1. AGENCY USE ONLY (Leave Blank)	2. REPORT DATE October 1993	3. REPORT TYPE AND DATES COVERED Final	

4. TITLE AND SUBTITLE
Finite-Difference Time-Domain Integration of Ultrafast Dynamics in Optical Resonators

5. FUNDING NUMBERS

6. AUTHORS
Scott Alan Basinger

AFRL-SR-BL-TR-98-

0003

7. PERFORMING ORGANIZATION NAME(S) AND ADDRESS(ES)
University of Illinois at Urbana-Champaign

9. SPONSORING/MONITORING AGENCY NAME(S) AND ADDRESS(ES)
AFOSR/NI
110 Duncan Avenue, Room B-115
Bolling Air Force Base, DC 20332-8080

10. SPONSORING/MONITORING AGENCY REPORT NUMBER

11. SUPPLEMENTARY NOTES

12a. DISTRIBUTION AVAILABILITY STATEMENT
Approved for Public Release

12b. DISTRIBUTION CODE

13. ABSTRACT *(Maximum 200 words)*
See attached.

19980115 184

DTIC QUALITY INSPECTED 2

14. SUBJECT TERMS

15. NUMBER OF PAGES

16. PRICE CODE

17. SECURITY CLASSIFICATION OF REPORT Unclassified	18. SECURITY CLASSIFICATION OF THIS PAGE Unclassified	19. SECURITY CLASSIFICATION OF ABSTRACT Unclassified	20. LIMITATION OF ABSTRACT UL

UNIVERSITY OF ILLINOIS AT URBANA-CHAMPAIGN

THE GRADUATE COLLEGE

OCTOBER 1993

WE HEREBY RECOMMEND THAT THE THESIS BY

SCOTT ALAN BASINGER

ENTITLED FINITE-DIFFERENCE TIME-DOMAIN INTEGRATION OF

ULTRAFAST DYNAMICS IN OPTICAL RESONATORS

BE ACCEPTED IN PARTIAL FULFILLMENT OF THE REQUIREMENTS FOR

THE DEGREE OF MASTER OF SCIENCE

Eavil Pradey
Director of Thesis Research

N. Narayana Rao
Head of Department

Committee on Final Examination†

_____
Chairperson

_____

_____

_____

_____

† Required for doctor's degree but not for master's.

O-517

ACKNOWLEDGEMENTS

TABLE OF CONTENTS

LIST OF FIGURES

CHAPTER 1

INTRODUCTION

1.1 Goals

This thesis discusses optical pulse discrimination in nonlinear resonators. The goal is to design a system which interacts strongly with an optical pulse of a specific temporal shape but rejects all others.

The resonator is a Fabry-Perot cavity that has a nonlinear absorbing material in the center. When an optical field of the resonant frequency is incident upon the cavity, the field intensity increases inside the cavity. As this happens, the refractive index of the nonlinear material is modified by the intensity of the field. This causes the cavity to shift off resonance, since the change in index changes the relative wavelength of the optical field inside the cavity. This, in turn, causes the intensity in the middle section to decrease, since the frequency of the field is no longer matched to the resonance frequency of the cavity. However, if the incident field's frequency is dynamically changed to track the shifting resonance of the cavity, the intensity of the interior field can be built up higher than is possible with just monochromatic light.

By looking at the total absorption in the cavity, it will be possible to determine whether or not a pulse of the correct temporal shape has passed through the system.

1

The absorption is strongly dependent on the shape of the incoming pulse, since only a pulse that tracks the nonlinear change in index will build up to a high enough intensity to be measured.

The incident light in this system is in the form of a three-dimensional pulse, consisting of two spatial dimensions and time (see Fig. 1.1). The temporal and spatial patterns of the pulse can be controlled to a high degree of accuracy using volume holography. The number of degrees of freedom in such a pulse is equal to the products of the space bandwidth product (SBP) and the time bandwidth product (TBP). The SBP is the quotient of the total area of the pulse and the smallest recognizable feature, or the spatial resolution. A pulse with an area of 1 cm^2 and of wavelength 1 μm may have an SBP of at most (1 cm)^2 / (1 μm)^2 = 10^8. The TBP is the length of the pulse in time divided by the smallest recognizable feature in time. If we have a 100-ps pulse with 100-fs temporal resolution, as might be generated by a pulsed Ti-sapphire laser, the TBP is 100 ps / 100 fs = 1000. The number of degrees of freedom in this pulse, then, is 10^{11}. A linear absorber integrates the incident intensity over time and effectively ignores the temporal characteristics of the pulse. The number of degrees of freedom that can be recorded with a linear absorber is only the SBP. But if we can design a nonlinear absorber that is highly sensitive to the temporal pattern of the pulse, we can extract both the spatial and temporal information from the pulse, increasing the number of degrees of freedom by the TBP. This means that we could increase the spatial resolution of the recorded pulse by at most the square root of the TBP.

A pulse sensitive system would be useful for high-speed optical communications. For example, a nonlinear filter could detect and direct packets of information and send them to the correct location at ultra-fast speeds. An array of filters could be used in an optical computer to process in parallel the temporal shape of the incident field.

2
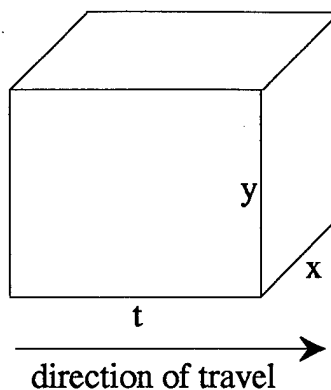
Figure 1.1. Incident pulse.

Another application of this technology is called a "magic bullet." On a quantum dynamic level, molecules behave like nonlinear resonators. An electromagnetic field incident upon a molecule transfers energy to it and can cause it to resonate. But just like the nonlinear Fabry-Perot cavity, this changes the resonant frequency of the molecule, limiting the amount of energy that can be transferred to it with a monochromatic field. However, a pulse of energy could be designed to have a specific quantum mechanical effect on a specific molecule. It is possible to model these quantum mechanical systems as a series of nonlinear Fabry-Perot cavities and, hence, study the molecular interactions with pulse-shaped fields.

The idea of a nonlinear Fabry-Perot cavity is not a new one. They have been studied extensively in the area of optical bistability. In optical bistability, the resonance of a cavity is switched between two stable states by an optical field, mimicking an electronic transistorized switch. However, this has met with limited success.

1.2   Methods of Analysis

Various numerical techniques are utilized in this thesis to determine the optimal cavity design and pulse shape. Among these are steady-state analysis and, most importantly, finite-difference time-domain (FD-TD) integration techniques. Conven-

3

tional steady-state analytic techniques, which are normally performed in the frequency domain, will be used to determine the initial geometry of the cavity and to obtain an intuitive feel for the problem. However, frequency domain analysis fails to describe the complexity of the ultra-fast nonlinear effects involved with pulsed optical fields. In addition, spectral analysis fails to detect the dynamic resonance shifts caused by the optical driving field, because cross-spectral effects are not included. To understand these ultra-fast effects, the evolution of the system must be determined numerically in the time domain.

Much work has been done with FD-TD techniques by A. Taflove et al. [1], [2], [3] in the areas of electromagnetic scattering, radar cross section, and soliton propagation in optical fibers. This work has been expanded to include resonators and dispersion in metals. In addition, the pulses we are working with are much shorter (on the order of 100 fs), and the response times are much quicker (10-100 fs) than have previously been studied with FD-TD techniques.

1.3   Introduction to Nonlinear Optics

1.3.1   The nonlinear refractive index

This section includes some preliminary notes on nonlinear optics that are necessary for the understanding of the rest of the thesis. Nonlinear optics describes the interaction of intense light with matter [4]. If strong enough, electromagnetic radiation can change the optical properties of the material it is incident upon. The polarization $\tilde{P}(t)$ of an optical system is the dipole moment per unit volume. In a nonlinear medium, $\tilde{P}(t)$ is dependent on the optical field strength $\tilde{E}(t)$ in the following way:

$$\tilde{P}(t) = \chi^{(1)}\tilde{E}(t) + \chi^{(2)}\tilde{E}^2(t) + \chi^{(3)}\tilde{E}^3(t) + \dots \tag{1.1}$$

4

where $\chi^{(1)}$ is the linear susceptibility, and $\chi^{(2)}$ and $\chi^{(3)}$ are the second- and third-order nonlinear susceptibilities, respectively. As can be seen, the polarization depends on multiple powers of the field strength, hence the term "nonlinear optics." The values of $\chi^{(2)}$ and $\chi^{(3)}$ are usually very small, and unless the field is extremely intense, the higher-order terms of the field will have no effect on the polarization. In addition, only non-centro-symmetric materials have a nonzero $\chi^{(2)}$. We focus on amorphous media in this thesis, and will therefore assume $\chi^{(2)}$ to be zero.

The constitutive equation relating the electric flux density $\tilde{D}$ to the electric field intensity $\tilde{E}$ is

$$\tilde{D} = \epsilon \tilde{E}, \tag{1.2}$$

which can also be written as

$$\tilde{D} = \tilde{E} + 4\pi \tilde{P}. \tag{1.3}$$

In addition, $\tilde{P}$ can be separated into its linear and nonlinear parts, P_L and P_{NL}.

Since $\tilde{P}$ is frequency dependent, we must examine how it reacts to a field composed of multiple frequencies. Conventionally, a field consisting of three frequencies is investigated in considering third-order nonlinearities:

$$\tilde{E}(t) = E_1 e^{-i\omega_1 t} + E_2 e^{-i\omega_2 t} + E_3 e^{-i\omega_3 t} + \text{c.c.} \tag{1.4}$$

Plugging this into the nonlinear polarization equation,

$$\tilde{P}^{(3)}(t) = \chi^{(3)} \tilde{E}(t)^3, \tag{1.5}$$

gives 44 different frequency components. By equating these with the right-hand side of

$$\tilde{P}^{(3)}(t) = \sum_n P(\omega_n) e^{-i\omega_n t}, \tag{1.6}$$

we obtain a simplistic dispersion relationship for the nonlinear polarization. For a field with only one frequency, this relation is

$$P_{NL}(\omega) = 3\chi^{(3)}(\omega)|E(\omega)|^2 E(\omega). \tag{1.7}$$

5

Substituting Eq. (1.7) into Eq. (1.3) gives

$$\tilde{D} = (1 + 4\pi\chi^{(1)} + 12\pi\chi^{(3)}|E(\omega)|^2)E(\omega). \tag{1.8}$$

Comparing this with Eq. (1.2), we see that

$$\epsilon = 1 + 4\pi\chi^{(1)} + 12\pi\chi^{(3)}|E(\omega)|^2. \tag{1.9}$$

Since the index of refraction is defined as the square root of the permittivity, and the linear part is defined as $n_0 = (1 + 4\pi\chi^{(1)})^{1/2}$, we have

$$n = (n_0^2 + 12\pi\chi^{(3)}|E(\omega)|^2)^{1/2}, \tag{1.10}$$

which can be approximated by

$$n = n_0 + \frac{6\pi\chi^{(3)}|E(\omega)|^2}{n_0}. \tag{1.11}$$

By letting $\bar{n}_2 = 3\pi\chi^{(3)}/n_0$, we obtain the final relationship between the refractive index and the field strength:

$$n = n_0 + 2\bar{n}_2|E(\omega)|^2. \tag{1.12}$$

The previous rationale works well for the steady-state analysis of monochromatic fields. However, the assumption of only three frequencies made in Eq. (1.4) is not sufficient to describe an ultra-short pulse, since it contains a continuum of many frequencies. In addition, frequency domain analysis cannot handle the complicated cross-spectral effects due to dispersion. For these reasons, it is necessary to perform the calculations in the time domain.

Time-domain analysis of nonlinearities in optical materials and cavities is the focus of this thesis. Equation (1.1) is insufficient to describe the complicated nonlinear polarization that we wish to look at. Instead, the dispersion relation is represented as a convolution in the time domain, as suggested by Goorjian and Taflove [2]:

$$
\begin{aligned}
\tilde{P}(t) &= \int_{-\infty}^{\infty} \chi^{(1)}(t - t')\tilde{E}(t')dt' \\
&+ \int_{-\infty}^{\infty}\int_{-\infty}^{\infty}\int_{-\infty}^{\infty} \chi^{(3)}(t - t_1, t - t_2, t - t_3)\tilde{E}(t_1)\tilde{E}(t_2)\tilde{E}(t_3)dt_1 dt_2 dt_3.
\end{aligned}
\tag{1.13}
$$

Once we have the structure of the polarization, it is necessary to pick a specific dispersion model. This is explored in more detail in Section 3.3.

1.3.2 Material considerations

As we have seen, $\chi^{(3)}$ is a frequency-dependent parameter. Therefore, a resonance frequency exists where it reaches a maximum. In addition, the nonlinear response of a material is not instantaneous, but rather it is time dependent. The response time is inversely proportional to the strength of the nonlinear interaction. Therefore, the response time for a resonant interaction is generally relatively slow.

We are interested in very fast interactions, so that dynamic changes smaller than the length of the incoming pulse can be tracked. Polydiacetylenes are a class of organic polymer that have a large, nonresonant third-order nonlinearity and are, therefore, ideally suited to nonlinear applications requiring fast response times. The off-resonant response time for a typical polydiacetylene has been estimated to be less than 100 fs [5], [6].

In addition, thin layered films can be made with relative ease out of certain types of polydiacetylene. For example, poly-4-BCMU is a particular form of polydiacetylene that is readily soluble in a solvent such as chloroform. It can thus be dip-coated onto slides, making it easy to make thin films. After it is dip-coated, it is irradiated by ultraviolet light in order to polymerize the monomers left on the slide.

A typical value for the third-order nonlinear susceptibility of polydiacetylene is $\chi^{(3)} = 2.5 \times 10^{-10}$. By focusing the output of a Ti-sapphire laser, it should be possible to generate a pulse with a field intensity of $E = 2500$ statvolt/cm, which corresponds to an intensity of about 3 GW/cm^2. With a linear refractive index of $n_0 = 1.45$, Eq. (1.12) shows the index change caused by the field to be 0.02.

1.4 Thesis Overview

As has been shown, frequency-domain techniques are insufficient to completely analyze the ultra-fast optical effects that we wish to observe. Instead, we must use numerical time-domain analysis. However, steady-state frequency-domain techniques are still employed in Chapter 2 to determine the geometry and preliminary design of the nonlinear cavity. Chapter 3 outlines the details of the finite-difference time-domain techniques developed and used for the necessary dynamic numerical analysis. Chapter 4 brings it all together by first discussing the final design of the cavity using all of the techniques mentioned, then the calculation of the pulse shape, and finally the results of the numerical analysis.

CHAPTER 2

THIN FILM RESONATOR DESIGN

2.1 Introduction

An example of a thin-film optical resonator is shown in Fig. 2.1. It consists of a layer of a dielectric medium an odd number of half-wavelengths thick, surrounded on both sides by reflecting surfaces. These "reflecting surfaces" can either be composed of layers of quarter-wavelength dielectric stacks or of thin metal films. This particular structure is referred to as a Fabry-Perot cavity, and acts as a band-pass filter for the frequency of electromagnetic radiation that it is designed for. In the analysis that follows, we assume that the light source is normal to the face of the cavity, and is incident from the left side.

When light of the proper frequency is incident on the cavity, the intensity of the field builds up in the middle dielectric. In certain cases, the intensity of the field inside the cavity can become larger than that of the incident field. We are interested in high intensities in order for nonlinear effects to take place. Various methods of achieving this goal will be explored in this chapter.

9
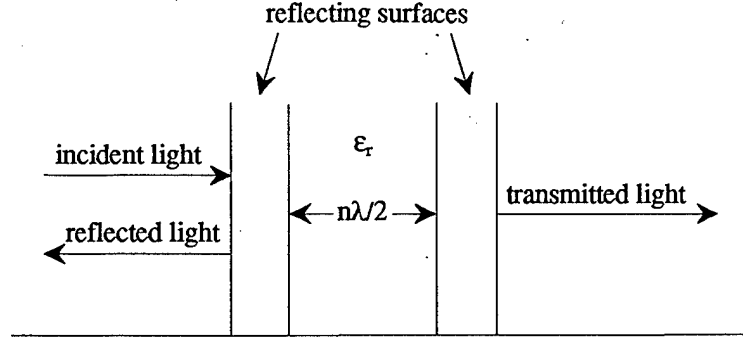
Figure 2.1. Fabry-Perot cavity.

2.2 Steady-State Analysis

To examine the optical field intensities inside a thin-film resonator, Maxwell's equations may be solved using steady-state techniques. Since we are assuming that the radiation is normal to the cavity, we only have to be concerned with a one-dimensional analysis. In this case, the electric field vector may be represented by a series of 2 × 2 propagation matrices, as in [7]. The field can be broken down into a right-traveling and a left-traveling wave:

$$E(z) = Re^{-ik_z z} + Le^{ik_z z} \equiv A(z) + B(z), \tag{2.1}$$

where R and L are constants, and $A(z)$ and $B(z)$ are the amplitudes of the left and right traveling waves, respectively. In vector form, the field is represented by

$$E(z) = \begin{pmatrix} A(z) \\ B(z) \end{pmatrix}. \tag{2.2}$$

To solve for the optical fields everywhere in a system such as that in Fig. 2.2, two additional matrices must be defined: a propagation matrix and an interface matrix. The former is used to propagate the field from $z = d$ to $z = 0$ and is represented as

$$P_\alpha = \begin{pmatrix} e^{ik_{\alpha z} d} & 0 \\ 0 & e^{-ik_{\alpha z} d} \end{pmatrix}, \tag{2.3}$$

10
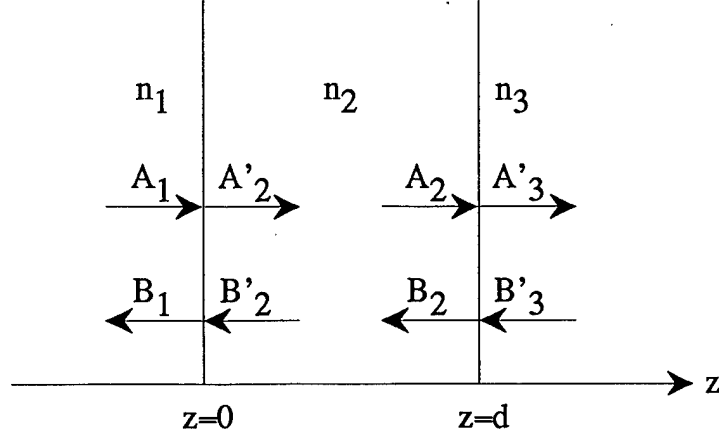
Figure 2.2. A thin dielectric.

where $k_{\alpha z}$ is the wave-number $2\pi n_\alpha / \lambda$. The latter is used to transform the field across an interface where the index of refraction changes and has the following form:

$$D_\alpha = \begin{pmatrix} 1 & 1 \\ n_\alpha & -n_\alpha \end{pmatrix}. \tag{2.4}$$

Two interface matrices are needed for this operation, D and D^{-1}, for each side of the barrier.

Assuming a structure like that in Fig. 2.2, the matrix method for solving for the amplitudes of the waves is as follows:

$$\begin{pmatrix} A_1 \\ B_1 \end{pmatrix} = D_1^{-1} D_2 \begin{pmatrix} A_2' \\ B_2' \end{pmatrix} \tag{2.5}$$

$$\begin{pmatrix} A_2' \\ B_2' \end{pmatrix} = P_2 \begin{pmatrix} A_2 \\ B_2 \end{pmatrix}$$

$$\begin{pmatrix} A_2 \\ B_2 \end{pmatrix} = D_2^{-1} D_3 \begin{pmatrix} A_3' \\ B_3' \end{pmatrix}.$$

Combining these equations gives

$$\begin{pmatrix} A_1 \\ B_1 \end{pmatrix} = D_1^{-1} D_2 P_2 D_2^{-1} D_3 \begin{pmatrix} A_3' \\ B_3' \end{pmatrix} \tag{2.6}$$

11

This method can be repeated for multiple layers as is necessary. For metals, the only difference is that the index of refraction is a complex number.

To find the reflection and transmission coefficients of a particular structure, the field at the output is set to $A'_n = 1$ and $B'_n = 0$; B'_n is set to zero because there is no wave traveling to the left at the output of the system. The reflection and transmission coefficients are then determined by

$$R = \frac{|B_1|^2}{|A_1|^2},$$
$$T = \frac{|n_n| \cdot |A_n|^2}{|n_1| \cdot |A_1|^2},$$

(2.7)

where the subscript n denotes the number of the last layer. To solve for the field *inside* a structure, the following formula can be used:

$$E = \frac{|n_m| \cdot |A_m + B_m|^2}{|n_1| \cdot |A_1|^2},$$

(2.8)

where the subscript m denotes the number of the matrix where the field is to be measured.

2.3 Examples

2.3.1 Pure dielectric stacks

As mentioned previously (Sec. 2.1), one method of creating a resonator is to have quarter-wave stacks of alternating dielectric constants placed on either side of the center half-wavelength dielectric (see Fig. 2.3). The quarter-wave stacks act as reflectors for a specific wavelength, so it is constructive to look at the reflective properties of these quarter-wave stacks. The first characteristic to consider is the reflectivity versus the number of layers. Typical values for the indices might be $n_1 = 1.33$ and $n_2 = 1.60$, and the results are plotted in Fig. 2.4. As can be seen, the reflection coefficient does not benefit from having more than 16 or so layers.
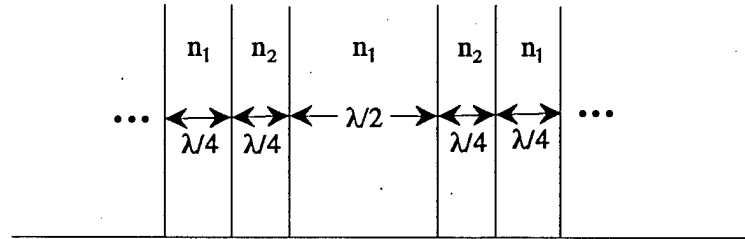
Figure 2.3. All-dielectric Fabry-Perot cavity.
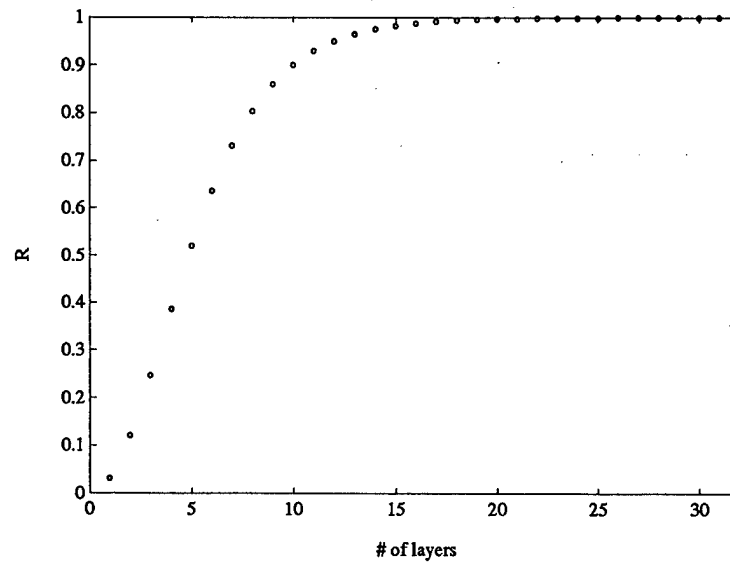
Figure 2.4. Reflectance vs. number of layers for $n_1 = 1.33$ and $n_2 = 1.60$.

13

For pulse discrimination, an ideal filter would be reflective under certain field situations, but would become transmissive under others. This is theoretically obtainable if alternating layers of the dielectric stack are composed of a highly nonlinear material. Then if the light passing through the stack is weak, the filter will act as a reflector. However, if the light is strong enough to shift the index of refraction of the nonlinear material by a suitable amount, the film will become transparent. Consider the case in which n_1 is a linear material and n_2 is a nonlinear material. Since typical index changes are generally quite small, consider the maximum index change of n_2 that could be obtained to be 0.02 (see Section 1.3.2). One method of making the filter transparent would be to set the linear index of n_2 at 0.02 below that of n_1. When strong light is passed through the filter, the indices of the two materials would become equal and the light would pass through. However, the closer the indices of refraction are to each other, the more layers that are necessary to have high reflection under weak conditions. Figure 2.5 shows that the number of layers needed to approach a reflectance of 1 is over 200. We would like thinner structures, however, so that the effects are more spatially localized. This will help to reduce the amount of diffraction.
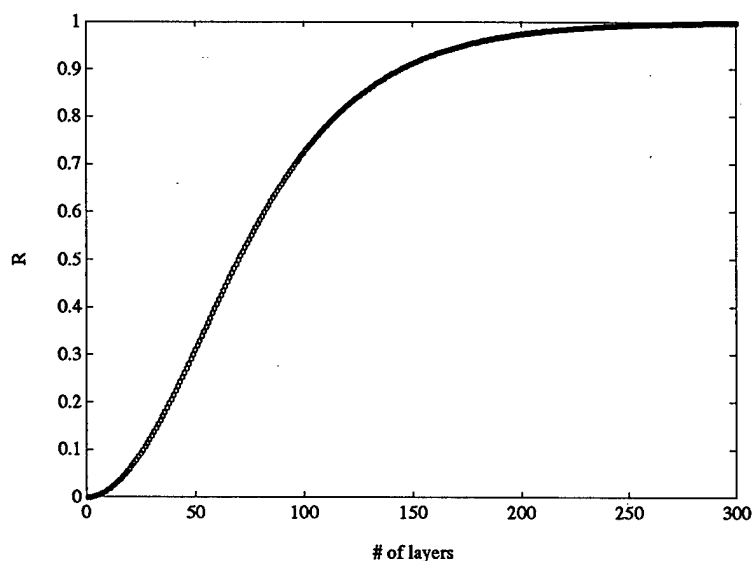
Figure 2.5. Reflectance vs. number of layers for $n_1 = 1.58$ and $n_2 = 1.60$.

A plot of reflection vs. n_2 for a filter designed for $n_1 = 1.33$ and $n_2 = 1.60$ and containing 16 layers is shown in Fig. 2.6. There is a sharp drop-off in reflection at $n_2 = 2.08$. This drop-off can be utilized to synthesize the desired filter. The normal index of the nonlinear material, n_2, is made to be 2.05, which gives a total reflectivity of the filter of 0.7908. Under strong field conditions, the index of n_2 changes to 2.07, which changes the reflectivity of the filter to 0.2190. Filters with even more dramatic changes in reflectivity can be designed by using more layers of the dielectric.
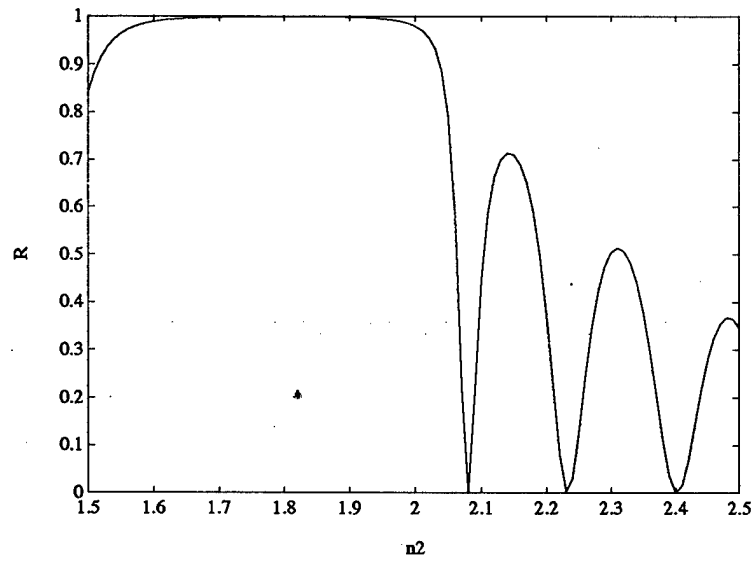
Figure 2.6. Reflectance vs. n_2 for 16 layers.

This method looks good in the steady state, but as will be seen later, when actually simulated using the FD-TD algorithm, problems were discovered. For instance, the intensity of the field inside the nonlinear material is not uniform throughout each layer, but has a standing-wave pattern, whice causes the index change in the nonlinear material to be less than expected. Also, the intensity of the light decreases as it travels through the filter. Therefore, the index change also decreases over the length of the filter. For these reasons, it was decided to use metals for reflecting surfaces, rather than dielectric stacks. In addition, the metal layers can be made much thinner, which keeps the electromagnetic fields more spatially localized.

2.3.2 Design and steady-state analysis with metal reflectors

In a pulse discriminating filter, the dielectric in the center of the Fabry-Perot cavity is a highly nonlinear material, such as polydiacetylene. As the field builds up inside the cavity, the resulting nonlinear index change causes the cavity to go off resonance. However, if the frequency of the field dynamically tracks the index change, it may be possible to build up the intensity of the field higher inside the cavity than would be possible with monochromatic light. This section explores the feasibility of designing a cavity to perform such a task.

The qualities that can be explored in the steady state are limited, but nonetheless useful. A cavity must be designed that will maximize the intensity of the field in the center of the cavity to produce a maximal index change in the nonlinear material. As the field builds up, the index change should be significant enough to change the resonant frequency of the cavity. To accomplish both of these goals, the cavity must have a high Q-factor. The "Q-factor," or "quality factor," is the quotient of the gain and the line width. In addition, to reduce reflections seen by the incoming field, a dielectric is placed on the exterior surfaces of the the metals. For simplicity of design, these antireflection dielectrics will be assumed to be made of the same nonlinear material as that inside the cavity. The setup can be seen in Fig. 2.7. The optimal length of the nonlinear dielectrics may be only approximate multiples of the wavelength, since the metal surfaces induce a phase shift in the field. Optimal values are determined from numerical analysis.

To optimize the cavity, a numerical algorithm was written to examine the field intensity inside the cavity vs. various layer thicknesses, indices of refraction, and wavelengths of the incoming field. For the calculations, the linear index of the dielectrics is assumed to be $n_d = 0.45$. The metal is silver, which has a complex index of refraction of $n_m = 0.2378 + i6.78702$. Determining the thicknesses of the nonlinear dielectrics is automatic, since we want the field intensity to always be maximized in

metal surfaces

air   air

~λ/4   ~$n\lambda$/2   ~λ/4

nonlinear dielectrics
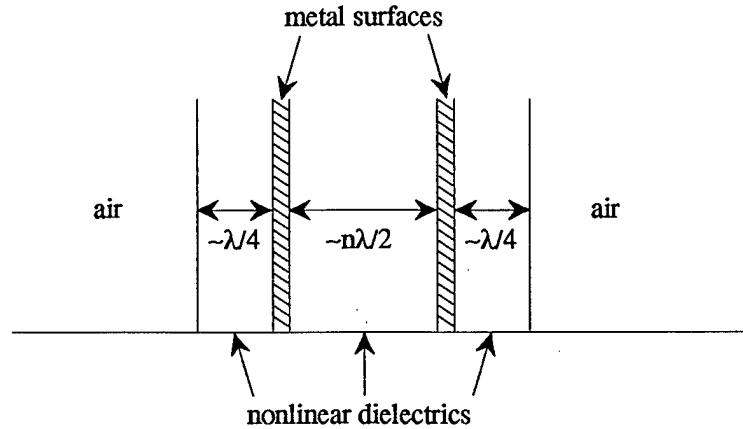
Figure 2.7. Final design for Fabry-Perot cavity.

accordance with the layer thicknesses. An example of the field intensity vs. dielectric thickness for $l_m = .05$, where l_m is the thickness of the metal layers in units of wavelength, can be seen in Fig. 2.8. The maximum intensity occurs when the center dielectric thickness is 0.297 wavelength and the outer dielectric thickness is 0.160 wavelength.
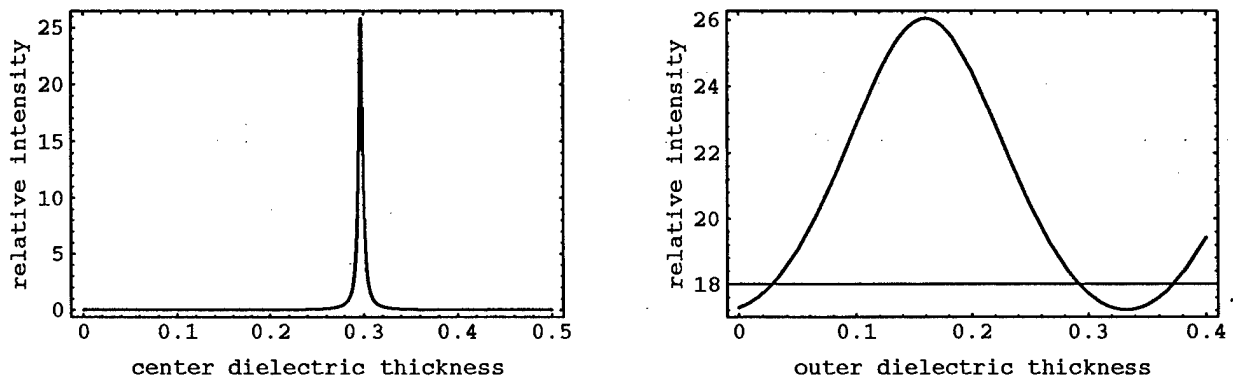
Figure 2.8. Relative field intensity inside cavity vs. dielectric thickness.

Next the effect of different metal layer thicknesses is explored. Figure 2.9 is a plot of the relative field intensity in the center of the cavity vs. the thickness of the metal reflectors, with the dielectric layers already optimized. The field intensity peaks at 28.7 with a metal thickness of 0.042. Figure 2.10 shows several different plots of the intensity of the field in the middle of the cavity vs. the index of refraction used

17
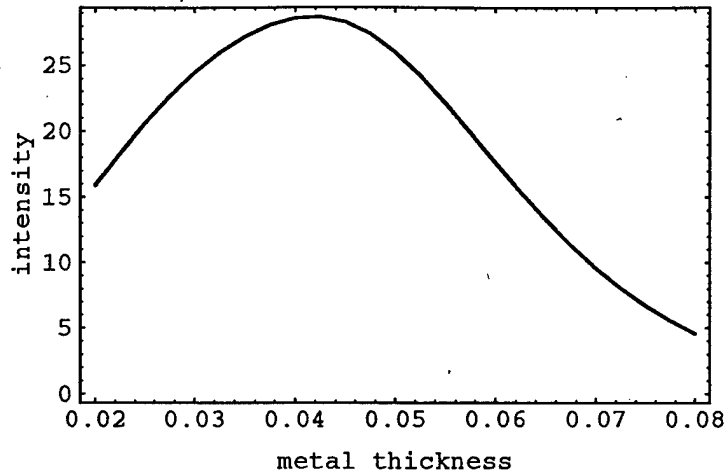
Figure 2.9. Relative field intensity inside cavity vs. metal thickness.

for the dielectrics. These plots are useful to see how the cavity will react when the intensity of the light shifts the index of the nonlinear material. As the metal layers get thicker, the linewidth decreases. However, the maximum intensity also decreases after $l_m = 0.042$. A compromise must be found between these two trade-offs.

We use the steady-state analysis to characterize the wavelength sensitivity of the cavity as the nonlinear index of the dielectric is changed by high intensity light. This will determine the metal thickness. Figure 2.11 shows four different plots of the intensity inside the cavity vs. the inverse wavelength of incident light. Each plot contains two curves, the first of which is centered around the middle and represents the linear response of the cavity. The other curve shows the frequency response for the cavity when a high intensity incident field is present inside the cavity and the index of the dielectric has changed by +0.02.

Assuming an incident field of relative wavelength $\lambda = 1$, the linear plot shows the maximum intensity that can build up inside the cavity. However, as the high intensity changes the index of refraction, the cavity shifts off resonance and the intensity inside drops. Assuming the index changes by 0.02, the intensity will drop to the value at which the second plot crosses the x-axis. Since we are looking for a high sensitivity to the wavelength, we want this value to be as low as possible. A relative comparison

18
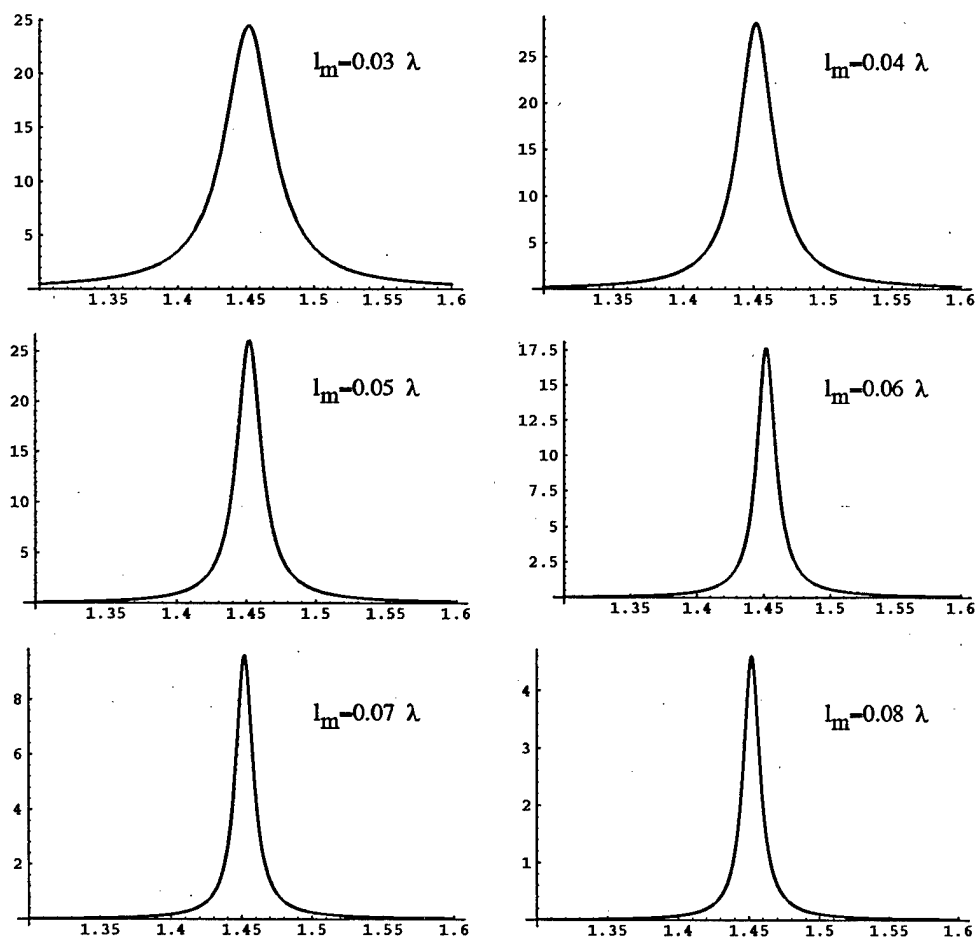
Figure 2.10. Intensity inside cavity vs. index of refraction of dielectric for several different metal thicknesses, l_m.
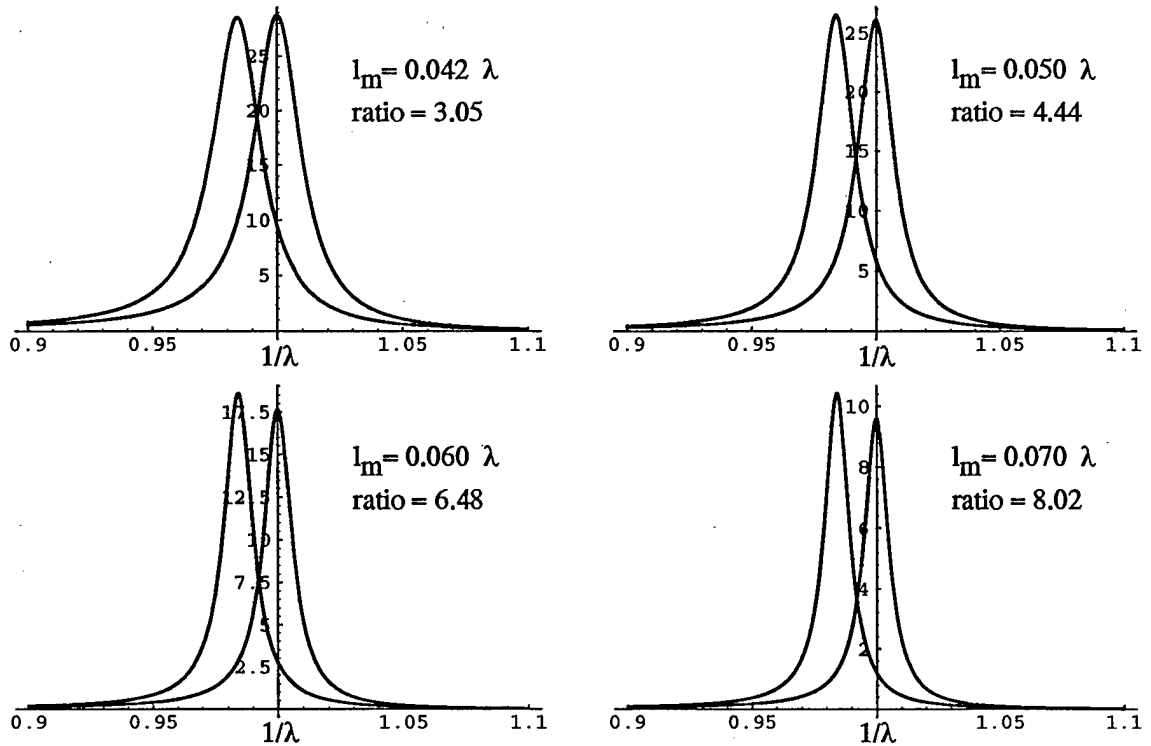
Figure 2.11. Intensity inside cavity vs. $1/\lambda$ for several different metal thicknesses, l_m. The center layer is $\lambda/2$ thick.

can be made between the four graphs by dividing the linear maximum intensity by the nonlinear x-axis crossing. This quotient is denoted as "ratio" on each of the graphs.

At this point we perform the entire analysis over again, but this time the center layer thickness is changed from $\lambda/2$ to $3\lambda/2$. The resonance of the cavity remains the same, but the amount of nonlinear material that the field is exposed to is effectively tripled. Because of this, the effective wavelength changes more than it does in the previous case, which causes the plots of the intensity vs. wavelength to be narrower, thus dramatically increasing the "ratio" of the cavity. Figure 2.12 shows two different plots of this situation.

Figures 2.11 and 2.12 also supply information about the steady-state stability of the cavity. The right-hand plot shows the resonance frequency of the cavity when there is no light present. If light of any intensity is incident upon the cavity, the
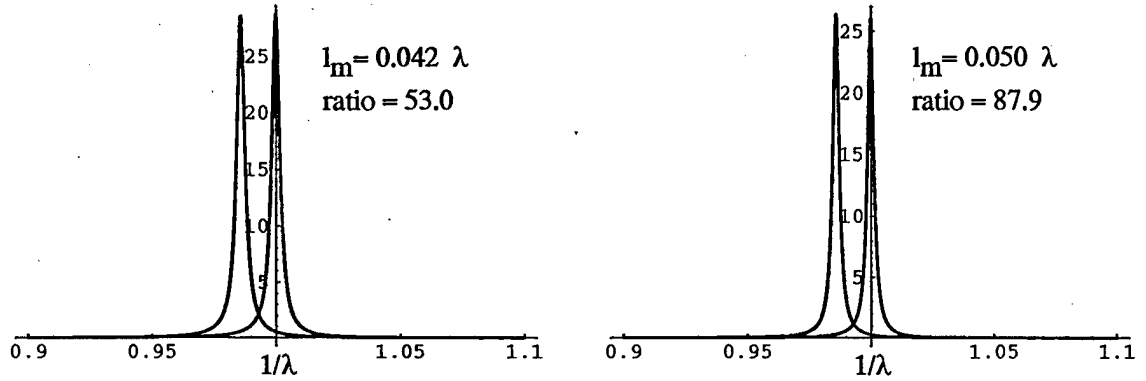
Figure 2.12. Intensity inside cavity vs. $1/\lambda$ for two different metal thicknesses. The center layer is $3\lambda/2$ thick.

resonance will shift to the left. If light of a frequency slightly higher than "1" is incident upon the cavity, the intensity will not build up very high, since it is off-resonance. However, what intensity *is* there will force the resonance to shift slightly to the left, causing the intensity to drop even further, which will pull the resonance back to the right. Because the behavior is resistant to change for this case, we say that the system is stable.

If light of a frequency slightly lower than "1" is incident upon the cavity, the intensity will not build up very high at first. However, what intensity *is* present will cause the resonance to shift slightly to the left, causing the intensity to increase and the resonance to shift even more to the left. This will continue until the peak intensity is reached and we have the previously mentioned situation.

See Appendix A for code for numerical simulations.

Although the steady-state analysis is helpful in the initial design of the cavity, it is insufficient to describe the interactions that occur in the actual system. This is due to the complex dispersion models used and the numerous frequency components contained in the ultra-fast optical pulses being used. For further analysis, it will now be necessary to introduce finite-difference time-domain techniques.

21

CHAPTER 3

THE FD-TD ALGORITHM IN DISPERSIVE AND NONLINEAR MEDIA

3.1 Introduction to the Finite-Difference Time-Domain Algorithm

In the past, numerical modeling of Maxwell's equations has been performed using frequency-domain techniques, because time-domain techniques generally have very large memory requirements, and also require significant computational power. However, the finite-difference time-domain techniques discussed here [1] lower the memory requirements by making it necessary to store only two or three previous time steps in memory. Faster RISC workstations make it possible to perform the calculations in real time. However, all of the calculations performed in this thesis are in one dimension. Two- and three-dimensional calculations would require additional memory to store all the spatial requirements.

We use finite-difference time-domain analysis to solve Maxwell's equations directly in the time domain. This is absolutely necessary for nonlinear analysis, since the frequency components are coupled and cannot be solved by Fourier decomposition. Ultra-fast pulses are also composed of multiple frequencies and are better suited to

time-domain analysis. In addition, time convolutions can be more sophisticated when performed in the time domain, which is necessary for certain dispersive models.

The FD-TD algorithm directly integrates Maxwell's curl equations. In one dimension, these are

$$\frac{\partial \mathcal{H}_y}{\partial t} = -c\frac{\partial \mathcal{E}_x}{\partial z} \tag{3.1}$$

$$\frac{\partial \mathcal{D}_x}{\partial t} = -c\frac{\partial \mathcal{H}_y}{\partial z} - 4\pi\sigma\mathcal{E}_x \tag{3.2}$$

$$\mathcal{D}_x = \epsilon_r\mathcal{E}_x + 4\pi\chi^{(3)}\mathcal{E}_x^3 \tag{3.3}$$

These equations are rewritten using the following approximations for the derivatives:

$$\frac{\partial F(z,t)}{\partial t} \simeq \frac{F(z,t) - F(z,t-1)}{\Delta t} \tag{3.4}$$

$$\frac{\partial F(z,t)}{\partial z} \simeq \frac{F(z,t) - F(z-1,t)}{\Delta z} \tag{3.5}$$

The problem is then broken up into two dimensions consisting of space and time as shown in Fig. 3.1. Two spatial arrays are defined to hold the values of the electric and the magnetic fields, respectively. In our analysis so far, each point in time depends only on the immediately preceding point in time, so only two time steps have to be retained in memory. However, in Section 3.3, it will be shown that three time steps are required. Therefore, the arrays for the electric and magnetic fields are two-dimensional, with one dimension representing space and the other representing time. The susceptibility and conductivity can be defined independently at each point in the spatial-dimension; hence, complex structures can be represented. Ignoring, for the moment, any nonlinearity, dispersion, absorption, and conductivity, the final difference equations for the numerical algorithm at each point in the arrays are as follows:

$$H_y(z,t) = H_y(z,t-1) + \frac{c\Delta t}{\Delta z}[E_x(z-1,t) - E_x(z,t)] \qquad (3.6)$$

$$E_x(z,t) = E_x(z,t-1) + \frac{1}{\epsilon_r(z)}\frac{c\Delta t}{\Delta z}[E_x(z-1,t) - E_x(z,t)] \qquad (3.7)$$

Numerical stability of these equations depends on the following criterion:

$$\frac{c\Delta t}{\Delta z} \leq 1. \qquad (3.8)$$
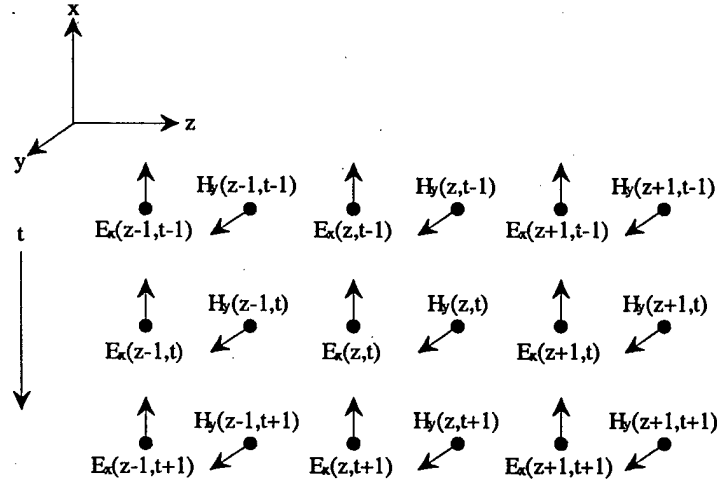
Figure 3.1. FD-TD lattice visualization.

Dispersion is included in the analysis as a linear convolution in the time domain. The time-domain convolution equation is Fourier transformed into the frequency domain where it becomes a multiplicative equation. A frequency-dependent model for the dispersive element is inserted into the equation, and the whole equation is inverse Fourier transformed back into the time domain with the use of the following identities:

$$j\omega \Leftrightarrow -\frac{\partial}{\partial t} \qquad (3.9)$$

$$(j\omega)^2 \Leftrightarrow +\frac{\partial^2}{\partial t^2}$$

$$(j\omega)^3 \Leftrightarrow -\frac{\partial^3}{\partial t^3}$$

$$\vdots$$

This method will be further illustrated in Sections 3.2 and 3.3.

3.2 Dispersion Model for Metals

Metals exhibit complex behaviors at optical frequencies. Both the dielectric constant ϵ and the conductivity σ are dependent on the frequency ω of the field. To incorporate this behavior into the analysis, a dispersive model must be used.

Since metals do not exhibit a high nonlinearity, the third-order susceptibility can be ignored. Remembering that ϵ and σ are frequency dependent, Equations (3.2) and (3.3) can be combined to give

$$-\frac{\partial \mathcal{H}_y(t)}{\partial z} = \frac{1}{c}(\epsilon_r(t) * \frac{\partial \mathcal{E}_x(t)}{\partial t}) + \frac{4\pi}{c}(\sigma(t) * \mathcal{E}_x(t)) \tag{3.10}$$

where * represents a linear convolution in time. Equation (3.10) can be Fourier transformed and simplified as follows:

$$
\begin{aligned}
-\frac{\partial \mathcal{H}_y(\omega)}{\partial z} &= \frac{\epsilon_r(\omega)}{c}(-j\omega)\mathcal{E}_x(\omega) + \frac{4\pi\sigma(\omega)}{c}\mathcal{E}_x(\omega) \\
-\frac{\partial \mathcal{H}_y(\omega)}{\partial z} &= \frac{-j\omega}{c}[\epsilon_r(\omega) - \frac{4\pi\sigma(\omega)}{j\omega}]\mathcal{E}_x(\omega) \\
\frac{\partial \mathcal{H}_y(\omega)}{\partial z} &= \frac{j\omega}{c}\hat{\epsilon}_r(\omega)\mathcal{E}_x(\omega)
\end{aligned}
\tag{3.11}
$$

where

$$\hat{\epsilon}_r(\omega) = \epsilon_r(\omega) + j\frac{4\pi\sigma(\omega)}{\omega}. \tag{3.12}$$

$\hat{\epsilon}_r(\omega)$ is then represented by a second-order model [8]:

$$\hat{\epsilon}_r(\omega) = \epsilon_\infty - \frac{\epsilon_s - \epsilon_\infty}{\omega(\omega - j\beta)}. \tag{3.13}$$

The parameters ϵ_∞, ϵ_s, and β were determined in Born & Wolf, p. 623 [8] from experimental data for silver to have the following values:

$$\epsilon_\infty = 6.60764, \quad \epsilon_s = 1.89235 \times 10^{32}, \quad \beta = -2.36136 \times 10^{14}.$$

This model provides a fairly accurate representation of dispersion in metals at plasma frequencies (see Fig. 3.2).
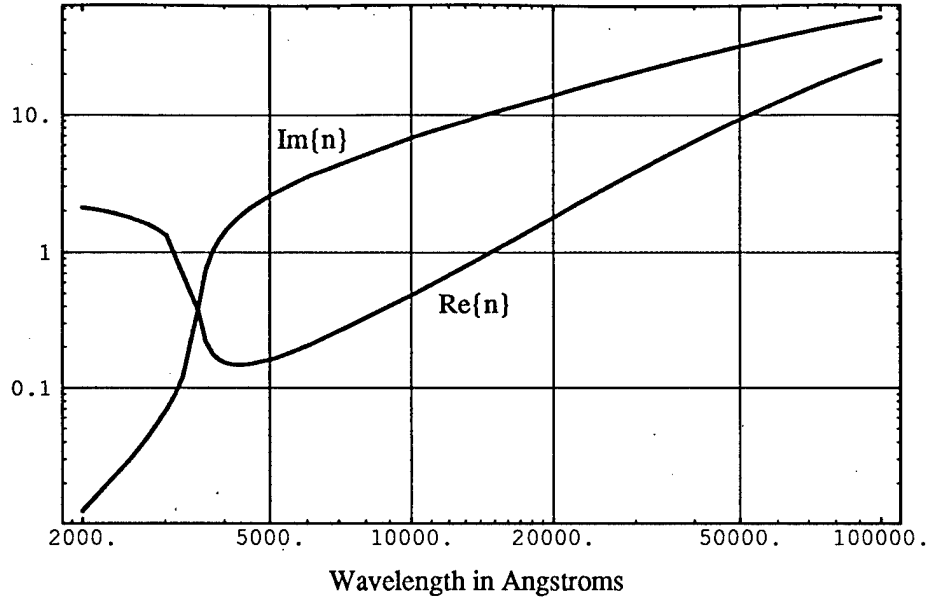
Figure 3.2. Index of refraction of silver ($\hat{\epsilon}_r = n^2$).

Inserting Eq. (3.13) into Eq. (3.11) and inverse Fourier transforming give the following differential equation:

$$\left(\frac{\partial}{\partial t} - \beta\right)\frac{\partial \mathcal{H}_y}{\partial z} = -\frac{\epsilon_\infty}{c}\left(\frac{\partial^2}{\partial t^2} - \beta\frac{\partial}{\partial t} + \frac{\epsilon_s + \epsilon_\infty}{\epsilon_\infty}\right)\mathcal{E}_x \qquad (3.14)$$

This equation is then converted into a difference equation. Because of the complexity of Eq. (3.14), care must be taken in how the approximations are made. $\frac{\partial \mathcal{H}_y(z,t)}{\partial z}$ is first approximated using Eq. (3.5). However, once $\frac{\partial \mathcal{H}_y(z,t)}{\partial z}$ has been calculated, $\frac{\partial \mathcal{H}_y(z,t)}{\partial t}$ and $\frac{\partial \mathcal{E}_x(z,t)}{\partial t}$ are then calculated by an alternate approximation:

$$\frac{\partial F(z,t)}{\partial t} \simeq \frac{F(z,t+1) - F(z,t)}{\Delta t} \qquad (3.15)$$

Finally, $\frac{\partial^2 \mathcal{E}_x(z,t)}{\partial t^2}$ is calculated by

$$\frac{\partial^2 F(z,t)}{\partial t^2} \simeq \frac{F(z,t+1) - 2F(z,t) + F(z,t-1)}{(\Delta t)^2} \qquad (3.16)$$

With these approximations, Eq. (3.14) becomes

26

$$\begin{aligned}
E_x(z, t+1) &= \left\{ \frac{c}{\epsilon_\infty \Delta z} [(1 + \Delta t \beta)(H_y(z,t) - H_y(z-1,t)) \right. \\
&\quad + H_y(z-1, t+1) - H_y(z, t+1)] \\
&\quad + (\frac{2}{\Delta t} - \beta + \Delta t \frac{\epsilon_\infty - \epsilon_s}{\epsilon_\infty}) E_x(z,t) - \frac{1}{\Delta t} E_x(z, t-1) \right\} / \\
&\quad \left(\frac{1}{\Delta t} - \beta \right).
\end{aligned} \tag{3.17}$$

This equation, along with Eq. (3.6) makes up the complete numerical algorithm for solving Maxwell's equations in a dispersive metal.

3.3 Nonlinear Dielectric Dispersion Model

This section relies heavily on two papers by Goorjian, Taflove, et al. [2], [3], which relate to soliton propagation in silicon fibers. Hence, the nonlinear dispersion models used also relate to soliton propagation. The interactions included in this analysis are Kerr and Raman scattering. There are, however, dispersion models that would be more ideally suited for our purposes here and they will be explored in the near future.

In nonlinear materials, ϵ_R and $\chi^{(3)}$ are frequency-dependent parameters. Therefore, Eqs. (3.2) and (3.3) must be solved very carefully.

Equation (3.3) can be written as

$$\mathcal{D}_x = \mathcal{E}_x + P_{x_L} + P_{x_{NL}}, \tag{3.18}$$

where P_{x_L} is the linear and $P_{x_{NL}}$ is the nonlinear polarization. The linear part can be written as a linear convolution in the time domain:

$$P_{x_L}(z, t) = \int_{-\infty}^{\infty} \chi^{(1)}(t - t') \mathcal{E}_x(z, t') \mathrm{d}t', \tag{3.19}$$

and the nonlinear part can be written as a nonlinear convolution in the time domain:

$$P_{x_{NL}}(z, t) = \int_{-\infty}^{\infty} \int_{-\infty}^{\infty} \int_{-\infty}^{\infty} \chi^{(3)}(t - t_1, t - t_2, t - t_3) \mathcal{E}_x(z, t_1) \mathcal{E}_x(z, t_2) \mathcal{E}_x(z, t_3) \mathrm{d}t_1 \mathrm{d}t_2 \mathrm{d}t_3, \tag{3.20}$$

where $\chi^{(1)}$ and $\chi^{(3)}$ are the first- and third-order susceptibilities, respectively.

The permittivity is represented by a Lorentzian model:

$$\epsilon(\omega) = \epsilon_\infty + \frac{\omega_0^2(\epsilon_s - \epsilon_\infty)}{\omega_0^2 - j\delta\omega - \omega^2}. \qquad (3.21)$$

Since $\epsilon(\omega) = \epsilon_\infty + \chi^{(1)}(\omega)$, $\chi^{(1)}(\omega)$ can be solved for and inverse Fourier transformed into

$$\chi^{(1)}(t) = \left(\frac{\omega_p^2}{\nu_0}\right) e^{-\delta t/2} \sin(\nu_0 t) \qquad (3.22)$$

where $\omega_p^2 = \omega_0^2(\epsilon_s - \epsilon_\infty)$ and $\nu_0^2 = \omega_0^2 - \delta^2/4$.

$P_{x_{NL}}(z,t)$ can be simplified into a single time convolution by assuming a Raman scattering model [9]:

$$P_{x_{NL}}(z,t) = \chi^{(3)} E_x(z,t) \int_{-\infty}^{\infty} g(t-t') E_x^2(z,t') \mathrm{d}t' \qquad (3.23)$$

where $\chi^{(3)}$ is the nonlinear coefficient and

$$
\begin{aligned}
g(t) &= \alpha\delta(t) + (1-\alpha)g_R(t) \qquad &(3.24)\\
g_R(t) &= \left(\frac{\tau_1^2 + \tau_2^2}{\tau_1\tau_2}\right) e^{-t/\tau_2} \sin(t/\tau_1).
\end{aligned}
$$

$\delta(t)$ is the instantaneous impulse response of the Kerr media, $g_R(t)$ models the Raman scattering, and α determines the relative strengths of the two processes.

Equations (3.19) to (3.24) can be solved by rewriting the convolution integrals (3.19) and (3.23) as a new set of coupled equations as follows [3]:

$$
\begin{aligned}
F(t) &= \int_0^t \chi^{(1)}(t-t') E_x(z,t') \mathrm{d}t' \qquad &(3.25)\\
G(t) &= \int_0^t g_R(t-t') E_x^2(z,t') \mathrm{d}t'.
\end{aligned}
$$

Differentiating these equations gives the following set of coupled differential equations:

$$\frac{1}{\omega_0^2}\frac{\mathrm{d}^2 F}{\mathrm{d}t^2} + \frac{\delta}{\omega_0^2}\frac{\mathrm{d}F}{\mathrm{d}t} + \left(1 + \frac{\epsilon_s - \epsilon_\infty}{\epsilon_\infty + \alpha\chi^{(3)}E_x^2}\right)F + \left(\frac{(\epsilon_s - \epsilon_\infty)(1-\alpha)\chi^{(3)}E_x}{\epsilon_\infty + \alpha\chi^{(3)}E_x^2}\right)G \quad (3.26)$$

$$= \left(\frac{\epsilon_s - \epsilon_\infty}{\epsilon_\infty + \alpha\chi^{(3)}E_x^2}\right)D_x,$$

$$\frac{1}{\bar\omega_0^2}\frac{\mathrm{d}^2 G}{\mathrm{d}t^2} + \frac{\bar\delta}{\bar\omega_0^2}\frac{\mathrm{d}G}{\mathrm{d}t} + \left(1 + \frac{(1-\alpha)\chi^{(3)}E_x^2}{\epsilon_\infty + \alpha\chi^{(3)}E_x^2}\right)G + \left(\frac{E_x}{\epsilon_\infty + \alpha\chi^{(3)}E_x^2}\right)F$$

$$= \left(\frac{E_x}{\epsilon_\infty + \alpha\chi^{(3)}E_x^2}\right)D_x$$

where $\bar\delta = 2/\tau_2$ and $\bar\omega_0^2 = (1/\tau_1)^2 + (1/\tau_2)^2$. When Equations (3.26) have been solved simultaneously, the solutions can be inserted into

$$E_x = \frac{D_x - F - (1-\alpha)\chi^{(3)}E_x G}{\epsilon_\infty + \alpha\chi^{(3)}E_x^2}, \qquad (3.27)$$

which replaces Eq. (3.3) in the numerical algorithm.

Converting Equations (3.26) into difference equations (as in Section 3.2) results in the following:

$$\frac{1}{\omega_0^2}\left(\frac{F(z,t+1) - 2F(z,t) + F(z,t-1)}{(\Delta t)^2}\right) + \frac{\delta}{\omega_0^2}\left(\frac{F(z,t+1) - F(z,t-1)}{2\Delta t}\right) \quad (3.28)$$

$$+ \left(1 + \frac{\epsilon_s - \epsilon_\infty}{\epsilon_\infty + \alpha\chi^{(3)}(E_x(z,t))^2}\right)\left(\frac{F(z,t+1) + F(z,t-1)}{2}\right)$$

$$+ \left(\frac{(\epsilon_s - \epsilon_\infty)(1-\alpha)(\chi^{(3)}E_x(z,t))}{\epsilon_\infty + \alpha\chi^{(3)}(E_x(z,t))^2}\right)\left(\frac{G(z,t+1) + G(z,t-1)}{2}\right)$$

$$= \left(\frac{\epsilon_s - \epsilon_\infty}{\epsilon_\infty + \alpha\chi^{(3)}(E_x(z,t))^2}\right)\left(\frac{D_x(z,t+1) + D_x(z,t-1)}{2}\right),$$

$$\frac{1}{\bar\omega_0^2}\left(\frac{G(z,t+1) - 2G(z,t) + G(z,t-1)}{(\Delta t)^2}\right) + \frac{\bar\delta}{\bar\omega_0^2}\left(\frac{G(z,t+1) - G(z,t-1)}{2\Delta t}\right)$$

$$+ \left(1 + \frac{(1-\alpha)\chi^{(3)}(E_x(z,t))^2}{\epsilon_\infty + \alpha\chi^{(3)}(E_x(z,t))^2}\right)\left(\frac{G(z,t+1) + G(z,t-1)}{2}\right)$$

$$+ \left(\frac{E_x(z,t)}{\epsilon_\infty + \alpha\chi^{(3)}(E_x(z,t))^2}\right)\left(\frac{F(z,t+1) + F(z,t-1)}{2}\right)$$

$$= \left(\frac{E_x(z,t)}{\epsilon_\infty + \alpha\chi^{(3)}(E_x(z,t))^2}\right)\left(\frac{D_x(z,t+1) + D_x(z,t-1)}{2}\right).$$

These equations can then be solved for $F(z,t+1)$ and $G(z,t+1)$, respectively.

In the overall numerical algorithm for solving Maxwell's equations in a nonlinear dispersive media, Eq. (3.1) remains unchanged, so Eq. (3.6) can be used for determining $H_y(z, t+1)$. Then $D_x(z, t+1)$ can be calculated by differencing Eq. (3.2) ($\sigma = 0$) to

$$D_x(z, t+1) = D_x(z, t) + \frac{1}{\epsilon_r(z)} \frac{c\Delta t}{\Delta z}[H_y(z-1, t+1) - H_y(z, t+1)]. \qquad (3.29)$$

$D_x(z, t+1)$ is then used in conjunction with Eqs. (3.28) to solve for $F(z, t+1)$ and $G(z, t+1)$. All of these are then inserted into Eq. (3.30), which was derived from Eq. (3.27), to finally solve for $E_x(t+1, z)$; the solution is complete.

$$E_x(z, t+1) = \frac{D_x(z, t+1) - F(z, t+1) - (1-\alpha)\chi^{(3)}E_x(z, t)G(z, t+1)}{\epsilon_\infty + \alpha\chi^{(3)}E_x^2(z, t)}. \qquad (3.30)$$

The values used for the constants, once again, generally correspond to soliton propagation in fiber (with minor adjustments), and are as follows [2]:

$$\epsilon_\infty = 2.25, \quad \epsilon_s = 5.25, \quad \omega_0 = 4.0 \times 10^{14} \text{ rad/s}, \quad \delta = 2.0 \times 10^9 \text{ s}^{-1},$$

$$\chi^{(3)} = 9.8 \times 10^{-10} \text{ esu}, \quad \alpha = 0.1, \quad \tau_1 = 12.2 \text{ fs}, \quad \tau_2 = 320 \text{ fs}.$$

3.4   The FD-TD Program

3.4.1   General programing techniques for FD-TD

The three different types of media discussed above (linear with no dispersion, metals, and nonlinear with dispersion) can be combined to simulate complicated structures. This is best accomplished by setting up separate arrays that correlate with the arrays for the electric and magnetic fields, and setting the values for susceptibility, nonlinearity, and conductivity at each point.

Care must be taken when programming the driving field and when programming the external boundaries of the problem. Since each point in the arrays is dependent on other points in the arrays, problems occur at the initial and final points. Solutions to

these problems are not well documented in FD-TD literature, so further elaboration is necessary.

In the numerical simulations performed, an incident field enters from the left (see Fig. 3.1 for orientation) and interacts with various surfaces. Some of the field exits to the right, or output, and some of the field reflects back to the left, or input.

The incident field is programmed by setting the first point in the electric field equal to the desired value, and changing it at each time step to match the temporal shape of the field. The numerical algorithm handles it from there. In this way, any arbitrary input field can be programmed, from a steady-state wave to a chirped pulse.

In order to solve the problem of reflections at the output, the array containing the electric field is defined to be one point larger than the simulation contains. Then, at the appropriate time, the value held in the next to last point is shifted to this extra point. This works as long as there are no sharp boundaries at the output.

Because reflections back to the input may cause problems, they must be eliminated. This is done by keeping track of the input field and subtracting off any deviations from the input at the first point in the array (where the input field is set).

3.4.2 Description of the program

See Appendix B for the program listing. The program for solving the numerical algorithms was written in C and can be ported to most computer systems. Since visualization is always a helpful tool, there is a graphical output to view the simulation on Silicon Graphics computers. The electric and magnetic fields can be viewed in real time as the calculations are made. Also, the input and output pulses are drawn on the screen. In addition, there is an FFT algorithm included which can show the Fourier transform of the signal anywhere in the simulation. This real-time graphical output has proven to be a useful tool when designing and optimizing nonlinear filters, and in visualizing optical fields in general.

In addition to determining the electric and magnetic fields, other calculations can be made with the program. The power density in a certain area is calculated by integrating the square of the electric field over the distance which is being measured. The absorption is measured by subtracting the Poynting vector, $\mathcal{E} \times \mathcal{H}$, at the output from the Poynting vector at the input.

CHAPTER 4

OVERALL NONLINEAR FILTER DESIGN

4.1 Design of the Cavity

In this chapter we combine the steady-state preliminary design with the finite-difference time-domain analysis to simulate and test an ultra-fast nonlinear optical resonator. We will show how the filter reacts more favorably towards a specific pulse shape than towards a monochromatic field or a poorly designed pulse shape.

The design is exactly like that shown in Fig. 2.7. The center nonlinear dielectric is $3\lambda/2$ thick because this provides a more narrow discrimination for the optimal wavelength, as proven at the end of Sec. 2.3.2. The parameters for the metal are those for silver, which is used primarily for its high reflectance. The incident light's wavelength is 1 μm, and the pulse length is approximately 300 wavelengths, which is about 1 ps. The parameters for the incident pulse represent a combination of practicality and convenience, and could easily be altered to correspond to any physical system. With a titanium-sapphire laser, pulse lengths of 100 fs or less are possible. The field intensity is $E = 10000$ statvolt/cm, which corresponds to an intensity of about 50 GW/cm^2

In order to keep the numerical simulations as accurate as possible, the sampling of the optical field must be relatively high. The program samples each wavelength nearly 256 times.

In actuality, the incoming pulse should be modeled with a Gaussian envelope. However, this does not allow one to observe the subtleties of the ultra-fast dynamics inside the cavity, so the field is turned on instantaneously and remains at a constant level of intensity. However, due to the numerical restraints of the simulation, the pulse shuts off gradually using a Gaussian fit. Otherwise, the shock to the system is too much for the simulation to handle and becomes unstable (or chaotic). Figure 4.1 shows a typical incoming pulse. Note that the individual wavelengths are too close together for the eye to distinguish. Only the envelope (and a bit of aliasing) can be seen.
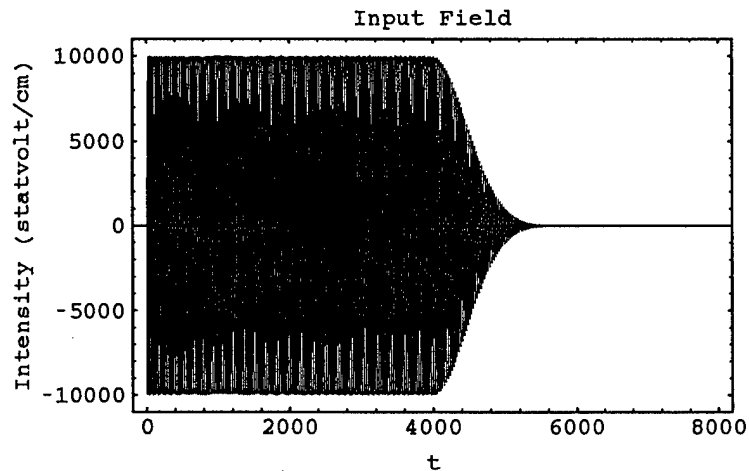
Figure 4.1. Typical input pulse.

The instantaneous turning on of the field creates an interesting phenomenon called a Sommerfeld precursor. This precursor can be seen in Fig. 4.2, which is a "snapshot" of a window taken directly from the Silicon Graphics real-time numerical simulation of an all-dielectric linear Fabry-Perot cavity. The top plot is the electric field $\mathcal{E}(z)$, the middle plot represents the linear refractive index of the cavity, and the bottom plot is the magnetic field $\mathcal{H}(z)$. This is a snapshot of the cavity shortly after the
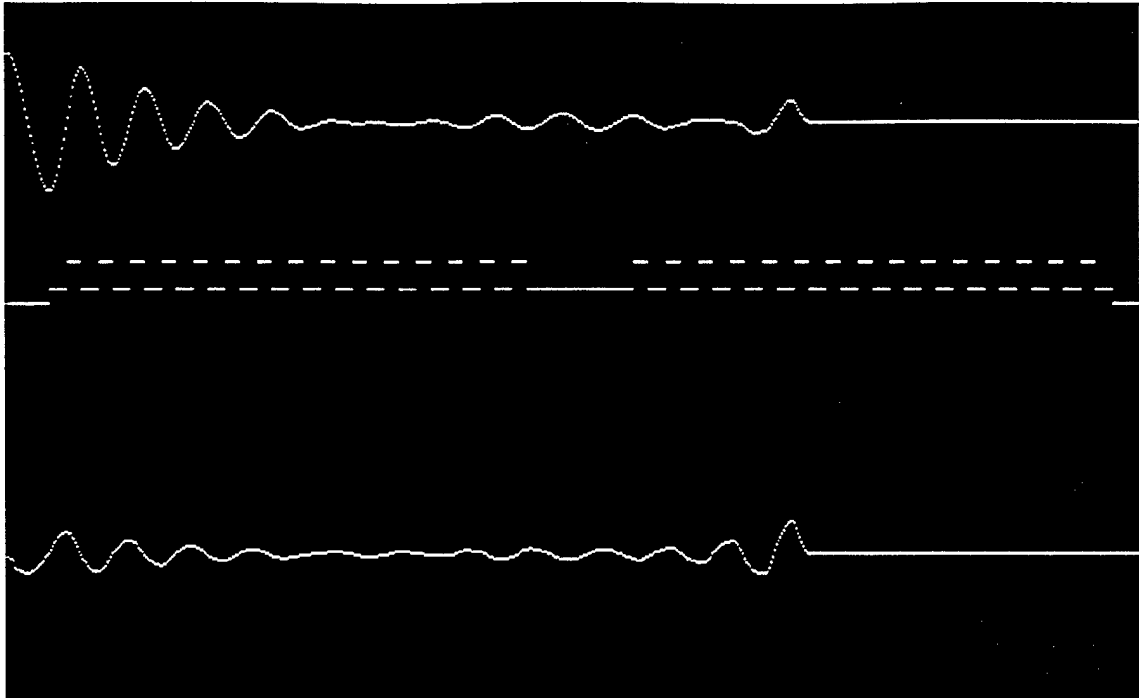
Figure 4.2. Simulation showing the Sommerfeld precursor.

field first hit the cavity. The precursor can be seen as the fairly large pulse in the right half of the picture and is moving to the right. It is composed of *very* high frequencies, since it travels faster in the dielectric than is possible for the wavelength of light that created it. It is caused by the field being turned on instantaneously and hitting the sharp barriers of the dielectrics. The other sinusoidal-shaped patterns are the beginnings of the standing-wave patterns starting to form in the structure.

After the initial precursor, the optical field generally settles down into a standing-wave pattern. Figure 4.3 is a snapshot of the same all-dielectric cavity as shown in Figure 4.2, a little later in time after the fields have begun to build up. In this figure, the standing-wave pattern can clearly be seen.
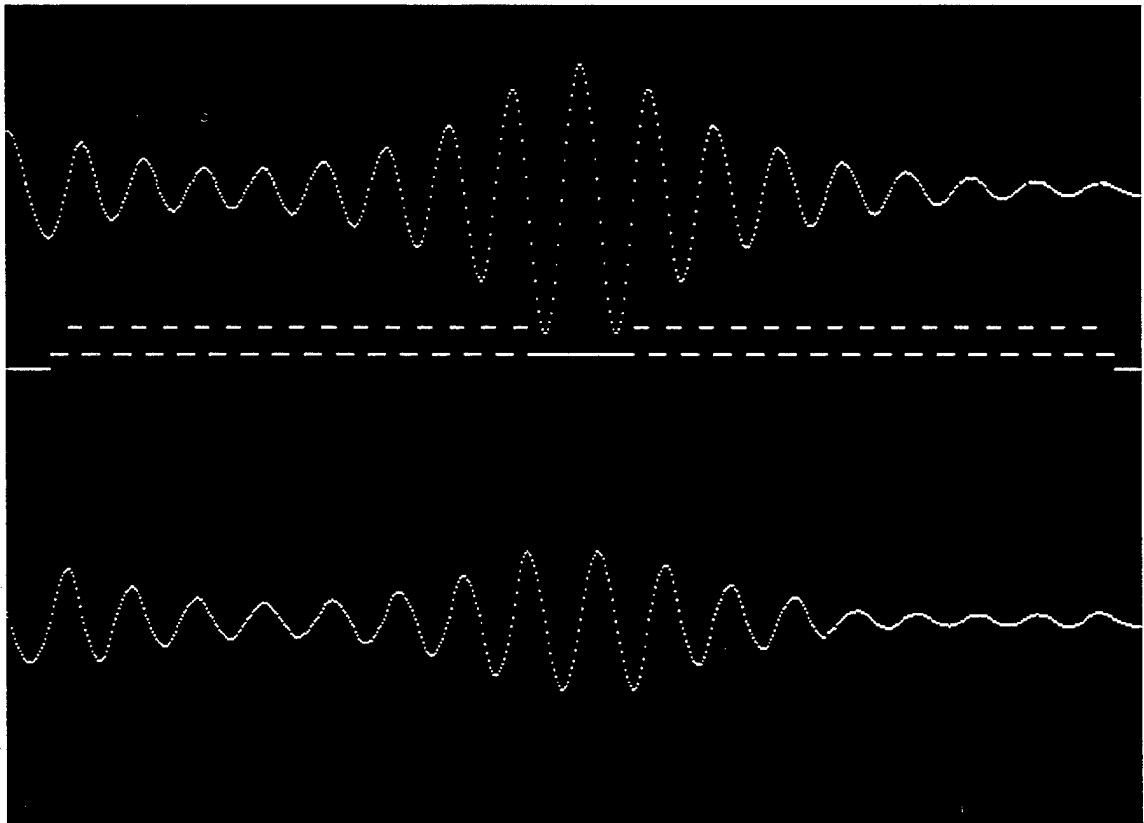
Figure 4.3. Simulation of an all dielectric cavity.

4.2 Optimizing the Cavity

Since the steady-state analysis does not include all of the factors that are present in the finite-difference time-domain algorithm, such as dispersion, the parameters for the optimal lengths of the individual sections calculated in Sec. 2.3.2 must be modified. The numbers are optimized by tweaking the individual parameters and maximizing the interior field's intensity. This is first performed on a completely linear cavity with monochromatic fields as the input. Then, the optimal wavelength for the nonlinear cavity can be determined.

4.3 Pulse Shape

Once the linear cavity has been optimized, the optimal pulse must be calculated. One way to do this is to look at the time dependence of the nonlinear index and see how it changes with the intensity. To obtain a general idea, we represent the index of refraction of the nonlinear material as

$$\frac{\partial n}{\partial t} = -\frac{n}{\tau} + \alpha I, \tag{4.1}$$

where τ and α are constants. To have the frequency of the incident light track the change in index of the cavity, we assume that the intensity remains constant. To solve Eq. (4.1), we multiply both sides by $e^{t/\tau}$. Rearranging gives

$$\frac{\partial n}{\partial t} e^{t/\tau} + \frac{n}{\tau} e^{t/\tau} = \alpha I e^{t/\tau}, \tag{4.2}$$

which simplifies to

$$\frac{\partial}{\partial t}(n e^{t/\tau}) = \alpha I e^{t/\tau}. \tag{4.3}$$

The solution to this differential equation is

$$n(t) = n_0 + \frac{\alpha I}{\tau}[1 - e^{-t/\tau}]. \tag{4.4}$$

We take the change in the resonance frequency as the first term in the Taylor series for the refractive index:

$$\omega(t) = \frac{n(t)}{n_0}\omega_0. \tag{4.5}$$

From this, we obtain the following relationship for the desired frequency of the pulse:

$$\omega(t) = \omega_i + (\omega_f - \omega_i)(1 - e^{-t/\tau}), \tag{4.6}$$

where ω_i and ω_f are the initial and final frequencies of the pulse, respectively.

The initial frequency was first estimated to be the frequency of light that optimizes the cavity when there is no nonlinear material present (only a dielectric). "Optimizes" means that the intensity in the center is built to a maximum. The final frequency was estimated to be the frequency of light that optimizes the cavity when the nonlinearity is added. This adding and subtracting of nonlinearity are done by changing the nonlinear susceptibility to suit the required needs. Once these initial estimates are made, the initial and final frequencies are tweaked using the simulation to maximize the field inside the cavity. Finally, the "chirp rate" τ was then determined using the simulation to optimize the interior field's intensity and "build-up" rate.

4.4   Results

The final simulations show a comparison of the output fields and related data of the optimally chirped pulse, a monochromatic pulse, and a chirped pulse that is not optimal. Figure 4.4 shows a snapshot of the simulation for the metal-mirrored Fabry Perot cavity after the field has built up. In this case, the top curve is the electric field, the middle curve is the magnetic field, and the bottom plot shows the relative positions of the nonlinear and metal layers. First there is air, then the exterior nonlinear dielectric, metal, interior nonlinear dielectric, metal, exterior nonlinear dielectric, and then air. Note the sharp discontinuities in the derivative of

38
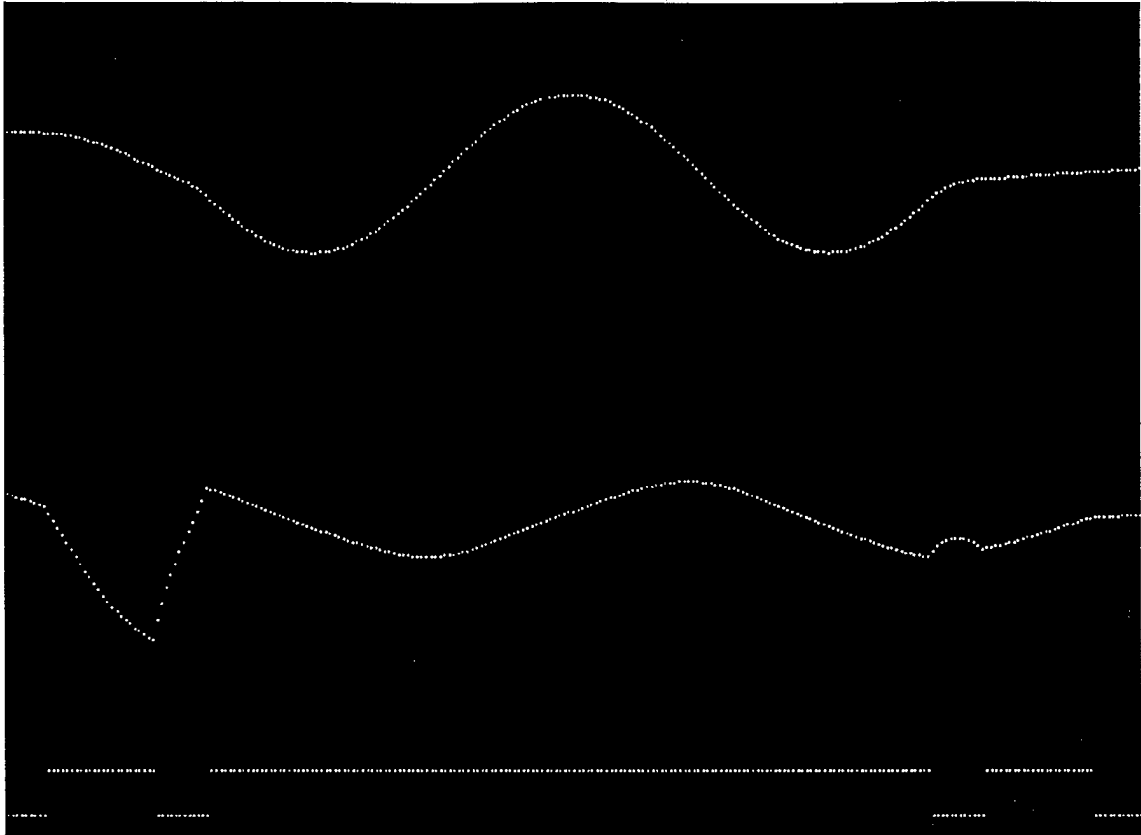
Figure 4.4. Simulation of optimally chirped pulse.

the magnetic field at the boundaries of the metal. This is due to the absorption of the metal, and is expected from Maxwell's Equations.

Figure 4.5 shows the input pulse, the maximum field strength inside the cavity, the instantaneous power density inside the cavity, and the Poynting vector inside the cavity (absorption) for a monochromatic pulse. The frequency of the pulse is such that the field inside the cavity is a maximum. Figure 4.6 shows the same data for the optimally chirped pulse for the cavity. As can be seen from the two figures, the interior field builds up much faster for the optimally chirped pulse than for the monochromatic pulse and also builds up to a slightly higher level. The interior field for the monochromatic pulse builds up fairly high at first, but then decreases, since the resonance frequency of the cavity is not being properly tracked. However, the chirped pulse continues to increases in intensity until it reaches its maximum, and
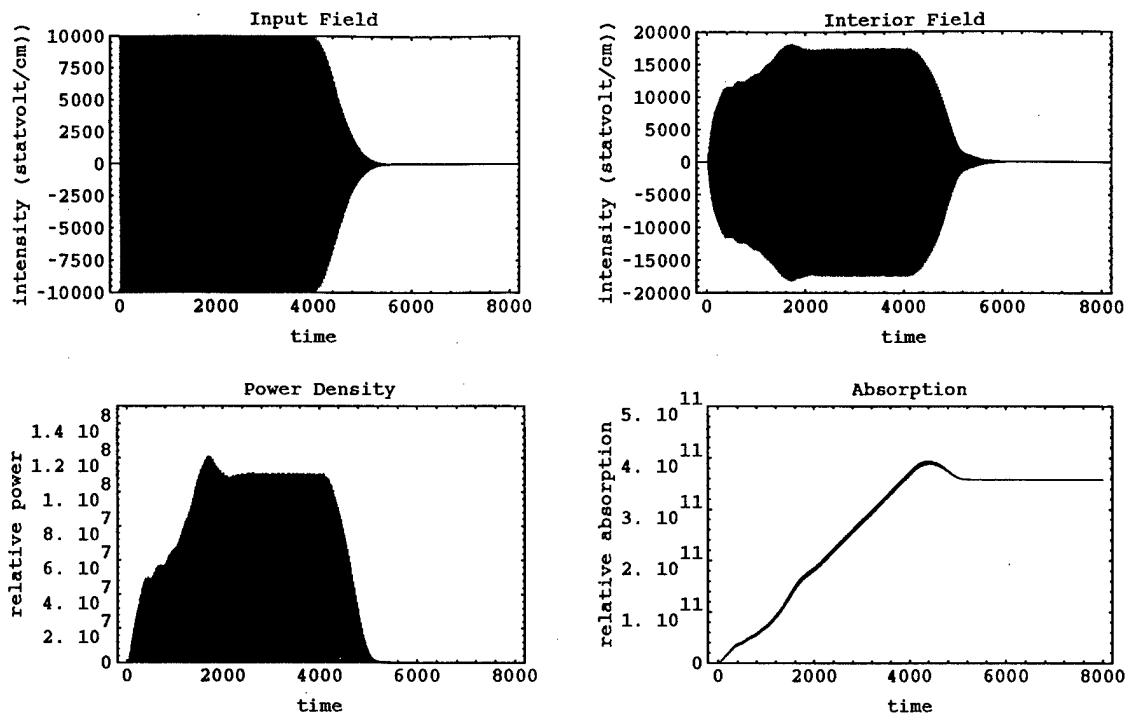
Figure 4.5. Monochromatic pulse. Optimized for nonlinear cavity.
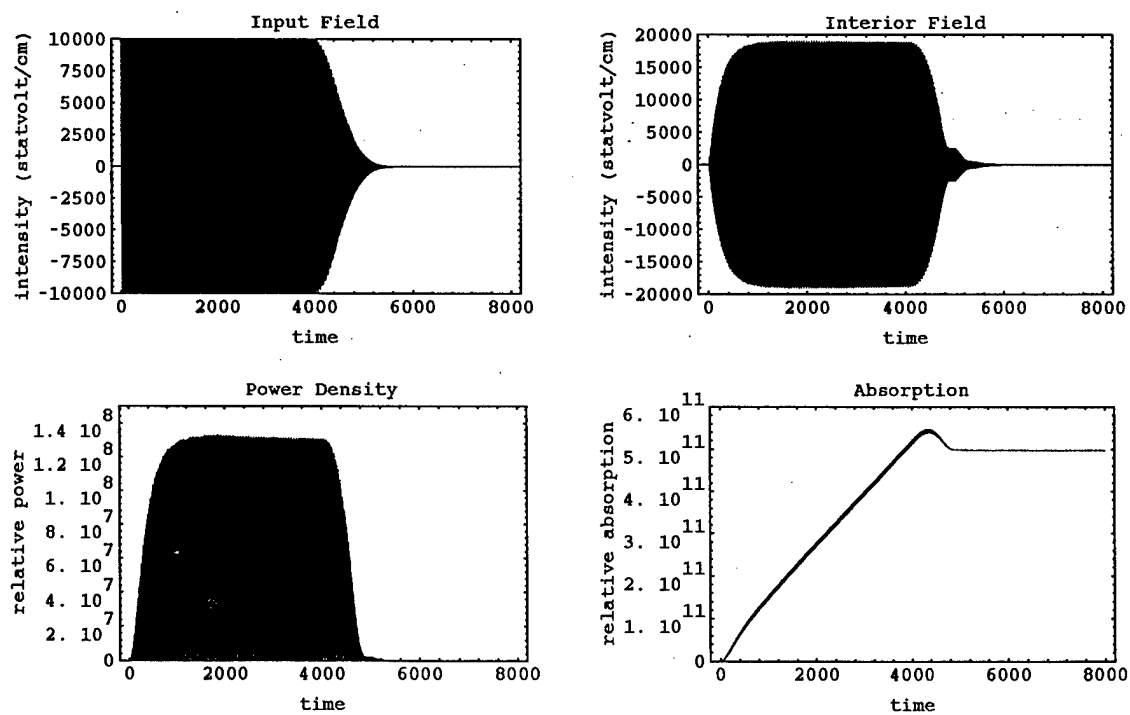
Figure 4.6. Optimally chirped pulse.

40

then holds steady. The overall power density is much greater for the chirped pulse. The final value for the absorption, which is the parameter of most interest, is also greater for the chirped pulse.

Figure 4.7 compares the absorption plots from both simulations, the top curve being from the chirped pulse.
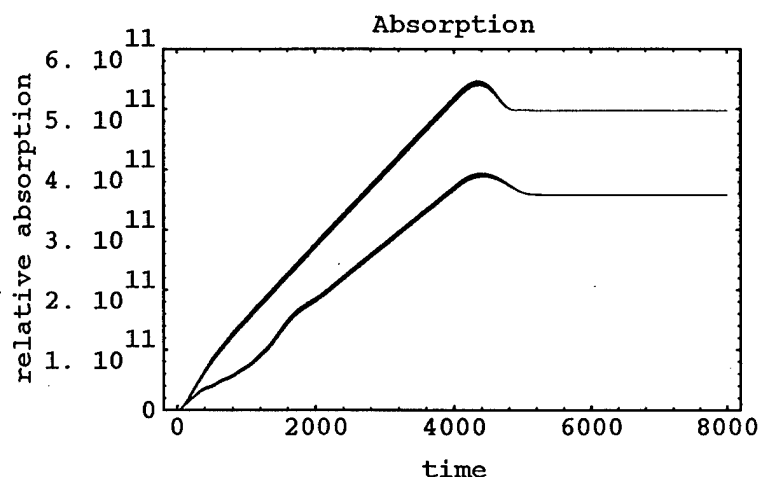
Figure 4.7. Comparison of absorption for monochromatic field and optimally chirped pulse.

Figure 4.8 shows the data for a chirped pulse where the ending frequency has been decreased by 1% from the optimal chirp. This means that the cavity is not optimized and the interior field does not build up quite as high as it could. Therefore, the absorption, too, is only about 80% of what it could be.

Figure 4.9 shows the data for a chirped pulse where the chirp rate has been decreased by 15%. This means that the frequencies change more rapidly than the refractive index of the cavity. Hence the field quickly builds up to a nominal value and then dies off. Note the absorption is quite small for this example.

Figure 4.10 shows the data for a pulse that has a reverse chirp from the optimal chirp. In other words, the starting frequency becomes the ending frequency and vice versa. As can be seen from the plots, the field never builds up appreciably and the absorption is low.
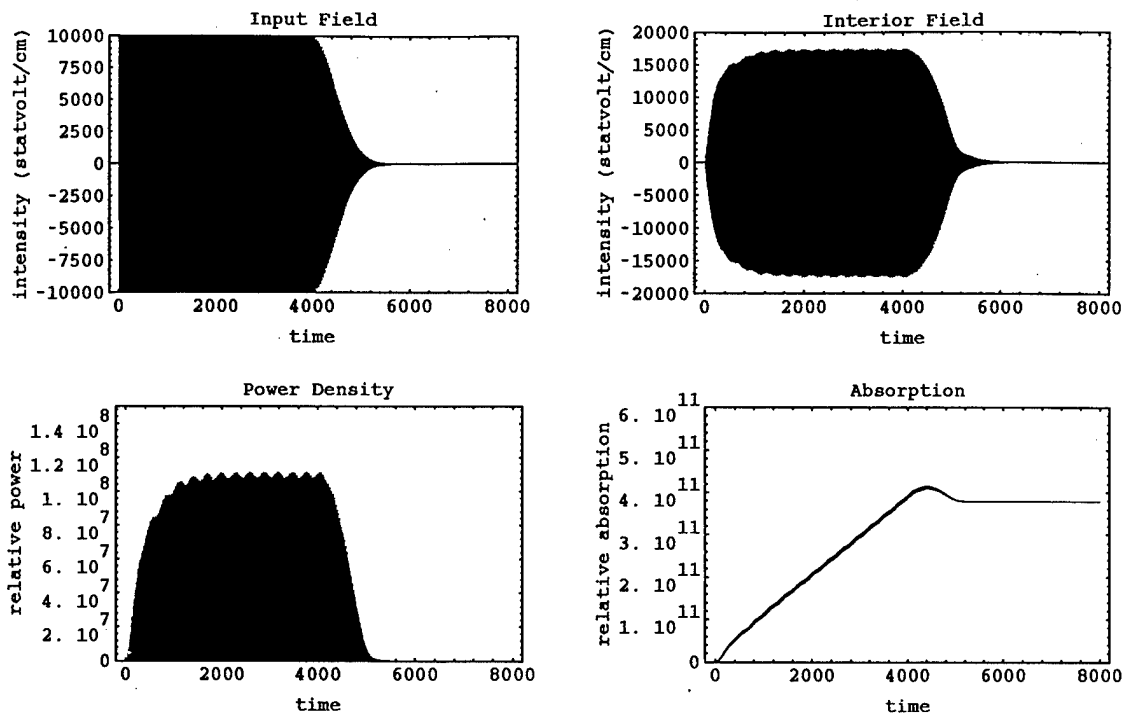
Figure 4.8. Nonoptimally chirped pulse.
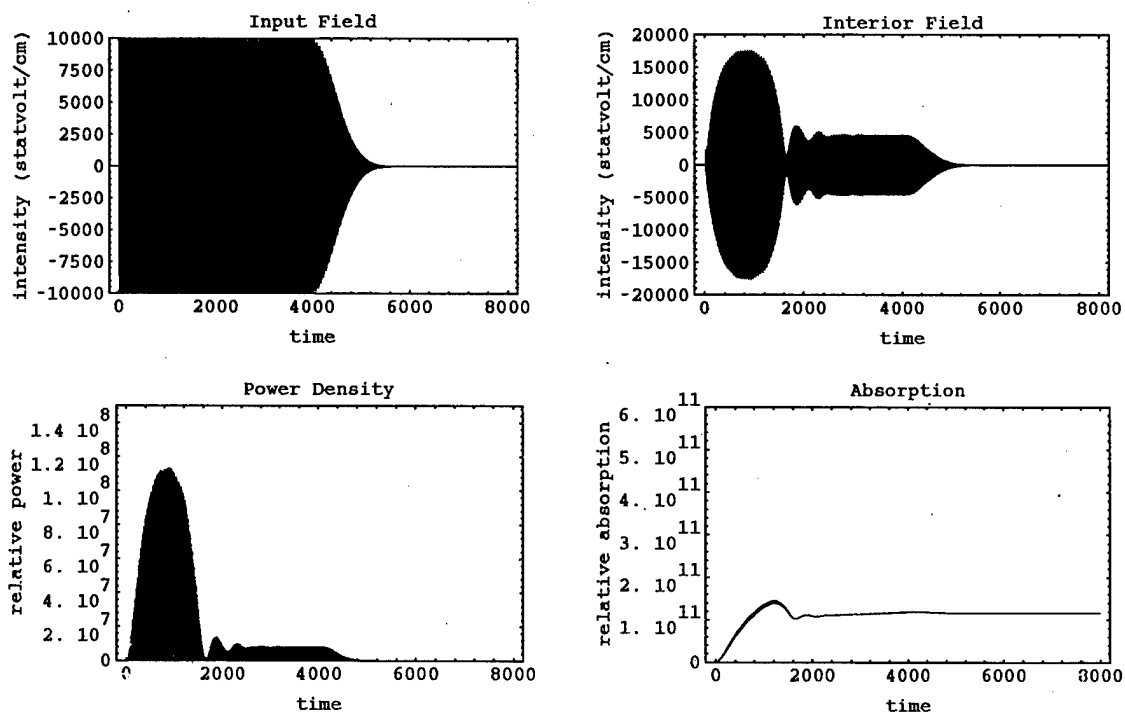
Figure 4.9. Faster chirped pulse.
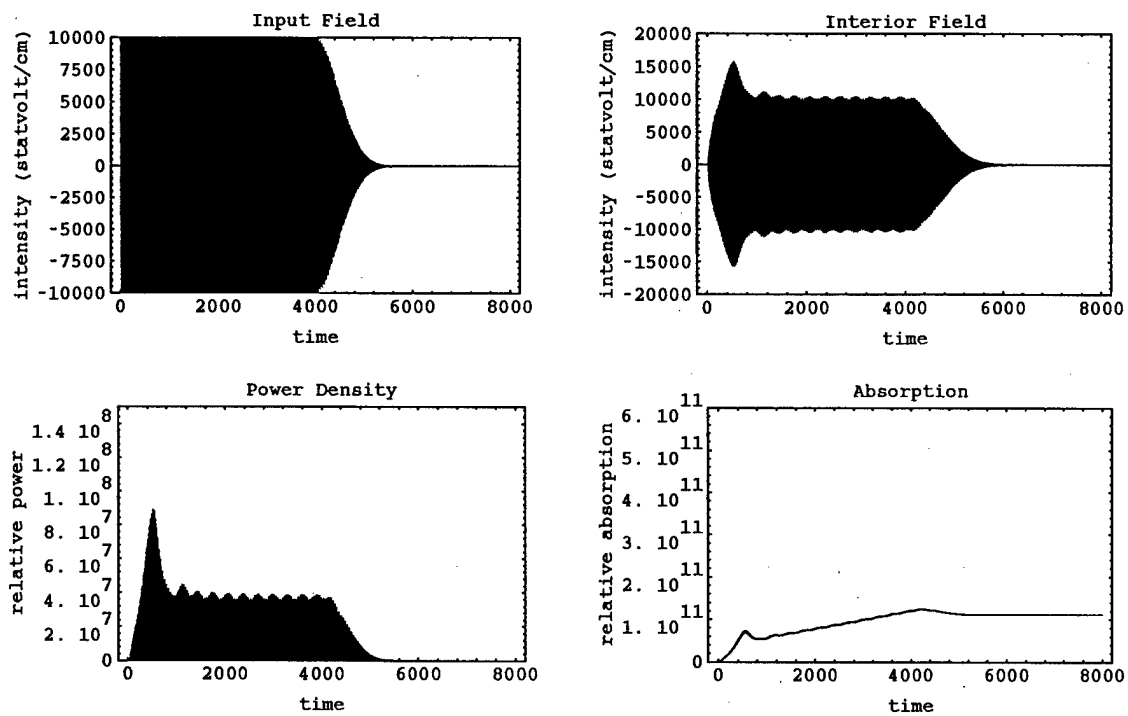
Figure 4.10. Reverse-chirped pulse.

CHAPTER 5

CONCLUSIONS

We have used finite-difference time-domain analysis to show how a nonlinear Fabry-Perot cavity can discriminate between different optical pulses.

We use steady-state analysis to determine the initial geometry of the cavity, which includes a nonlinear dielectric in the center of the cavity with thin metal films on either end. This is to insure that a large field will build up inside the cavity. For the best results, another antireflection dielectric layer is placed on the outside of the cavity. The reflectivity and interior field intensity of the cavity can be estimated using steady-state analysis. The Q-factor of the cavity can be chosen by varying the metal layer thicknesses, and by increasing the thickness of the interior nonlinear dielectric, the resonance of the cavity can be made narrower.

Because of the cross-spectral effects of the nonlinearity and also the complicated dispersion models, frequency-domain analysis is insufficient to completely explore the interaction of the cavity with ultra-fast pulses. For this reason, we use time-domain analysis. Numerical algorithms have been written to directly solve Maxwell's equations in the time domain. These algorithms include the absorption in metals and the nonlinear dispersion models.

Using these algorithms, it is possible to examine the behavior of the cavity to very short, shaped pulses. It has been shown that the cavity reacts more favorably, and absorbs more light, when the pulse shape has been dynamically matched to the time response of the cavity. This can be used, then, to create highly localized fields in space, which could theoretically be used to create a higher resolution than is normally possible with linear systems.

In the future, more optimal dispersion models will be explored and implemented in the design of the nonlinear cavities to increase the amount of discrimination between different pulse shapes.

LIST OF REFERENCES

[1] A. Taflove and K. R. Umashankar, "Review of FD-TD numerical modeling of electromagnetic wave scattering and radar cross section," *Proceedings of the IEEE*, vol. 77, pp. 682–699, May 1989.

[2] P. M. Goorjian and A. Taflove, "Direct time integration of Maxwell's equations in nonlinear dispersive media for propagation and scattering of femtosecond electromagnetic solitons," *Optics Letters*, vol. 17, pp. 180–182, Feb. 1992.

[3] P. M. Goorjian, A. Taflove, R. M. Joseph, and S. C. Hagness, "Computational modeling of femtosecond optical solitons from Maxwell's equations," *IEEE Journal of Quantum Electronics*, vol. 28, pp. 2416–2422, Oct. 1992.

[4] R. W. Boyd, *Nonlinear Optics*. New York: Academic Press, Inc., 1992.

[5] G. M. Carter, J. V. Hryniewicz, M. K. Thakur, Y. J. Chen, and S. E. Meyler, "Nonlinear optical processes in a polydiacetylene measured with femtosecond duration laser pulses," *Applied Physics Letters*, vol. 49, pp. 998–1000, Oct. 1986.

[6] G. M. Carter, "Excited-state dynamics and temporally resolved nonresonant nonlinear-optical processes in polydiacetylenes," *Journal of the Optical Society of America B*, vol. 4, pp. 1018–1024, June 1987.

[7] P. Yeh, *Optical Waves in Layered Media*. New York: John Wiley & Sons, 1988.

[8] M. Born and E. Wolf, *Principles of Optics*, 6th ed. Oxford: Pergamon Press, 1984.

[9] K. Blow and D. Wood, "Theoretical description of transient stimulated Raman scattering in optical fibers," *IEEE Journal of Quantum Electronics*, vol. 25, pp. 2665–2673, Dec. 1989.

APPENDIX A

STEADY-STATE CODE

A.1 Matlab Code

The following program was written in Matlab and was used to generate Figs. 2.4 and 2.5.

```
% This program plots Reflectance vs. Number of Layers
% for layered dielectric stacks
%
n(1)=1.0;        n(2)=1.33;      n(3)=1.6;       n(4)=1;
lambda=1;
a=lambda/(4*n(2));       b=lambda/(4*n(3));

for i = 1:4, k(i)=2*pi*n(i)/lambda;, end
d1=[1 1; n(1) -n(1)];    d2=[1 1; n(2) -n(2)];
d3=[1 1; n(3) -n(3)];    d4=[1 1; n(4) -n(4)];
p2=[exp(j*k(2)*a) 0; 0 exp(-j*k(2)*a)];
p3=[exp(j*k(3)*b) 0; 0 exp(-j*k(3)*b)];
A=exp(j*k(2)*a)*(cos(k(3)*b)+.5*j*(k(3)/k(2)+k(2)/k(3))*
    sin(k(3)*b));
B=exp(-j*k(2)*a)*.5*j*(k(3)/k(2)-k(2)/k(3))*sin(k(3)*b);
C=-exp(j*k(2)*a)*.5*j*(k(3)/k(2)-k(2)/k(3))*sin(k(3)*b);
D=exp(-j*k(2)*a)*(cos(k(3)*b)-.5*j*(k(3)/k(2)+k(2)/k(3))*
    sin(k(3)*b));
for m=1:32
    v=inv(d2)*d4*[1; 0];
    for i = m:-1:2
        v=[A B; C D]*v;
    end
    v=inv(d1)*d3*p3*inv(d3)*d2*p2*v;
```

```
    y(m)=abs(v(2)/v(1))^2;
    x(m)=m;
end
axis([0,m,0,1])
plot(x,y,'o')
```

The following program was written in Matlab and was used to generate Fig. 2.6.

```
% This program plots Reflectance vs. Change in Index for one of the
% layers of a layered dielectric stack
%
n1=1.0;          n2=8/6;          n3=1.6;          n4=1;
m=16;            lambda=1;
a=lambda/(4*n2);          b=lambda/(4*n3);
n3_start=1.5;    n3_stop=2.5;

k(1)=2*pi*n1/lambda;
k(2)=2*pi*n2/lambda;
k(4)=2*pi*n4/lambda;
d1=[1 1; n1 -n1];
d2=[1 1; n2 -n2];
d4=[1 1; n4 -n4];
p2=[exp(j*k(2)*a) 0; 0 exp(-j*k(2)*a)];
for n3=n3_start:.01:n3_stop
    k(3)=2*pi*n3/lambda;
    d3=[1 1; n3 -n3];
    p3=[exp(j*k(3)*b) 0; 0 exp(-j*k(3)*b)];
    A=exp(j*k(2)*a)*(cos(k(3)*b)+.5*j*(k(3)/k(2)+k(2)/k(3))*
        sin(k(3)*b));
    B=exp(-j*k(2)*a)*.5*j*(k(3)/k(2)-k(2)/k(3))*sin(k(3)*b);
    C=-exp(j*k(2)*a)*.5*j*(k(3)/k(2)-k(2)/k(3))*sin(k(3)*b);
    D=exp(-j*k(2)*a)*(cos(k(3)*b)-.5*j*(k(3)/k(2)+k(2)/k(3))*
        sin(k(3)*b));
    v=inv(d2)*d4*[1; 0];
    for i = m:-1:2
        v=[A B; C D]*v;
    end
    v=inv(d1)*d3*p3*inv(d3)*d2*p2*v;
    x(n3*100-149)=n3;
    y(n3*100-149)=abs(v(2)/v(1))^2;
end
axis([n3_start,n3_stop,0,1])
plot(x,y)
```

A.2   Mathematica Code

The following is the Mathematica code used for the steady-state simulations of Chapter 2.

```
(* Set up matrices and constants *)
m[n_,l_]:=N[{{Exp[2 Pi I n l],Exp[-2 Pi I n l]},
    {n Exp[2 Pi I n l],-n Exp[-2 Pi I n l]}}];
im[n_,l_]:=Inverse[m[n,l]];
m2[n_,l_]:=N[{{Exp[2 Pi I n l],0},{0,Exp[-2 Pi I n l]}}];
nm=0.2378 +  6.78702 I;
nd=1.452;


(* transmission of nd nm nd nm nd. *)

f[la_,lb_,lm_,n_]:=im[1,0].m[n,-la].im[n,0].m[nm,-lm].im[nm,0].
    m[n,-lb].im[n,0].m[nm,-lm].im[nm,0].m[n,-la].im[n,0].m[1,0].{1,0};
f2[la_,lb_,lm_,n_]:=m2[n,-lb/2].im[n,0].m[nm,-lm].im[nm,0].m[n,-la].
    im[n,0].m[1,0].{1,0};
r[la_,lb_,lm_,n_]:=1/Abs[f[la,lb,lm,n][[1]]]^2
r2[la_,lb_,lm_,n_]:=n Abs[f2[la,lb,lm,n][[1]]+f2[la,lb,lm,n][[2]]]^2/
    Abs[f[la,lb,lm,n][[1]]]^2;


(* Sample Plot *)

Plot[r2[.160174,x,0.05,nd],{x,0,.5},PlotRange->All,Frame->True,
    FrameLabel->{"center dielectric thickness","relative intensity"}]
FindMinimum[-r2[.160174,y,0.05,nd],{y,.2,.3}]
```

APPENDIX B

FD-TD CODE

The following C code is the FD-TD code used for the simulations in Chapter 4.

```c
/* nonlin.h*/

#include <math.h>
#include <stdio.h>
#include <stdlib.h>

void nonlin(float, int);
void epsilon(float*, int*, int*);
void graphics(float*, int*, int*);
void write_file(char filename[], double*, float);
void plot(int, double*, double*, double*, double*, double*, double*,
    double*, double*, int);

#define Pi 3.14159265359
#define twoPi 6.28318530717959
#define c0 3E10
#define TRUE 1
#define FALSE 0
#define RGB_BLACK 0x000000
#define RGB_WHITE 0xffffff
#define RGB_YELLOW 0x00ffff
#define RGB_CYAN 0x00ffff
#define RGB_MAGENTA 0xff00ff
#define RGB_BLUE 0xff0000
#define RGB_RED 0x0000ff
#define RGB_GREEN 0x00ff00

#define SWAP(a,b) tempr=(a);(a)=(b);(b)=tempr
```

```c
/* vars.h */

#define period          256      /* Number of pixels per wavelength */
#define xstop           250      /* Number of points in simulation  */
#define wavelength      1E-4     /* Wavelength in cm                */
#define Efield          10000    /* Mag. of E-field in statvolt/cm  */
#define nn              256      /* Number of points in FFT         */
#define pulselength     156.25   /* Length of pulse in wavelengths  */
#define maxiter         80000    /* number of iterations to run     */
#define sigma_squared   (pulselength*period/6.0 * pulselength*period/
                           6.0)
#define period2         246.0    /* Optimum for linear cavity       */
#define rate            18000.0  /* chirp rate                      */


#define power_spectrum  FALSE    /* Power spectrum on?              */
#define IO_pulses       TRUE     /* Input Output chart on?          */
#define simulation      TRUE     /* Real-time simulation on?        */
#define power_density   TRUE     /* Average power density on?       */
#define absorption      TRUE     /* Calculate absorpton?            */
#define step            10       /* sampling step                   */


#define const1          1.89235E32    /* Constant for metal          */
#define const2          6.60764       /* Constant for metal          */
#define beta            -2.36136E14   /* Constant for metal          */


#define epss            5.25     /* epsilon at w=0            */
#define epsi            2.25     /* epsilon at w=infinity     */
#define w0              4.0E14   /* resonant frequency        */
#define delta0          2.0E9    /* delta for nonlinear disp. */
#define X31             9.8E-10  /* X3 for nonlinear disp.    */
#define alpha           .1       /* instantaneous nonlinear.  */
#define t1              12.2E-15 /* time const. 1 for disp.   */
#define t2              320.0E-15 /* time const. 2 for disp.  */


#define start           10       /* layer starts here         */
#define layers          1        /* number of layers (ends)   */


#define film_a_on       TRUE
#define film_a_length   24
#define film_a_eps      2.25
#define film_a_nonlin   TRUE
#define film_a_metal    FALSE


#define film_b_on       TRUE
#define film_b_length   12
```

```
#define film_b_eps       1.0
#define film_b_nonlin    FALSE
#define film_b_metal     TRUE

#define film_c_on        TRUE
#define film_c_length    158
#define film_c_eps       film_a_eps
#define film_c_nonlin    TRUE
#define film_c_metal     FALSE

#define film_d_on        TRUE
#define film_d_length    film_b_length
#define film_d_eps       1.0
#define film_d_nonlin    FALSE
#define film_d_metal     TRUE

#define film_e_on        TRUE
#define film_e_length    film_a_length
#define film_e_eps       film_a_eps
#define film_e_nonlin    film_a_nonlin
#define film_e_metal     film_a_metal


#define yscale           20      /* multiplier for scaling  y       */
#define yoffset          600     /* offset for various windows      */
```

```
/* main.c */

#include "nonlin.h"
#include "vars.h"

double  data[nn+3];
int     dude[128];
long    win1, win2, win3;

void main()
{
    float period3=170.88;   /* Optimum for nonlinear cavity          */
    int   offset=0;

    for (period3=255.0; period3<=255.0; period3+=1) {
        printf("period3 = %.2f\n", period3);
        nonlin(period3, offset);
    }
}
```

```c
/* nonlin.c */

#include "nonlin.h"
#include "vars.h"

void nonlin(float period3, int offset)
{
    /* Declare variables */
    extern double   data[];
    extern long     win1, win2, win3;
    long vert[2];
    short val;
    int i, j, a=0, b=1, c=2, tempr,
        X3[xstop+1], *pX3=X3, sigma[xstop+1], *psigma=sigma, iter = 0;
    float   eps[xstop+1], *peps=eps;
    double  E[3][xstop+2], *pE,
            H[3][xstop+1], *pH,
            *pdata1=data, *pdata2=data,
            D[3][xstop+1], F[3][xstop+1], G[3][xstop+1], delt, coef,
            input[maxiter/step+1], *pinput=input,
            output[maxiter/step+1], *poutput=output,
            output2[maxiter/step+1], *poutput2=output2,
            output3[maxiter/step+1], *poutput3=output3,
            output4[maxiter/step+1], *poutput4=output4,
            absorp, *pabsorp,
            back1=0, back2=0, back3=0,
            delz = wavelength / period,
            a1, a2, b1, b2, c1, c2, const3, const4, const5,
            w00_2, w10_2, delta1;

    /* Initialize variables and set eps */
    pabsorp=&absorp;
    *pabsorp=0;
    pE=&E[0][0];
    pH=&H[0][0];
    for (i=0; i<=2; i++) {
        for (j=0; j<=xstop; j++) {
            E[i][j] = 0;    H[i][j] = 0;
            D[i][j] = 0;    F[i][j] = 0;    G[i][j] = 0;
        }
        E[i][xstop+1] = 0;
    }
    delt = delz / c0;
    coef = delt * c0 / delz;
    w00_2 = pow(w0,2);
```

```
w10_2 = 1/pow(t1,2) + 1/pow(t2,2);
delta1 = 2/t2;
epsilon(peps, pX3, psigma);

/* Initialize graphics screens */
graphics(peps, pX3, psigma);

/* main program */
while (iter <= maxiter)
{
    if (iter<pulselength*period)
        E[a][0] = (input[iter/step]=Efield*sin(twoPi*
            (iter/period3 + rate*(1/period3-1/period2)*
            exp(-iter/rate))));
    else
        E[a][0] = (input[iter/step]=Efield*sin(twoPi*
            (iter/period3 + rate*(1/period3-1/period2)*
            exp(-iter/rate))) * exp(-pow(iter-pulselength*
            period,2)/sigma_squared));
    back3=back2; back2=back1; back1=E[a][0];
    E[a][0] = E[a][0] + E[b][1] - back3;
    H[a][0] = H[b][0] + coef * (E[b][0] - E[b][1]);

    pdata2++;
    *pdata2=(E[b][xstop+1] = E[c][xstop]);
    if (pdata2-pdata1 >= nn) pdata2 = pdata1;

    for (i=1; i<=xstop; i++) {
        H[a][i] = H[b][i] + coef * (E[b][i] - E[b][i+1]);

        if (sigma[i] != 0) {
            E[a][i] = (c0 * ((-H[a][i]+H[b][i]+H[a][i-1]-
                H[b][i-1])/(delt*delz) + beta*(H[b][i]-
                H[b][i-1])/delz)-(-2*const2/pow(delt,2)+beta*
                const2/delt+const1)*E[b][i] - const2/pow(delt,2)*
                E[c][i]) / (const2*(1/pow(delt,2)-beta/delt));
        }

        else if (X3[i] != 0) {
            D[a][i] = D[b][i]+(coef/peps[i])*(H[a][i-1]-H[a][i]);
            const3=epsi+alpha*X31*pow(E[b][i],2);
            const4=(epss-epsi)/const3;
            const5=E[b][i]/const3;
            a1=1/(w00_2*pow(delt,2)) + delta0/(2*w00_2*delt) +
                (1+const4)/2;
```

55

```
                b1=const4*(1-alpha)*X31*E[b][i]/2;
                c1=const4*(D[a][i]+D[c][i])/2 - 1/w00_2*(-2*F[b][i]+
                    F[c][i]) / pow(delt,2) + delta0/w00_2*F[c][i]/
                    (2*delt) - (1+const4)*F[c][i]/2 - const4*(1-
                    alpha)*X31*E[b][i]*G[c][i]/2;
                a2=const5/2;
                b2=1/(w10_2*pow(delt,2)) + delta1/(2*w10_2*delt) +
                    (1+(1-alpha)*X31*E[b][i]*const5)/2;
                c2=const5*(D[a][i]+D[c][i])/2 - 1/w10_2*(-2*G[b][i]+
                    G[c][i])/pow(delt,2) + delta1/w10_2*G[c][i]/
                    (2*delt) - (1+(1-alpha)*X31*E[b][i]*const5)*
                    G[c][i]/2 - const5*F[c][i]/2;
                F[a][i]=(b2*c1-b1*c2)/(a1*b2-a2*b1);
                G[a][i]=(a1*c2-a2*c1)/(a1*b2-a2*b1);
                E[a][i]=(D[a][i]-F[a][i]-(1-alpha)*X31*E[b][i]*
                    G[a][i])/const3;
            }

        else
            E[a][i] =E[b][i]+(coef/peps[i])*(H[a][i-1]-H[a][i]);
        }


    plot(iter, pE, pH, pinput, poutput, poutput2, poutput3,
        poutput4, pabsorp, offset);


    a--;  if (a <= -1) a = 2;
    b--;  if (b <= -1) b = 2;
    c--;  if (c <= -1) c = 2;
    iter++;
}
close_graphics(pinput, poutput, poutput2, poutput3, poutput4,
    period3);
tempr=0;
for (i=500; i<=maxiter/step; i++)
    tempr+=poutput4[i];
back1 = tempr;
back2 = maxiter;
back3 = step;
printf("  average zero crossing at: %.2f\n", back1/(back2/
    back3-500.0));
}
```

```c
void epsilon(float *eps, int *X3, int *sigma)
{
    int i, j, k;

    i = 0;
    while (i < start) {
        eps[i] = 1;                X3[i] = 2 * twoPi * 0;
        sigma[i] = 0;
        i++;
    }
    j = 0;
    while (j < layers) {
        k = 0;
        while ((k < film_a_length) && (film_a_on == TRUE)) {
            eps[i] = film_a_eps;
            X3[i] = film_a_nonlin;
            sigma[i] = film_a_metal;
            i++; k++;
        }
        k = 0;
        while ((k < film_b_length) && (film_b_on == TRUE)) {
            eps[i] = film_b_eps;
            X3[i] = film_b_nonlin;
            sigma[i] = film_b_metal;
            i++; k++;
        }
        j++;
    }
    k = 0;
    while ((k < film_c_length) && (film_c_on == TRUE)) {
        eps[i] = film_c_eps;
        X3[i] = film_c_nonlin;
        sigma[i] = film_c_metal;
        i++; k++;
    }
    j = 0;
    while (j < layers) {
        k = 0;
        while ((k < film_d_length) && (film_d_on == TRUE)) {
            eps[i] = film_d_eps;
            X3[i] = film_d_nonlin;
            sigma[i] = film_d_metal;
            i++; k++;
        }
        k = 0;
```

```
        while ((k < film_e_length) && (film_e_on == TRUE)) {
            eps[i] = film_e_eps;
            X3[i] = film_e_nonlin;
            sigma[i] = film_e_metal;
            i++; k++;
        }
        j++;
    }
    while (i <= xstop) {
        eps[i] = 1;                 X3[i] = 2 * twoPi * 0;
        i++;
    }
}
```

```c
/* graphics.c */

#include "nonlin.h"
#include "vars.h"

void close_graphics(double *pinput, double *poutput,
    double *poutput2, double *poutput3, double *poutput4,
    float parameter)
{
    FILE *fp;
    int i;

    if (IO_pulses == TRUE)
        write_file("input", pinput, parameter);

    if (IO_pulses == TRUE)
        write_file("output", poutput, parameter);

    if (power_density == TRUE)
        write_file("output2", poutput2, parameter);

    if (absorption == TRUE) {
        write_file("output3", poutput3, parameter);
        write_file("output4", poutput4, parameter);
    }
}


void write_file(char filename[], double *output, float parameter)
{
    FILE *fp;
    int i;
    char tmp[32], newfilename[32];

    strcpy(newfilename, filename);
    sprintf(tmp, "_%.2f", parameter);
    strcat(newfilename, tmp);
    if ((fp = fopen(newfilename, "w+")) == NULL) {
        printf("cannot open file '%s'\n", newfilename);
        exit(1);
        }
    for (i=0; i<=maxiter/step; i++)
        fprintf(fp, "%f\n", output[i]);
    fclose(fp);
}
```

```c
/* plot.c */

#include "nonlin.h"
#include "vars.h"

int sgn(double);

void plot(int iter, double *pE, double *pH, double *pinput,
    double *poutput, double *poutput2, double *poutput3,
    double *poutput4, double *pabs, int offset)
{
    /* Declare variables */
    extern int dude[];
    double tmp;
    int i, mini=0,
        a = start + layers * (film_a_length + film_b_length),
        b = a + film_c_length - 1,
        b1= a + film_c_length/2,
        b2= b1- film_c_length/6,
        b3= b1+ film_c_length/6;

    /* Keep track of output of E-field */

    i = b2;
    tmp = sgn(pH[i+1]-2*pH[i]+pH[i-1]);
    while(tmp == sgn(pH[i+1]-2*pH[i]+pH[i-1]) && i<b3) i++;
    dude[iter-64*(iter/64)] = i;

    if (iter % step == 0) {
        poutput[iter/step] = pE[xstop];
        mini=0;
        for (i=0; i<=63; i++)
            mini+=dude[i];
        poutput4[iter/step] = mini/64;
    }


    /* Calculate instantaneous power density */
    if (power_density == TRUE && iter % step == 0) {
        tmp = 0;
        i = a;
        while (i < film_c_length) {
            tmp += pow(pE[i], 2);
            i++;
        }
```

```
            poutput2[iter/step] = tmp / film_c_length;
        }


    /* Calculate total absorpton */
    if (absorption == TRUE) {
        *pabs += pE[a]*pH[a]-pE[b]*pH[b];
        if (iter % step == 0)
            poutput3[iter/step] = *pabs;
    }
}

int sgn(double number)
{
    if (number > 0) return 1;
    else if (number < 0) return -1;
    else return 0;
}
```

THESIS ABSTRACT

THE OHIO STATE UNIVERSITY
GRADUATE SCHOOL

NAME: Breslin, Michael, Craig   **QUARTER/YEAR:** Spring 1994

DEPARTMENT: Materials Science and Engineering

DEGREE: Master of Science

ADVISOR'S NAME: Fraser, Hamish, L.

TITLE OF THESIS: Transformation Kinetics of Al_2O_3/Al Co-Continuous Ceramic/Metal Composite Materials (C^4) Produced by a Displacement Reaction Between Liquid Al and Fused SiO_2

Studies of the transformation kinetics and resulting microstructures of C^4 materials processed at various temperatures are presented. C^4 materials are produced through a displacement reaction between solid silica and molten aluminum. Evidence suggests that three distinct, temperature related processing regimes exist, each of which yields characteristic kinetic behavior and microstructures. Through the identification of the various phases and morphologies present in the microstructure, coupled with the observed kinetic behavior, a transformation mechanism for the evolution of the material is proposed.

Hamish L. Fraser, Advisor

Transformation Kinetics of Al_2O_3/Al Co-Continuous Ceramic/Metal Composite Materials (C^4) Produced by a Displacement Reaction Between Liquid Al and Fused SiO_2

A Thesis

Presented in Partial Fulfillment of the Requirements for the Degree

Master of Science

in the Graduate School of The Ohio State University

by

Michael Craig Breslin, B.S.

● ● ● ● ●

The Ohio State University

1994

Master's Examination Committee:

Dr. Hamish L. Fraser

Dr. Glenn S. Daehn

Approved by:

_____

Advisor
Department of Materials
Science and Engineering

In loving memory of my Grandfather, Lewis Breslin --

"The fire extinguisher is over here and
the breaker is over there; yell if you get hurt."

ACKNOWLEDGMENTS

VITA

June 9, 1967	Born - Cleveland, Ohio
June, 1990	B.S. Metallurgical Engineering, The Ohio State University
June, 1990 - July, 1991	Graduate Research Associate Department of Materials Science and Engineering, The Ohio State University
July 1991 - Present	National Defense Science and Engineering Graduate Fellow Department of Materials Science and Engineering, The Ohio State University

SELECTED PUBLICATIONS

M.C. Breslin, L. Xu, G.S. Daehn and H.L. Fraser, "Applications of Co-Continuous Ceramic Composite Materials for Automotive Applications," *SAE Technical Paper Series* #930184, 1993.

M.C. Breslin, J.Ringnalda, J.Seeger, A.L. Marasco, G.S. Daehn and H.L. Fraser, "Alumina/Aluminum Co-Continuous Ceramic Composite (C^4) Materials Produced by Solid/Liquid Displacement Reactions: Processing Kinetics and Microstructures," *Proceedings of the 18th Annual Conference on Composites and Advanced Ceramic Materials*, 1994.

J. Ringnalda, M.C. Breslin, J.Seeger, D. LeJeune, G.S. Daehn and H.L. Fraser, "Development of Co-Continuous Ceramic Composite Materials for Specific Applications," *SAE Technical Paper Series* #940850, 1994.

FIELDS OF STUDY

Major Field: Materials Science and Engineering

TABLE OF CONTENTS

LIST OF FIGURES

LIST OF TABLES

CHAPTER I

INTRODUCTION

The development of new materials to meet the needs of high performance applications has become an increasingly important research area. Advancing technology is placing demands on material performance which exceeds existing material properties. While improving properties of existing materials may help narrow the gap between application requirements and material performance, often unique and unusual combinations of properties are required to satisfy these technological demands. One promising approach of achieving this is to exploit the possibilities offered by composite materials.

Composites allow new material systems to be designed and fabricated which exhibit both significant improvements in and the ability to tailor properties. Considering the virtually infinite potential constituent combinations and processing conditions, the number of possible composite systems is staggering. Examination of virtually any source of materials science literature suggests that the limit on composite variations is dictated merely by the creativity of the researcher.

As a means of characterizing composite structures, several classifications have been accepted. Specifically, three main genera of inorganic composite materials have been suggested: Ceramic Matrix Composites (CMC), Metal Matrix Composites (MMC), and the lesser known Interpenetrating Phase Composites (IPC) (It should be noted that intermetallic matrix composites also exist, however they will not be discussed here). The first two of these classifications feature discrete reinforcing phases dispersed within a continuous matrix. The former is defined by a continuous ceramic matrix, and the latter by a continuous metal matrix. In both cases the reinforcement can be comprised of metal, ceramic, intermetallic, etc. or any combination thereof.

An example of a commercial MMC material is SiC reinforced Al [1]. Currently being evaluated as a candidate material for use as an automotive brake rotor, the addition of SiC increases the wear resistance and strength of the Al while still yielding a lightweight, thermally conductive material. Commercial use of CMC materials can be exemplified by fiber reinforced Al_2O_3 [2]. In this case, the addition of fibers to an otherwise brittle matrix allows graceful failure of the structure when critical load conditions are exceeded. CMCs of this type are currently being considered for various jet turbine applications.

In contrast to MMC and CMC materials, IPC materials feature two distinct (but not discrete) phases which interpenetrate each other, usually in three-dimensions. Often referred to as co-continuous composites, this genus

offers excellent potential for producing materials with truly unique combinations of properties. Constituents with complementary properties can be combined in a co-continuous manner yielding a composite structure which features some of the best features of both. For example by combining metal and ceramic phases, a composite can be produced which exhibits high stiffness, good hardness, and a high ultimate application temperature (i.e. ceramic) as well as good toughness, and appreciable electrical and thermal conductivity (i.e. metal).

Theoretically, IPC materials offer the ability to produce tailorable composite materials featuring a nearly infinite range of properties. Unfortunately, in the case of these materials, theory and practice do not entirely intersect. Due to the inherent incompatibilities of various constituents as well as the difficulty of combining the various phases in a three dimensionally interpenetrated network, only a limited number of IPC systems have been identified.

The difficulty of designing a new IPC system was circumvented by serendipity in 1989 during an undergraduate laboratory experiment at the Ohio State University. The purpose of the experiment was to measure the active oxidation rate of a molten Al-Mg-Si alloy at high temperatures (T>1000°C). The experimental set-up required a refractory vessel capable of holding the molten alloy for periods of time longer than 24 hours. Of the few materials capable of withstanding the strong reducing nature of the alloy, Al_2O_3 was the most readily available. Thus an attempt of obtaining an Al_2O_3

crucible was made. The crucible which was obtained, however, was not the desired Al_2O_3, but composed of fused SiO_2. Since it was believed to be composed of Al_2O_3, the vessel was used in the experiment without alteration.

SiO_2 refractories are commonly used in processing molten Al, however, the oxidation/reduction reaction

$$4\,Al + 3\,SiO_2 \rightarrow 2\,Al_2O_3 + 3\,[Si]_{Al} \qquad (1)$$
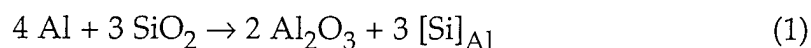
is known to occur (the product Si dissolves into the melt). While the thermodynamics of this reaction are favorable, the kinetics can be quite slow, thus for melting of Al at reasonable temperatures and short periods of time SiO_2 crucibles are acceptable. Al is seldom taken to temperatures greater than 50 percent above its melting temperature ($T_m \approx 660°C$) due to excessive H_2 dissolution and the ensuing porosity which would form in the solidified structure. Furthermore, it is unlikely that Al would be held at molten temperatures for more than several minutes.

If the crucible had been identified as fused SiO_2 prior to the experiment, it would not have been used. Although no evidence was available to predict exactly what would happen, it might be inferred that Equation 1 would proceed at a relatively rapid rate reducing a large portion of the SiO_2 crucible, rendering it useless.

As a result of using the fused SiO_2 crucible, a rather unusual, unexpected phenomena was observed. The white, porous, crucible which was put into the furnace at the start of the experiment was removed as a gray, dense crucible of the same shape and size as the original. In order to determine what had caused this change, and more importantly what had happened to the crucible, an attempt was made to break off a piece of the gray matter for analysis. Surprisingly, the crucible was quite resistant to fracture, unlike the original fused SiO_2 material. With the aid of a hammer and chisel, the crucible was finally broken, and analyzed. The results of these analyses became the driving force for a patent application [Appendix A] on a new IPC process and material system known as Co-Continuous Ceramic Composite or C^4 materials. This *"event"* was also the impetus for the work detailed in this thesis.

C^4 materials are unusual materials from several aspects. Aside from the characteristic co-continuous microstructure and useful properties [Appendix B], the materials are produced by a truly arbitrary near-net shape process. From the point of view of thermodynamics, Equation 1 dictates the displacement reaction upon which the process is based. The SiO_2, however, is not merely a chemical reactant, but a geometric precursor as well. Following transformation, the newly formed composite body has the same size, shape, and surface contour as the starting SiO_2 preform. Thus, the ability to produce composite bodies is limited only by existing ceramic powder and glass forming technologies.

The SiO_2 preform is introduced into the melt merely by immersing the ceramic body in the molten alloy. The time necessary for completion of the reaction is dependent on several variables, most importantly, the temperature of the Al bath and thickness of the part. Once removed, the body is air cooled and subjected to either a mechanical or chemical cleaning process to remove extraneous metal from the surface. The resulting component is virtually identical in geometry to the starting SiO_2 component on a macroscopic or geometric scale. Microstructurally, however, the component is no longer SiO_2, but a three dimensional, co-continuous Al_2O_3/Al composite.

With any new material/process comes the need to understand the fundamentals of its character. In the past four years much work has been done in understanding the mechanical and physical behavior of C^4. Included in this effort has been a concerted attempt to phenomenologically understand how and why this material forms. By observing the kinetics associated with Equation 1, and examining the resulting microstructures and product phases it was anticipated that some insight into the C^4 reaction could be gained. This thesis represents an attempt at providing some understanding of this phenomena.

CHAPTER II

LITERATURE REVIEW

1. Overview

The following section represents a review of pertinent literature associated with the development of the C^4 materials. For simplicity, the reviewed documents have been divided into four sections: (2.1) interpenetrating phase composite (IPC) structures, (2.2) displacement reactions, (2.3) reactions between silica and aluminum, and (2.4) oxidation of metals. While these distinctions may appear unrelated to each other, this simple classification represents a logical division in the background information necessary for understanding the behavior of this novel material.

2. Interpenetrating Phase Composite (IPC) Structures

The nature of materials characterized by interpenetrating phases has long been acknowledged. In the classic work by D'Arcy Thompson [3] their existence in naturally occurring systems (i.e. wood, bone, etc.) is qualitatively examined. The topic, however, seems to have been virtually ignored until recent times. In 1989 the Department of Energy Basic Energy Sciences (DOE-BES) division, in response to a growing interest in the topic, sponsored a workshop on multiphase or co-continuous composite materials. Clarke [4]

reviewed the information presented at the conference in lieu of a more formal proceedings. While topics such as mechanical properties and microstructural characterization were presented, emphasis was placed on processing methods since few techniques actually exist for forming these elusive materials. Although the thrust of the workshop was on ceramic materials, much of the subject matter can be applied equally well to metals, polymers and combinations of all three.

Many techniques for producing IPC materials are reviewed in Clarke's report. These methods can be loosely classified into a few general categories. This number can be reduced even further to three specific categories if only methods relevant to this thesis are considered: (1) infiltration techniques, (2) *in-situ* decomposition/precipitation techniques and (3) reactive metal processes. Much literature exists detailing specific examples of each of the above synthesis methods. Little of the new literature, however, is considered revolutionary or unique. Thus the various techniques can be adequately reviewed by examining several specific examples.

2.1 Infiltration Techniques

Infiltration processing of IPC structures can be defined by the assisted infiltration of a fluid into an interconnected, open pore solid preform. In the most basic from, a molten metal is percolated into a porous ceramic preform. The actual infiltration must be induced either by physical or chemical methods. Toy and Scott [5] employed a vacuum to aid in the infiltration of liquid Al into porous AlN preforms. In producing these materials two

critical observations were made. First, Arrhenius plots of infiltration rates yield an unexpectedly high activation energy ranging from 330 to 460 kJ/mol. Values this high suggest that a chemical reaction rather than viscous flow is rate limiting in this process. Second, the investigators found a direct relationship between pore size in the preform and infiltration rate. The smaller the pore size, the slower the rate of infiltration.

Subsidiaries of the Honda Motor Company have put into production a process similar to that used by Toy and Scott. As a means of reducing automobile gross curb weight, traditional cast iron cylinder bore liners have been replaced with an $Al_2O_3/C/Al$ composite material [6,7]. The composite is produced through a complex, multi-step process which is reported to be economically feasible.

As a means of producing the near-net shape composite, low aspect ratio Al_2O_3 and C fibers (i.e. whiskers) are mixed with a binder in a dissemination/distribution apparatus. This mixture is introduced into an aspiration filter mechanism much like that used for paper production. The fiber mixture is drawn onto a porous, disposable filter composed of resin bonded sand. The purpose of the filter is two-fold: it provides a means of transport for the fiber-slurry and it acts much like a traditional casting "core".

After the filter is adequately coated with the fiber mixture, it is removed from the processing tank and placed into a water actuated rubber press. Once situated into the press, pressure is applied to the rubber

membranes which in turn compress the fiber agglomerate, partially densifying the preform. The rubber press technique is employed such that only light, even pressure is applied to the preform, thus only nominal densification (and no breakage of the fibers) occurs.

Following pressing, the preform/filter assembly is dried and heated to a temperature ranging from 400°C to 600°C promoting the decomposition of the resin-bonded filter, leaving behind an interconnected fiber preform capable of receiving molten metal. Infiltration is accomplished through low-speed, low pressure die casting. The final product can then be machined and pressed into the engine block.

Unlike many other IPC materials, Honda's engineers have employed common, commercially available material constituents for use in the composite bore liners. Rather than design an application around a given material/process, Honda appears to have designed the material and process around their application. In spite of the complexity associated with the process, the Honda composite bore represents one of the most successful commercial uses of composite materials.

An alternative approach to pressure assisted infiltration is the PRIMEX™ process developed by the Lanxide Corporation. Through alloying or doping additions made to an Al melt, coupled with a controlled atmosphere, a near net-shape preform can be "spontaneously" infiltrated. Porous preforms, produced by a variety of traditional ceramic processing

techniques, and composed of several different materials including diamond [8], SiC [9], and Al_2O_3 [10] have been successfully used in this process. In all three cases, the infiltration methods are virtually the same. As described by Aghajanian *et* al.[10], an Al-Mg alloy is placed in contact with and directly above a partially sintered, porous preform. The assembly is placed in a furnace which is evacuated and back-filled with N_2 gas. Upon heating to an appropriate temperature, the metal melts and infiltrates the preform yielding a continuously reinforced ceramic/Al composite.

Experimental evidence suggests that the PRIMEX™ process has a strong dependence on processing variables including Alloy composition, N_2 content, infiltration temperature, and preform grain size. At concentrations below 1% Mg (weight percent) infiltration would not proceed. As the Mg content was increased, the rate of infiltration increased proportionally. It is suggested that this phenomena is due to the Mg's ability to reduce the surface tension of the molten alloy. Furthermore, the addition of Si reduces the viscosity of the Al-Mg alloy increasing the infiltration rate even further. The addition of Cu, which is known to increase the viscosity of molten Al alloys, reduces the infiltration rate.

The critical N_2 concentration is approximately 25%, below which infiltration will not proceed. Above this value, infiltration appears to proceed to completion providing the other variables are favorable. No explanation for this phenomena is presented.

The effect of infiltration temperature on penetration depth was observed to be directly proportional and linear. This suggests some form of thermal activation associated with the process, however no explanation is given by the authors.

Finally, experimental observation indicates that infiltration into fine particles occurs more readily than larger particles. This is the opposite of the findings presented by Toy and Scott. As an explanation, Aghajanian *et al.* suggest that this behavior is due to the chemical nature of the process. Since the process is conducive to metal/ceramic wetting conditions, the increased surface area associated with smaller particles provides a more wettable surface and hence a more rapid infiltration.

Another technique, known as reactive infiltration, can be exemplified by the work of Behrendt *et al.* Composites of Si/SiC or $MoSi_2$/Si/SiC are produced by infiltrating molten porous carbon preforms with molten Si or Si-3.2 Mo (atomic percent), respectively. During infiltration, the molten phase reacts with the preform producing a ceramic material (SiC in the former), or ceramic and intermetallic phases ($MoSi_2$ and SiC in the latter). Evidence suggests that the initial pore fraction in the preform is critical in allowing full reaction between the reactants. Since the reaction rate is relatively faster than the infiltration rate, precursors with a pore fraction below a critical value will become "choked off" during processing. Thus, production of controlled porosity preforms in this technique as well as in the previous examples is critical.

2.2 *In-situ* Decomposition/Precipitation Techniques

Composite structures produced via decomposition of a solid solution or precipitation of a second phase within a homogenous matrix are one of the more simple, yet most limited composite systems. In order for this technique to be effectively used, a solid solution containing the desired elements must be formed. Upon a specific heat treatment (dictated by the given system) the solution decomposes (i.e. spinodal decomposition) or precipitates a second phase. Examples of such systems include Vycor™ glass [4] which spinodally decomposes into a silica glass network interpenetrated by a borosilicate glass network, and the Nb-Si system [11] which yields a Nb/Nb_5Si_3 metal/intermetallic structure upon precipitation. While IPC structures are simple to produce using this technique, systems for which it is feasible are limited to those with mutually soluble constituents at high temperatures. Furthermore, the literature suggests that this technique is limited to composites with similar phases (e.g. glass/glass, metal/metal, metal/intermetallic, or ceramic/ceramic). Thus the decomposition/precipitation method appears to be useless (at least for the present time) for forming metal/ceramic composite structures.

2.3 Reactive Metal Processes

Reactive metal processing used as a technique for producing composite structures has received much attention over the last decade due largely to the Lanxide Corporation's directed metal oxidation or DIMOX™ process (to avoid legal entanglement this process is often referred to as the

non-trademarked DMO process). The term oxidation is used here in its broadest sense, meaning metals which give up or share electrons with another element to form a compound. Thus, in this context, nitridation (i.e. the forming of a nitride) is considered an oxidation process. In one of the earlier papers on this process, DMO is defined as

"...the oxidation of a bulk molten metal by a gas to produce a solid ceramic body via a directed growth process that results from unusual oxidation behavior."[12]

In less vague terms, the process entails the oxidation of molten metal in such a way so that the product oxide is porous. As the reaction continues, molten metal wicks (i.e. transport through capillary action) through the pores providing a fresh molten surface to oxidize. The reaction continues yielding a ceramic oxide structure infiltrated by continuous metal channels. This technique has been shown to work for several systems including Al/Al_2O_3, Al/AlN, Ti/TiN, and Zr/ZrN, however the first of these has received the most scientific and industrial attention.

A significant requirement of DMO is the need for "dopants" (i.e. less than approximately 10 weight percent) to be added to the Al melt. In the case of the Al/Al_2O_3 system both Mg and a group IVB element (typically Si) are necessary to promote the reaction. Nagleberg [13] showed that the absence of

Mg will completely prevent the composite structure from forming, while the absence of Si merely retards composite growth, yielding a non-homogeneous, "pock-marked" composite structure.

The accepted reaction mechanism as proposed by Vlach *et al.* [14] features three stages: the initial oxidation, incubation, and composite growth. The initial oxidation event is characterized by the formation of a discontinuous $MgAl_2O_4$ spinel at the melt surface. This is followed by the incubation period, during which MgO evolves from the spinel and forms at the gas/oxide interface. Liquid Al then permeates the spinel through the existing microchannels and oxidizes, forming Al_2O_3 nodules. These nodules proceed to coarsen, eventually impinging upon one another and forming a near-planar growth front. This is defined as the composite growth regime.

Kinetic evaluation of the DMO behavior has become a strong subject of debate. A review of the literature indicates that there are virtually as many different reported growth rates and activation energies as there are research teams evaluating the process. Growth rates have been reported ranging from approximately 7 $\mu g/cm^2/s$ [14] to greater than 50 $\mu g/cm^2/s$ [15] while activation energies have ranged from approximately 400 kJ/mol [16] to approximately 90 kJ/mol. Some of these discrepancies can be related to subtle alloying variations (such as activation energy), however growth rate variations still remain a mystery. Clearly more work needs to be done on this subject.

Finally, it should be mentioned that DMO materials rarely see application in their as-reacted from. Instead, the material described above is grown into a bed of inert filler material (e.g. fibers, whiskers, platelets) composed of SiC, Al_2O_3 or some other non-reactive material. This provides a means of increasing the mechanical properties of the material as compared to the un-reinforced DMO material. As a result, however, further variables and processing steps are introduced to this technique, decreasing the simplicity and increasing the cost of producing this material.

3. Displacement Reactions

Rapp *et al.* [17] and Yurek *et al.* [18], in two intimately related papers, thermodynamically and kinetically rationalize the microstructures which evolve when solid metal/metal oxide couples are annealed. In the first of these two papers the authors claim that metal/metal oxide couples, when allowed to interdiffuse, react according to:

$$\upsilon Me + M_xO \rightarrow Me_\upsilon O + xM \qquad (2)$$

where Me and M are metals and $Me_\upsilon O$ and M_xO are there respective lowest oxides. Mutual solubility is assumed negligible for Me and M_xO, M and $Me_\upsilon O$, M_xO and $Me_\upsilon O$, and Me and M. Furthermore, no ternary or other binary compounds form other than those shown in Equation 2. Under these conditions two possible microstructures can result: aggregate or layered. The aggregate arrangement is a co-continuous structure which forms between the M and $Me_\upsilon O$ constituents. The theory presented in this paper relates

thermodynamic and kinetic arguments to the resulting phase morphology. If a *wavy* (i.e. non-flat) interface is assumed between the reactants, the evolution of the microstructure becomes dependent on the rate-limiting step [19] of the reaction. If cation diffusion through $Me_\upsilon O$ is rate-limiting, the interface will straighten out and the layered morphology will form. Alternatively, if diffusion prior to the $Me_\upsilon O/M$ interface is rate-limiting (e.g. a slow reaction at the $M/M_x O$ interface), growth conditions will be such that the $Me_\upsilon O/M$ interface grows unevenly, resulting in the co-continuous morphology.

Yurek *et al.* verified and extended Rapp's work by looking at the $Fe/Cu_2 O$ system. This system is known to produce the aggregate/co-continuous microstructure. According to the Rapp *et al.* model, the growth rate should depend on the oxygen activity at the growth front as well as the volume fraction of oxide in the product zone. Numerical analysis produced a solution to this model which agreed with experimental observation.

A practical example of displacement reaction synthesis of composite materials is the Lanxide Corporation's $Zr/ZrB_2/ZrC$ materials produced by the directed reaction of Zr with $B_4 C$. As detailed by Johnson *et al.* [20,21] and Claar *et al.* [22], liquid Zr will react with $B_4 C$ according to the reaction:

$$(2.2 + x)\, Zr + 0.6\, B_4 C \rightarrow 1.2\, ZrB_2 + ZrC_{0.6} + x\, Zr \qquad (3)$$
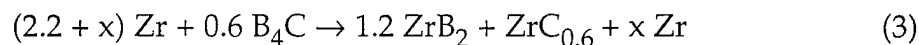
The resulting microstructure features continuous ZrB_2 platelets in an interconnected ZrC matrix with either isolated or connected regions of residual Zr metal. The amount of residual metal (and subsequently the degree of interconnectivity) can be varied by controlling the quantity of reactant Zr. Thus if x in Equation 3 is equal to zero, a $ZrB_2/ZrC_{0.6}$ composite will be formed with virtually no residual Zr. If excess Zr is used (e.g. x approximately equal to 0.66) then a composite will be formed with approximately 22 volume percent interconnected metal. Thus a useful degree of microstructural tailorability is featured in this system.

Kinetic studies of Equation 3 suggest a parabolic relationship between growth and time. This is consistent with a mass-transfer step (i.e. diffusion) limiting the overall reaction. Johnson *et al.* [21] suggest that either the capillary flow of Zr through the matrix or the diffusion of Zr through an intermediate boride/carbide two phase layer constitutes the rate limiting step. Unfortunately, experimental evidence was not able to confirm which of these steps actually limits the rate.

4. Reactions Between Silica and Aluminum

The reaction between Al and SiO_2 has historically been viewed as a "pesting" reaction in the aluminum processing industry. The interaction results in the degradation of the refractory material, as well as a Si enrichment of the molten Al/alloy. Brondyke [23] was one of the first to attempt to study and classify this reaction by looking at the effect of molten Al on commercially produced Al_2O_3-SiO_2 refractories. The governing

reaction associated with this phenomena is the same as Equation 1, however, here the reaction product is "a hard, dense, monolithic" material penetrating into the refractory brick. Accompanying the reaction is an increase in volume of the penetrated product compared to that of the reactant resulting in cracking and spaling of the refractory material. Through simple cup tests and immersion tests, Brondyke measured penetration depths of the reaction front as well as Si pick-up in the molten Al. Results of the work suggest that the penetration depth of the reaction product appears to be unrelated to the initial silica content of the refractory, however, the amount of Si picked-up by the melt is.

This apparent dichotomy can be explained by noting the formulations used in preparing the refractories. Diaspore clay is often used as a binder in high-alumina (>50% Al_2O_3) refractory brick. Thus, penetration occurs through the clay binding material surrounding the alumina grains. The result is an apparently deep penetration with little Si rejected into the melt. Furthermore, 99% Al_2O_3 brick prepared with an inorganic silica binder experienced deep penetration as well as high Si pick-up in the melt.

As a follow-up to the previous work, Lindsay et al. [24] examined the reaction between Al-Mg alloys and various refractory brick compositions. Rather than studying the attack of the Al on the refractory material, methods of preventing attack were investigated. The general reaction:

$$2Al + 3\,MO = Al_2O_3 + 3\,M \qquad (4)$$
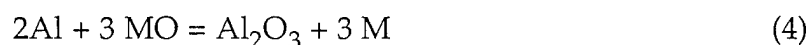
was used to describe the reaction of an Al alloy with an arbitrary oxide refractory (i.e. MO). The forward reaction represents attack on the oxide ceramic, while the backwards reaction represents the attack of a metal component of the alloy on the Al_2O_3 in the refractory.

For the purpose of the experiment it was assumed that the alloy is composed of Al and Mg, and that a suitable resistive refractory composition could be determined. The following reactions and standard free energies are applicable:

$$MgO + Al_2O_3 = MgAl_2O_4 \qquad \Delta G°_{1000} = -8 \text{ kcal} \qquad (5)$$

$$3Mg + Al_2O_3 = 3MgO + 2Al \qquad \Delta G°_{1000} = -28 \text{ kcal} \qquad (6)$$

$$3Mg + 4Al_2O_3 = 3MgAl_2O_4 + 2Al \qquad \Delta G°_{1000} = -52 \text{ kcal} \qquad (7)$$

$$3Mg + MgAl_2O_4 = 4MgO + 2Al \qquad \Delta G°_{1000} = -20 \text{ kcal} \qquad (8)$$
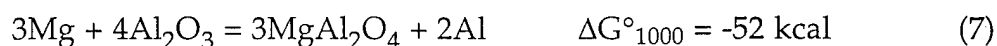
The negative free energy associated with all four reactions implies that the products (i.e. left sides) are stable. Thus according to Equation 5, the $MgAl_2O_4$ spinel is favored over the MgO and Al_2O_3 reactants. Furthermore, while the displacement reaction in Equation 6 is feasible, the spinel formation in Equation 7 is preferred (smaller $\Delta G°_{1000}$ value). Equation 8 shows that the reaction of Mg with the spinel is also possible, however the reaction between Mg and Al_2O_3 (Equation 7) is favored.

The hypothesis drawn from the above thermodynamic comparison is that the stability of the spinel can be used to prevent reaction between the Al-

Mg alloy and the refractory if the spinel is used within the refractory. This theory was tested by immersing refractory bricks of high Al_2O_3, high MgO (periclase) and high $MgAl_2O_4$ content into Al and Al-Mg alloys. Results indicated that neither the periclase nor the spinel bricks were attacked by the Al-Mg alloy and none were attacked by the commercial Al alloy. Thus it is possible to contain molten Al without refractory degradation.

Lindsay *et al.* present a parenthetical note in their paper concerning one of the test pieces which did react. Apparently, one of the high Al_2O_3 bricks contained mullite ($3Al_2O_3 \cdot 2SiO_2$), possibly as a binder component, which showed signs of severe attack following exposure to Al. The resulting product material contained Si and secondary Al_2O_3, similar to the reaction product described by Brondyke. This observation suggests that not only SiO_2, but SiO_2-containing compounds such as mullite will react with Al. This implication is further supported by Loehman *et al.* [25], however formal report detailing their work has not been published.

As stated previously, Equation 1 is usually considered to be a deleterious reaction, causing much trouble in the Al processing industry. As an alternative to this viewpoint, George [26] patented a process employing this reaction as a method of producing "...articles having metallic aspect, a highly refractory nature, a very hard substance, and good electrical conductivity..." The process entails reacting a silica structure with molten Al between 700°C and 900°C for a time long enough to complete the reaction.

Standage and Gani [27] examined the process patented by George, however their impetus was the prevention of Equation 1 during the coating of fused silica fibers with Al. Their procedure involved measuring the rate of penetration of the reaction product when fused silica rods were immersed in molten Al. The rods were preheated to melt temperature prior to immersion in all cases. Measurements were made by photographing the samples with a projection microscope and measuring with a graduated rule.

The results of their experiments indicate a linear relationship between penetration depth and time with an activation energy of approximately 44 kJ/mol. The reaction, however, did not start immediately, but exhibited a brief incubation period (the duration of which decreased with increasing reaction temperature). The reaction products consisted of Si, η-alumina, θ-alumina and α-alumina. These reports are somewhat consistent with those of George with two exceptions. George claims an Al-Si alloy along with the alumina phase, while the current work claims only Si. George also claims a generic "alumina" as opposed to the current authors' three phase distribution. The first of these discrepancies cannot be explained, while the second of these is possibly due to improved analytical techniques. It is well known [28] that η-alumina will transform to the transient θ-alumina phase followed by a transformation to α-alumina, however detecting these different phases may be difficult. Thus George's "alumina" may be an undetected/unreported mixture of alumina phases, or it simply may have undergone full transformation to the α-phase.

Prabriputaloong and Piggott [29], using thin film techniques, attempted to identify any compounds which form at the Al-SiO$_2$ interface prior to and during reaction. There results were unsuccessful in determining compounds at the interface, however, a more interesting observation was the absence of an incubation period. This was assumed to be a result of the reaction taking place in a vacuum environment.

As a means of confirming their assumptions, Prabriputaloong and Piggott [30] repeated the experiments of Standage and Gani both under vacuum and in laboratory air. The results showed similar linear behavior to that reported by Standage and Gani, however a decrease in incubation period was observed in the experiments performed under vacuum.

The authors surmised that the incubation period was due to the presence of an Al$_2$O$_3$ layer which formed on the surface of the melt. When under vacuum, however, the Al$_2$O$_3$ layer volatilizes as Al$_2$O. This results in the thinning or complete elimination of the barrier layer and the subsequent incubation period.

In a similar study to the above work, Thacker [31] examined the reaction between fused SiO$_2$ thin walled tubes and molten Al-Si alloys (Al-12.5 Si and Al-30 Si; both in weight percent) at 750°C, 830°C and 1050°C. The results indicate, once again, a linear relationship between reaction layer thickness and time with an incubation period lasting for several minutes in all cases.

Thacker reports higher reaction rates for the Al-12.5 Si eutectic alloy compared to the Al-30 Si alloy at all three temperatures. It is also reported that the maximum slope (i.e. rate) occurs for the 830°C reaction conditions for both alloys. Reported activation energies for the reactions were approximately 12.6 kJ/mol for the eutectic alloy and approximately 23.4 kJ/mol for the hypereutectic alloy. Admittedly, the accuracy of these measurements is questionable due to relatively few data points (i.e. 2 per linear segment in each plot) as well as the high degree of error in measurement. The values, however, are similar in magnitude to the reported diffusion of Si in molten Al (approximately 20 kJ/mol). This is the first indication of a rate limiting step within the literature.

If diffusion of Si (or some other species) is the rate limiting step, the expected penetration depth plots should be parabolic rather than the reported linear. The presence of the linear plots suggest a rate limiting step associated with a reaction or nucleation phenomena. If this is were indeed true, the observed activation energy would be merely an observation and would not correlate with the published diffusion data. Thus, the reliability of the rate data reported by Thacker is, at best, questionable.

The reaction products reported by Thacker were "...large, columnar grains of gray material growing radially..." inward, which remain attached to the SiO_2. The grains were quite fragile, and often cracked upon cooling. This description appears consistent with the previous literature, however no analysis of the reaction product was made.

Thacker also reported a lack of reaction between Al and crystalline silica. This appears to contradict previous literature [26]. No reaction occurred between lower softening point eutectic glasses (SiO_2-CaO eutectic and SiO_2-CaO-Na_2O ternary eutectic) either. Furthermore, it was shown that molten SiO_2 ($T \approx 1610°C$) will readily react with Al, resulting in a complete reduction of the SiO_2 to pure Si with no other product phase present (other than a thick dross scale on the surface of the melt).

5. Oxidation of Metals

The subject of oxidation of metals is indeed a broad field providing subject material for countless text books and journals. There is, however, a specific sub-topic which is significant to this thesis. Originally identified in their classic discourse, Pilling and Bedworth [32] describe a method by which metals can be divided into one of three classifications based on the nature of their respective oxidation products. Oxides are assumed to have a high vapor pressure, in which case they evaporate as soon as they are produced (e.g. Mo), or a low vapor pressure, in which case they from a solid structure (e.g. Fe). The second type (i.e. solid type) can be divided even further into two categories: oxides which form a continuous, protective scale, and those which produce a discontinuous, cellular scale. It has been suggested that the classification of these solid oxides can be determined by the following ratio:

$$\frac{Wd}{wD} \qquad (9)$$

in which: W = molecular weight of oxide

                   d = density of metal

                   w = formula weight of metal

                   D = density of metal

Equation 9, commonly referred to as a Pilling-Bedworth Ratio or PBR, can be re-written as the ratio of the specific volume of the oxide to the specific volume of the metal on a per mole of metal basis. Specific volume is defined as the volume of one mole of the given species. The "per mole basis" is derived from the *formula weigtht* term (w), which is defined as the molar weight multiplied by the respective stoichiometric coefficient.

In simple terms, if the product oxide occupies less physical space than the parent metal, the ratio is less than unity and the cellular or discontinuous oxide type is produced. If, however, the oxide occupies more space than the parent metal the PBR will be greater than 1 and the compact or continuous scale forms.

The group of metals which exhibit the cellular oxides is comprised mostly of the *alkali metals*, (e.g. Ba, Ca, K, etc.) while those exhibiting the continuous oxide scale comprise mostly the *heavy metals* (e.g. Cd, Pb, Ni). In the case where PBR<1, the oxide scale is porous and/or cracked, allowing oxygen access to bare metal, thus the rate of oxidation is constant for a fixed temperature. For the case of PBR≈1, the oxide is protective, providing a barrier between the metal surface and the oxygen source. It has been shown

that oxygen will diffuse through this barrier, thus the rate of oxidation of these metals exhibits a parabolic relationship with time.

The discontinuous oxidation scale (PBR<1) has been expanded by Kubaschewski and Hopkins [33] in their rather extensive review of oxidation. The discontinuity of the oxide scale is caused by stresses which develop due to the lattice mismatch between the parent metal and product oxide. These stresses eventually lead to mechanical breakdown in the oxide film. It is suggested that the breakdown can assume two possible forms: blistering or shear-cracking. The former occurs when adhesion is weak and cohesion (between the metal and the oxide) is strong, while the latter occurs when cohesion is weak and adhesion is strong. Regardless of the breakdown type, the process is accompanied by linear oxidation.

Oxidation behavior supporting this model has been reported in a variety of metallic systems. Leontis and Rhines [34] observed the oxidation of nearly 400 samples of Mg and Mg-alloys in various O_2 containing gaseous environments. In virtually all cases, at sufficiently high temperatures, oxidation behaved linearly with time although in some cases, a brief induction period was observed. The reported activation energy at steady state was approximately 211 kJ/mol.

Observation of the scale indicated that the reaction product grew outward from the surface, leaving the corners free of oxide. This is indicative of the reaction taking place at the metal/oxide interface. Interestingly, surface

markings present upon the original metal surface were retained in the outer surface of the oxide.

The observed induction period indicates that parabolic oxidation does occur in the initial oxidation of Mg. Leontis and Rhines attribute this to a thin coherent MgO film which develops under plane stress conditions, and can thus resist the tensile stress which arise due to the misfit of the oxide and parent metal. When this layer reaches a critical thickness, which depends on temperature, surface contour of the metal, and composition of the film, spontaneous rupturing occurs, and linear, non-protective oxidation occurs. This work was repeated by Gregg and Jeepson [35] resulting in similar results.

Gulbranson and Wysong [36] observed the oxidation of Al; a material which usually obeys parabolic oxidation behavior. Evidence indicates that between 475°C and 500°C the behavior changes from parabolic/protective to linear/nonprotective. At approximately 550°C, the behavior is purely linear. This phenomena is not attributed to rupturing of the film as is the case in Mg, but to inhibited formation of ions necessary for protective oxide formation. It is suggested that this would lead to linear behavior, however neither the result nor the implied cause is supported.

Cubicciotti [37] examined the oxidation of U and found similar behavior to Mg and Al. At low temperatures, parabolic/protective behavior was observed. However at higher temperatures (T > 190°C), linear behavior was observed. It was suggested that this behavior could possibly be due to a

continuous increase in the sample temperature as oxidation occurred. This phenomena could possibly cause parabolic behavior to appear linear. This theory was tested by examining the heat input due to oxidation and the heat output due to radiation for several pure-parabolic materials (Cu, Fe, Mn) and several metals which undergo parabolic to linear behavioral transitions (Th, Al, and U). It was found that the latter set was less likely to increase in temperature than the former set, thus it is unlikely that the suggested exothermic character is present.

Cubicciotti suggests a re-interpretation of the Pilling-Bedworth argument as a justification for the observed behavior. Since the volume of the oxide is substantially larger than that of the metal, a *compressive* stress develops in the oxide. When the stress becomes too large, buckling and rupturing occur resulting in the observed linear behavior. With increasing temperature, the thickness at which the oxide ruptures occurs sooner. At a high enough temperature, cracking occurs so soon that the entire oxidation behavior appears linear.

Cathcart *et al.* [38] performed a microtopographical study of oxide films on Nb. Behavior similar to that exhibited by the preceeding metals was observed. Oxidation, for a given temperature (325°C < T < 600°C) initially behaved parabolically, followed by a transition period leading to linear/non-protective behavior. Similar to the oxidation of U, as the experimental temperature increased, the parabolic and transition periods decreased,

yielding a greater degree of linear behavior. At temperatures greater than 600°C, pure linear behavior was observed.

TEM examination of carbon replicas of the oxidation surface indicate a relationship between surface morphology and oxidation behavior. During the initial parabolic/protective regime, the oxide appears continuous and smooth, thus indicating a barrier to further oxidation. During the transition regime, blisters in the surface begin to appear, and finally during the linear behavior, a heavily blistered, discontinuous surface is observed.

Similar to U, Nb has a high PBR (i.e. 2.7), implying that a protective, continuous scale should form. This is indeed observed in the early stages of oxidation. The authors suggest a modification to the PBR argument similar to that presented by Cubicciotti. Initially, a protective scale forms at the metal/oxide interface. As the scale coarsens, compressive stresses develop due to misfit between the metal and the oxide. This is supported by the observed ridges, indicative of plastic buckling in the scale. This buckling eventually leads to blistering and rupturing, rendering the scale non-protective. This process can continue providing that new oxide forms at the metal/oxide interface rather than at the oxide/gas interface.

A review of the oxidation of Nb, as well as Ta, Mo and W was performed by Kubaschewski and Hopkins [39] indicating that these metals also oxidize linearly at high temperatures (T≈600°C and higher). Their mechanism to explain this behavior is similar to that proposed for U.

CHAPTER III

EXPERIMENTAL PROCEDURE

As a means of gaining insight into the mechanism by which C[4] materials form, an attempt was made at studying the kinetic behavior of Equation 1 at various temperatures. High purity, semiconductor grade, fused SiO_2 glass rods of 10mm diameter (data set B) and 16mm diameter (data set A, collected by A.L. Marasco) (GE 214LD, General Electric Company or equivalent) were reacted with molten, commercial purity Al (CP 1100, Alcoa or similar). The melt was maintained in a fused SiO_2 crucible coated with a non-reactive ceramic coating. Bath temperature was maintained in a custom built box furnace/controller assembly. Temperature was controlled to within ± 3°C using a type K thermocouple. Samples were reacted for fixed times over the temperature range of 700°C to 1400°C.

Following reaction, samples were removed from the bath, air cooled, sectioned with a high-speed diamond cut-off wheel, mounted, ground, and diamond polished according to standard metallographic techniques. Some of the lower temperature reaction products were quite fragile and difficult to handle. These samples were encased in a thermo-set polymer shrink tube (Thermo-Shrink®, Ideal Industries, Inc.) prior to cutting.

31

Cross sectional penetration/reaction depths were measured by one of two methods. Samples were either measured directly with the aid of a microscope fitted with a graduated eyepiece (data set A), or macro photographs of the samples were measured with a ruler (data set B,). Values of all measurements were recorded along with the respective processing times and temperature conditions. Average measurement values are presented in Appendix C.

The two data sets (A and B) show comparable kinetic behavior, however due to improved stability in the "A" furnace during processing, less scatter in the observed penetration values was noticed. Thus, for kinetic measurements data set A was used.

Further information was obtained by examining the polished samples described above using scanning electron and optical microscopy (SEM and OM respectively) techniques. Phase identification in reacted samples was performed using powder X-ray diffraction techniques. Samples were pulverized using a porcelain mortar and pestle.

CHAPTER IV

RESULTS

In order to observe general trends over the entire temperature range (700°C $\leq$ T $\leq$ 1400°C), an isochronal plot of reaction rate data for a 4 hour hold time was constructed. The resulting plot, shown in Figure 1, indicates that the reacted thickness is dependent on temperature. Figure 2 is a similar plot focusing on temperatures between 700°C and 1150°C. Three distinct regions are apparent in this plot. These regions are denoted as a low temperature regime ($T_{m,Al} \leq T \leq 800°C$), an intermediate regime (800 $\leq$ T $\leq$ 950°C), and a high temperature regime (T $\geq$ 950°C). The temperatures which define the limits are approximate (i.e. $\pm$25%) due to the resolution of the experiment, the accuracy of the equipment used in measurement, and perhaps, the intrinsic nature of the material itself.

Figure 3 shows a typical sample set for material produced in the low temperature processing regime together with the corresponding microstructure. Observation indicates that the thickness of the reaction product is proportional to the reaction time. The reaction product shown in Figure 3a is quite fragile as evidenced by the presence of a relatively large number of cracks. X-ray diffraction experiments made on this material (Figure 4) indicates that it is composed of Al and θ-Al_2O_3; the latter being a
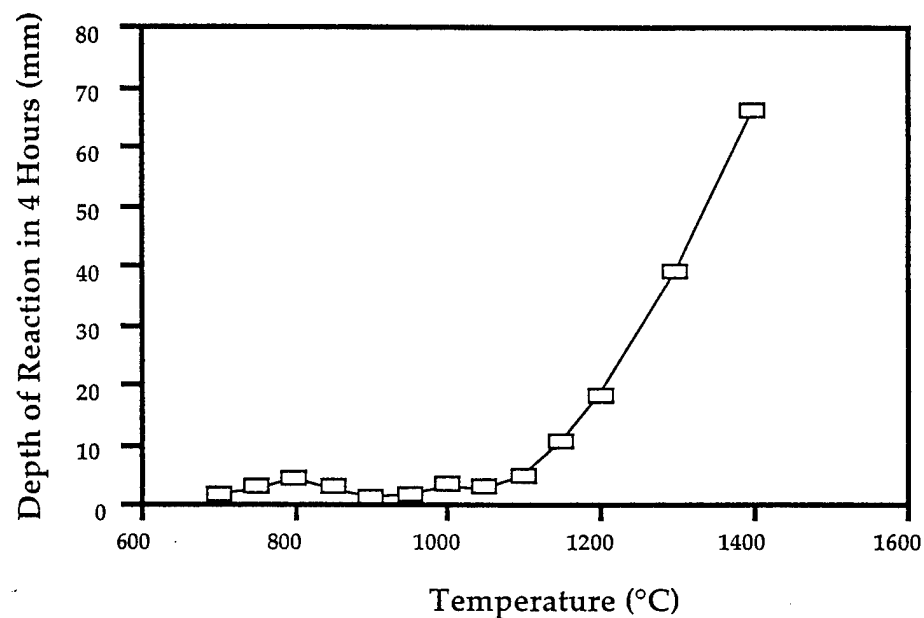
Figure 1.   Variation of transformation rate with transformation temperature. Samples were transformed at their respective temperatures for 4 hours.
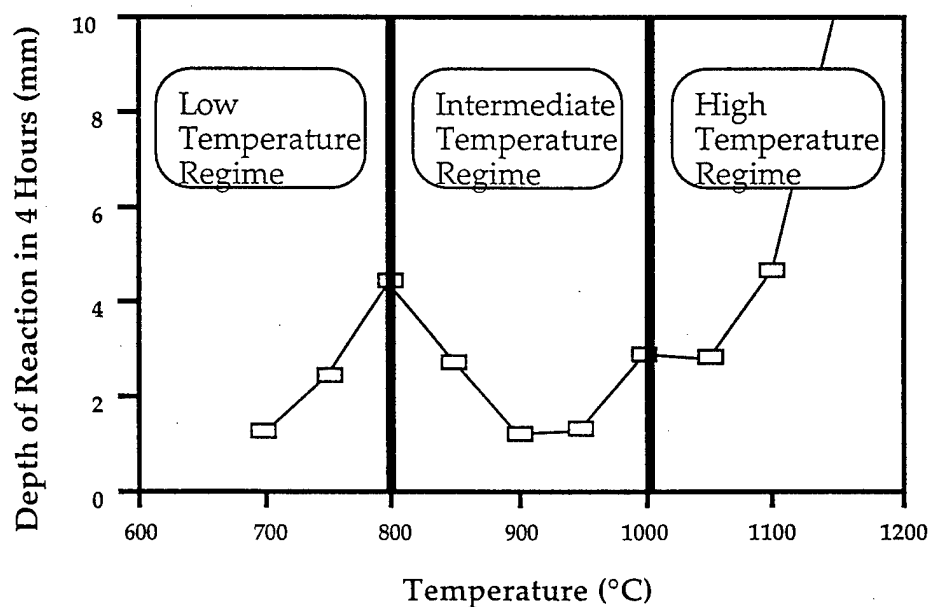
Figure 2.   Variation of transformation rate with transformation temperature for temperatures between 700°C and 1150°C.

(a)   (b)
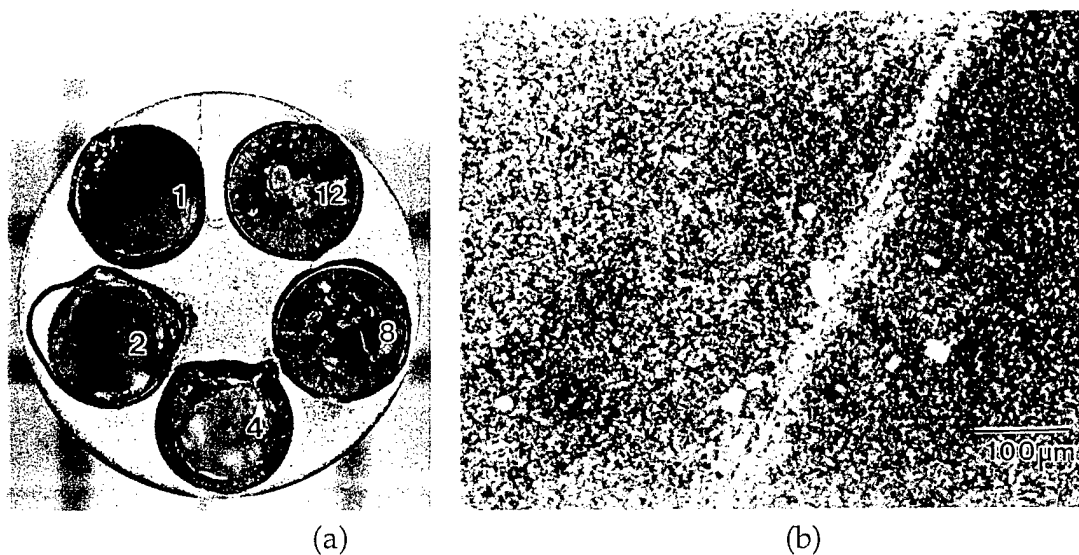
Figure 3.   Typical sample set (a) composed of five 10mm specimens produced in the low temperature regime. Numbers represent reaction time. (b) is the corresponding optical micrograph.
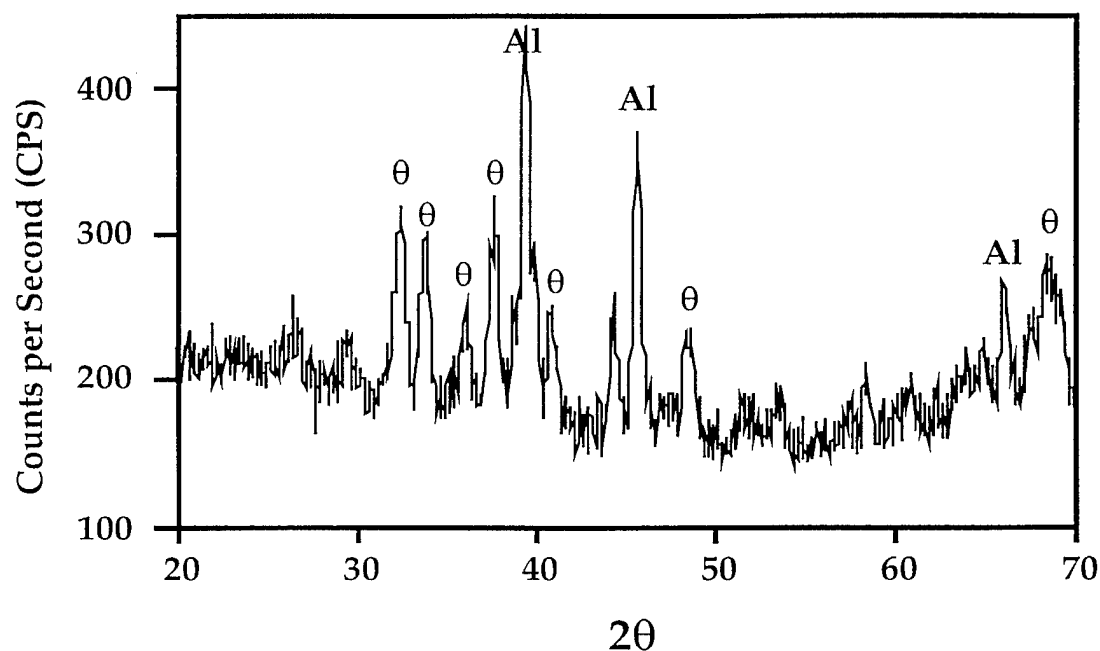
Figure 4.   Typical X-ray diffraction data for low temperature regime reaction product. θ-Al_2O_3 and Al are present.

fine grained, transient phase of Al_2O_3 [40]. The accompanying optical micrograph (Figure 3b) is consistent with an extremely fine grained material.

Material produced in the intermediate temperature regime is shown in Figure 5. An inspection of the sample set (Figure 5a) shows that the reaction thickness is changes very slowly with respect to time; thus thicknesses for all five samples within the set are approximately the same in magnitude. Behavior such as this suggests that the resulting reaction initially progresses quickly followed by "passivation" (i.e. the rate of reaction slows down and/or stops). The corresponding microstructure (Figure 5b) shows a duplex structure which was confirmed by X-ray diffraction (Figure 6) to consist of the previously observed θ-Al_2O_3/Al structure surrounding colonies of α-Al_2O_3/Al. While the growth of α-Al_2O_3 from θ-Al_2O_3 is common [28], the passivating behavior and its relation to the duplex morphology is not fully understood.

Figure 6 represents a sample set and typical micrograph of material produced in the higher temperature region. The observed trend here (Figure 7a) is one of rapid increase in reacted thickness as a function of time. The transformation front appears uniform in contrast to materials produced in the lower two processing regimes. Scanning electron microscopy (SEM) (Figure 6b) coupled with X-ray diffraction (Figure 7), indicates that the reaction product is a co-continuous structure composed of α-Al_2O_3 and Al.

(a) (b)
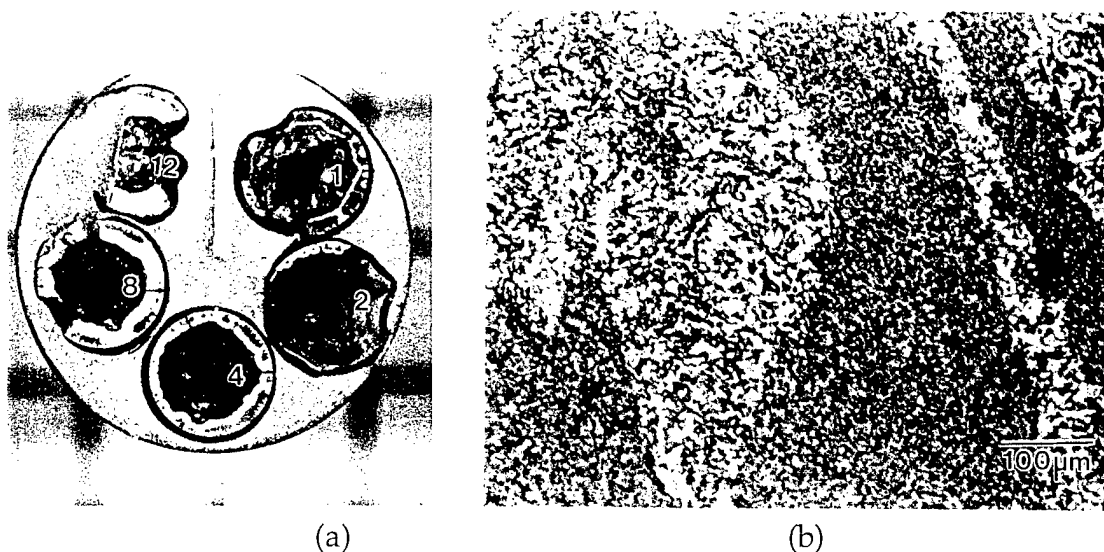
Figure 5. Typical sample set (a) composed of five 10mm specimens produced in the intermediate temperature regime. Numbers represent reaction time. (b) is the corresponding optical micrograph.
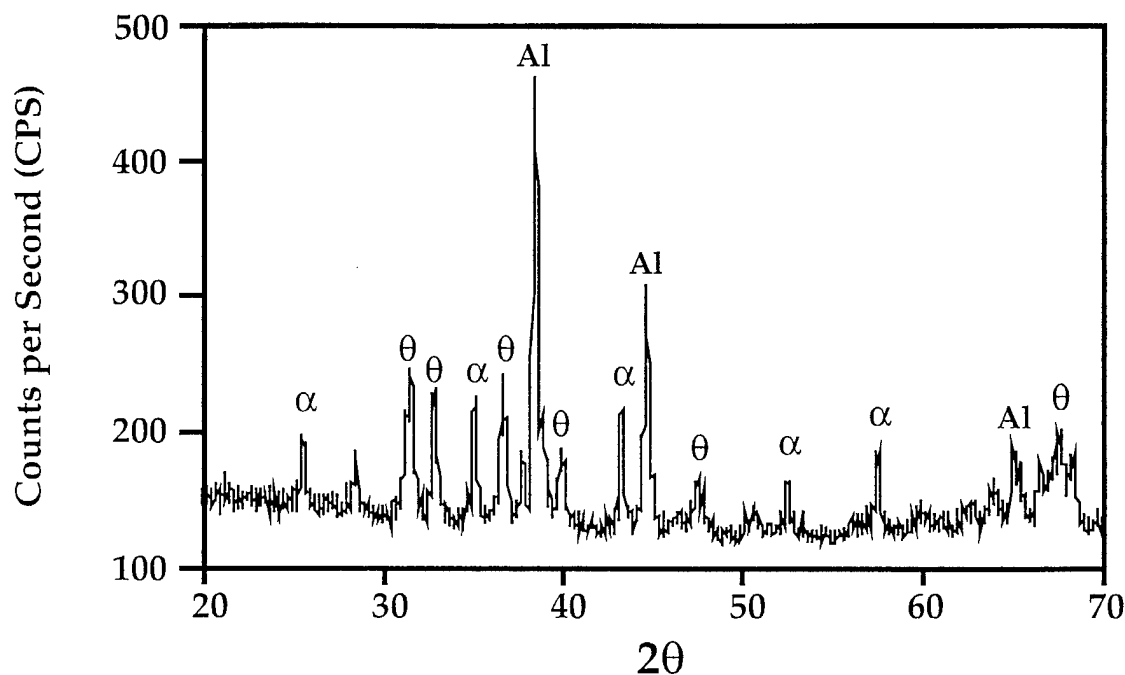
Figure 6. Typical X-ray diffraction data for intermediate temperature regime reaction product. α-Al_2O_3, θ-Al_2O_3 and Al are present.

(a)   (b)
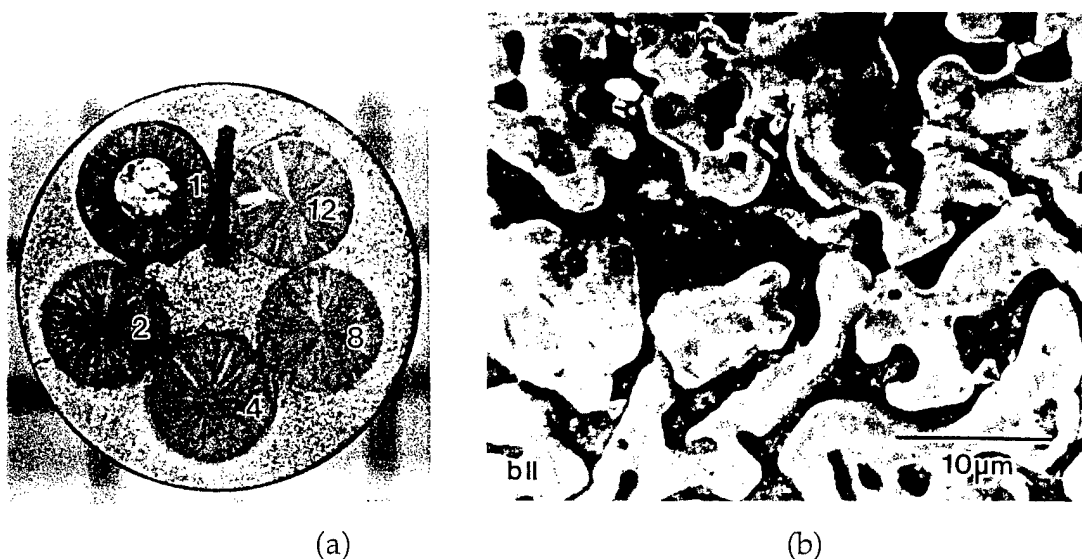
Figure 7.   Typical sample set (a) composed of five 10mm specimens
             produced in the high temperature regime. Numbers represent
             reaction time. (b) is the corresponding scanning electron
             micrograph.
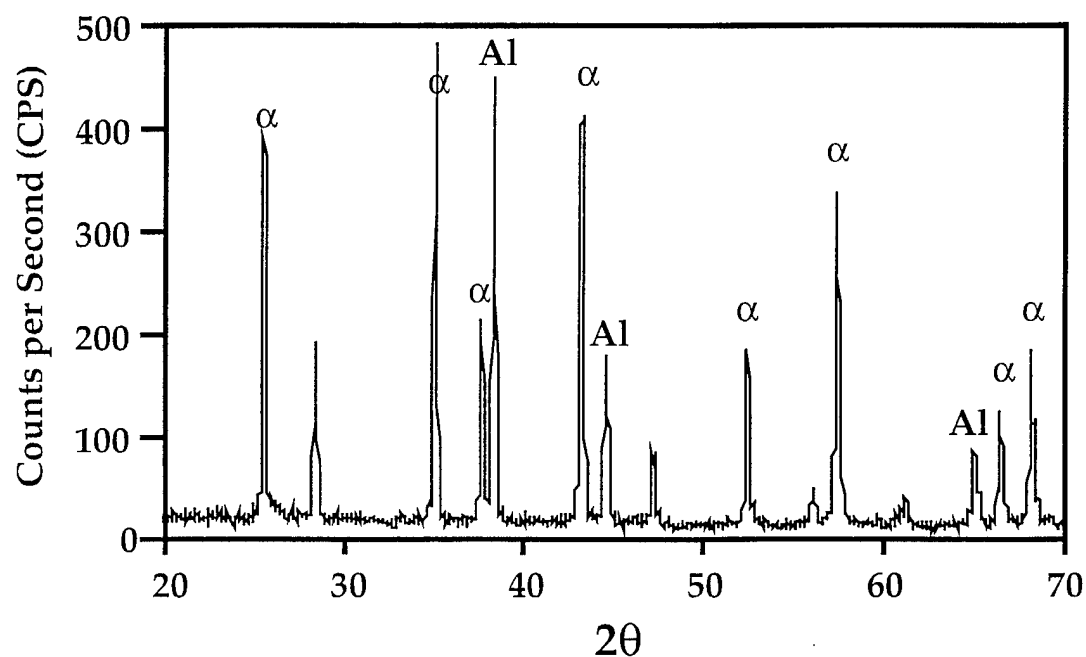
Figure 8.   Typical X-ray diffraction data for high temperature regime
             reaction product. α-Al_2O_3 and Al are present.

The high-temperature processing regime (T ≈ 1000°C and greater) is the region of interest in this study, since it is within this temperature field that the microstructure associated with useful properties is produced [see Appendix B for C^4 properties]. A plot of reacted thickness vs. time for four temperatures in this regime is presented as Figure 9. Significant in this plot is the observed change in behavior of each curve. In all four cases, the reaction rate decreases after a short "induction" period. Experimental evidence [41] indicates that this induction period is a processing artifact due to the temperature difference between the room temperature SiO_2 and the molten Al bath. If the glass is preheated to the temperature of the bath, the induction behavior is not observed, thus this behavior is not considered as part of this study.

The data plotted in Figure 9 is re-plotted as ln(thickness) vs. ln(time) in an attempt to determine the order of reaction (Figure 10). As can be seen in the plot, the slope of the data appears much closer to a value of 1 (zeroth order, linear reaction) than to a value of $1/2$ (first order, parabolic reaction). Thus, for the present arguments, the behavior is considered to be linear.

In Figure 11, the linear portions of the kinetic data presented in Figure 9 are re-plotted, from which the linear reaction constants can be determined. Data from the induction period is ignored since it is not representative of the true material behavior. The slopes of the lines (linear rate constants) are plotted in Arrhenius fashion in Figure 12. The result of this plot indicates an activation energy of approximately 160 kJ/mole for the process.
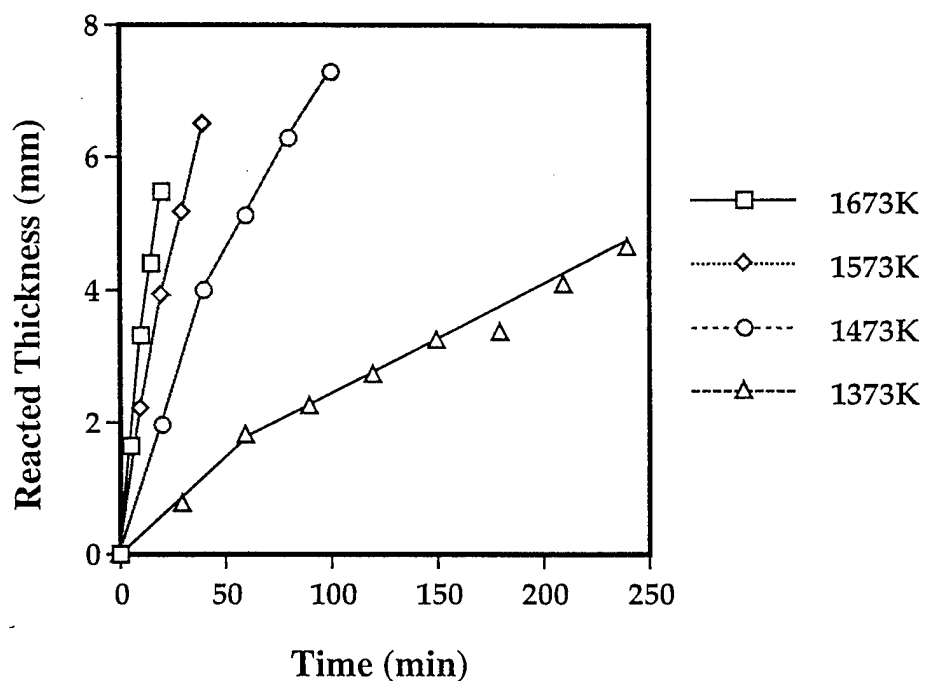
Figure 9.   Plot of thickness vs. time for high temperature processing regime conditions.

Figure 10.   Plot of ln(thickness) vs. ln(time) for high temperature regime data. Note the slope of the plotted data is close to unity.
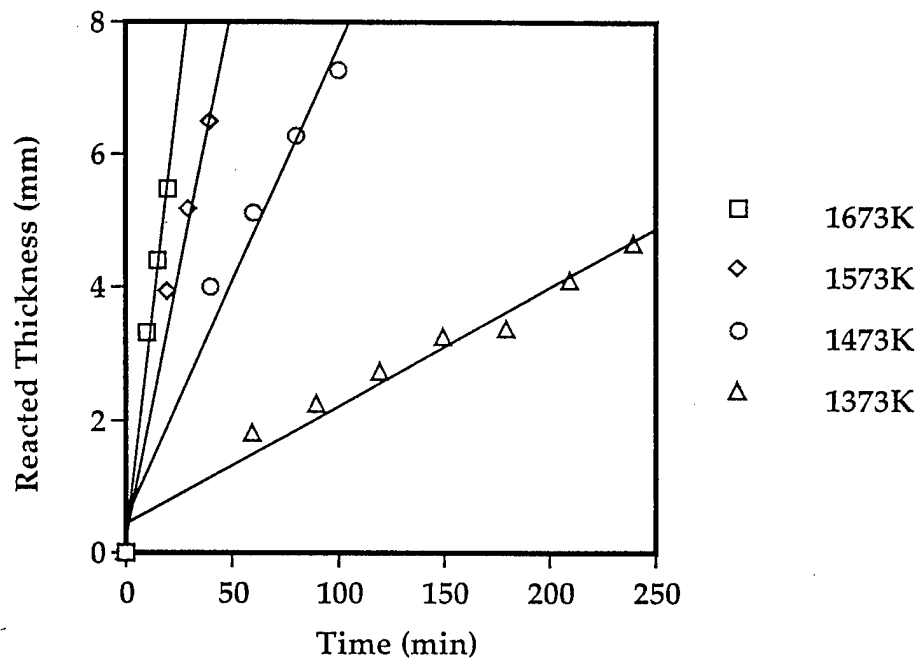
Figure 11. Plot of thickness vs. time for steady state behavior yielding linear rate constants (i.e. slope).
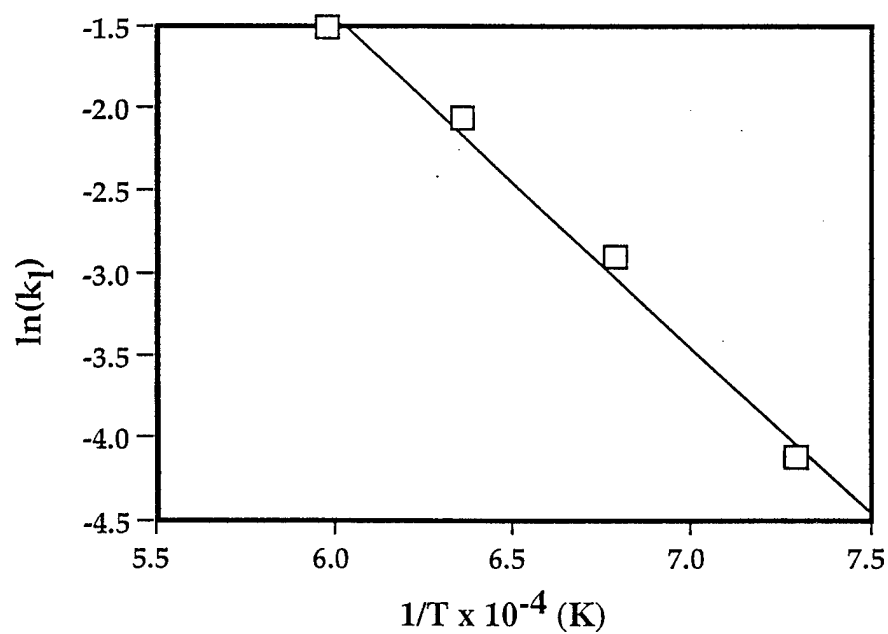
Figure 12. Arrhenius plot of linear activation constants.

CHAPTER V

DISCUSSION

In order to develop a mechanistic model by which SiO_2 is reacted with Al to form C^4, several observations/conditions must be supported. First, the model must account for linear (zeroth order) reaction kinetics as shown in the previous section. Secondly, the proposed model must support the observed co-continuous microstructure. Finally, the model must account for the reported activation energy of 160 kJ/mole. The proposed model, shown graphically in Figure 13, can be shown to support these requirements.
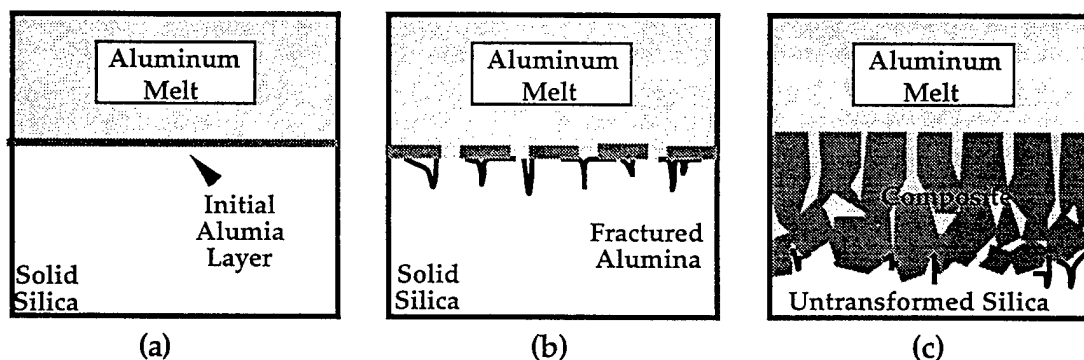
Figure 13.   Proposed schematic model of the C^4 transformation mechanism.

The schematic diagram presented in Figure 13 suggests that the transformation begins shortly after the precursor is placed in contact with the liquid Al. A thin layer of Al_2O_3 forms due to the chemical interaction

proposed in Equation 1 (Figure 13a). Upon transformation there is a volume decrease on the order of 20 to 30 percent associated with 3 moles of Al_2O_3 becoming 2 moles of SiO_2. As a result of this misfit, very high tensile stresses develop in the Al_2O_3 film leading to periodic cracking in the product layer (Figure 13b). Many of these cracks extend into the SiO_2 allowing the molten Al to infiltrate along the cracks and contact the unreacted SiO_2 body. The Al can then react with the SiO_2 along the surfaces formed by the cracks eventually resulting in the observed complex three dimensional co-continuous structure (Figure 13c).

The proposed mechanism can be shown to support the previously mentioned conditions. As Figure 13 suggests, a tensile-cracking mechanism [42] occurs between the metal and ceramic phases. This type of behavior is accompanied by linear reaction kinetics [33]. The model also justifies the observed co-continuous microstructure, thus providing further support to its application. Also, it has been shown that in kinetic behavior of this type, activation energies can not usually be applied to specific processes due to the complex nature of the reaction mechanism, thus the reported value of 160 kJ/mole can be considered an experimental observation.

Further support for this model can be gained by considering the Pilling-Bedworth Ratio (PBR) associated with Equation 1 in the context of the unique nature of this reaction. In most oxidation reactions, the species which is the oxygen receiver (usually metallic) is a solid and the oxygen supply is usually a gas (i.e. fluid). The case at hand differs in that the oxygen receiver is

a fluid (i.e. molten Al) and the oxygen supplier is in the solid phase (i.e. SiO_2). Thus a modification to the common Pilling-Bedworth Ratio must be made.

The standard Pilling-Bedworth Ratio is defined as the specific volume (i.e. molar volume) of oxide to the specific volume of the parent metal on a per mole of metal basis (i.e. Equation 9). This can be re-written in more general terms as:

$$PBR = \frac{\text{Specific Volume of Solid Product}}{K \bullet \text{Specific Volume of Solid Reactant}} \tag{10}$$

where K is the stoichiometric coefficient of the reactant necessary to normalize the equation on a per mole of metal basis. In traditional oxidation studies, Equation 10 and Equation 9 are identical since the solid product is the oxide and the solid reactant is the parent metal. In the case of C^4, however, the solid product is Al_2O_3, and the solid reactant is SiO_2, thus only Equation 10 is applicable.

Since the oxygen supply is solid (i.e. the SiO_2 precursor), the molar quantity of oxygen available for the reaction is fixed, thus the stoichiometry of Equation 1 must be considered. The new Pilling-Bedworth Ratio (defined as PBR') can be expressed as:

$$PBR' = K' \frac{\text{Specific Volume of Alumina}}{\text{Specific Volume of Silica}} \tag{11}$$

where K' is the stoichiometric coefficient necessary to normalize Equation 1 to a per mole basis of reactant. In the present case, a factor of $2/3$, arising from the normalization of Equation 1 to a basis of one mole of SiO_2 is necessary to properly adjust the PBR.

Values for the specific volumes of the relevant phases can be substituted into Equation 11, yielding a value for PBR' of approximately 0.62. This reflects an approximate 38% volume change associated with the transformation of 3 moles of amorphous SiO_2 to 2 moles of α-Al_2O_3. Evidence suggests that a volumetric mismatch of this magnitude should generate sufficient tensile forces at the reaction front [33], thus enabling the reaction to progress as detailed in the model (Figure 13). This finding lends further support to the proposed model.

The above calculation assumes that the amorphous SiO_2 precursor does not undergo devitrification at the reaction interface. Measurements of density of C^4 test pieces shows a wide scatter in values, however, suggesting that the interface can be either amorphous, crystalline, or a combination of both. With this in mind, the PBR' value will range from approximately 68% to 74%. The observed scatter, however, will still support the proceeding hypothesis.

CHAPTER VI

SUMMARY

The following comments can be made in summary of the work presented in this thesis:

- Evidence suggests that the reaction between molten Al and fused SiO_2 exhibits three distinct kinetic regimes resulting in three distinct microstructural reaction products.

- At temperatures below 1100°C, two distinct reaction regions exist. At temperatures below approximately 900°C, a fine grained θ-Al_2O_3/Al product results. Between approximately 900°C and 1100°C the reaction forms a pseudo-duplex structure consisting of α-Al_2O_3/Al islands surrounded by θ-Al_2O_3/Al.

- At temperatures above 1100°C, the reaction can be employed to produce a co-continuous composite material comprised of α-Al_2O_3 and Al (known as C^4) which exhibits attractive mechanical and physical properties.

- The reaction product, C^4 is produced by a near-net shape reaction. The final geometry of the composite body is virtually identical to the fused SiO_2 precursor.

- At temperatures above 1100°C, the reaction which forms the C^4 structure proceeds according to linear rate kinetics.

- At temperatures above 1100°C, the rate of reaction increases as temperature increases.

- The associated activation energy is approximately 160 kJ/mole, and can be considered an apparent activation energy because a rate controlling atomic level process could not be identified.

- A model has been proposed which supports both the linear reaction kinetics and the observed co-continuous microstructure.

- Evidence suggests that the reaction occurs according to a cracking mechanism similar to the oxidation of metals which exhibit a low Pilling-Bedworth Ratio (e.g. Mg).

- A modification has been made to the standard Pilling-Bedworth Ratio (PBR) to account for oxidation systems wherein the phase which supplies oxygen is solid and the phase which receives the oxygen is a fluid. This new term, PBR', incorporates the stoichiometry of the underlying reaction.

REFERENCES

1. Duralcan USA, Product Literature, Alcan Aluminum Corporation, 1993.

2. Du Pont Lanxide Composites, Inc., Product Literature, 1992.

3. D.W. Thompson, *On Growth and Form*, Cambridge at the University Press, 2nd edition, (1968).

4. D.R. Clarke, "Interpenetrating Phase Composites," *J. Am. Ceram. Soc.*, **75**, [4], 739-59, (1992).

5. C. Toy and W.D. Scott, "Ceramic-Metal Composite Produced by Melt Infiltration," *J. Am. Ceram. Soc.*, **73**, [1], 97-101, (1990).

6. M. Ebisawa, T. Hara, T Hayashi, and H. Ushio. "Production Process of Metal Matrix Composite (MMC) Engine Block," *SAE Technical Paper Series*, **910835** (1991).

7. T. Hayashi, H. Ushio, and M. Ebisawa, "The Properties of Hybrid Fiber Reinforced Metal and It's *(sic)* Application for Engine Block," *SAE Technical Paper Series*, **890557**, (1989).

8. W.B. Johnson, B. Sonuparlak, and A. Fortini, "Diamond/Al Metal Matrix Composites Prepared by the Pressureless Metal Infiltration Process," *Proceedings of The 16th Conference on Metal Matrix, Carbon, and Ceramic Matrix Composites*, **2**, 925-32, (1992).

9. B. Sonuparlak, W.B. Johnson, and K.K. Aghajanian, "Processing and Properties of SiC/Al Metal Matrix Composites for Advanced Electronic Applications," *Proceedings of The 16th Conference on Metal Matrix, Carbon, and Ceramic Matrix Composites*, **2**, 1045-53, (1992).

10. M.K. Aghajanian, M.A. Rocazella, T.J. Burke, and S.D. Keck, "The Fabrication of Metal Matrix Composites by a Pressureless Infiltration Technique," *J. Mater. Sci.*, **26**, 447-54, (1991).

11. M. G. Mendiratta, J.J. Lewandowski, and D.M. Dimiduk, "Strength and Ductile-Phase Toughening in the Two-Phase Nb/Nb_5Si_3 Alloys," *Metall. Trans. A,* **22A**, 1573-83, (1991).

12. M.S. Newkirk, A.W. Urquhart, H.R. Zwicker, and E. Breval, "Formation of Lanxide™ Ceramic Composite Materials," *J. Mater. Res.,* **1**, [1], 81-9, (1986).

13. A.S. Nagelberg, "Observations on the Role of Mg and Si in the Directed Oxidation of Al-Mg-Si Alloys," *J. Mater. Res.,* **7**, [2], 265-8, (1992).

14. K.C. Vlach, O. Salas, H. Ni, V Jayaram, C.G. Levi, and, R. Mehrabian, "A Thermogravimetric Study of the Oxidative Growth of Al_2O_3/Al Alloy Composites," *J. Mater. Res.,* **6**, [9], 1982-95, (1991).

15. A.S. Nagleberg, "Growth Kinetics of Al_2O_3/Metal Composites from a Complex Aluminum Alloy," *Solid State Ionics,* **32/33**, 783-8, (1989).

16. A.S. Nagelberg, S. Antolin, and A.W. Urquhart, "Formation of Al_2O_3/Metal Composites by the Directed Oxidation of Molten Aluminum-Magnesium-Silicon Alloys: Part II, Growth Kinetics," *J Am. Ceram. Soc. ,* **75**, [2], 455-62, (1992).

17. R.A. Rapp, A. Ezis, and G.J. Yurek, "Displacement Reactions in the Solid State," *Metall. Trans. ,* **4**, 1283-92, (1973).

18. G.J. Yurek, R.A. Rapp, and J.P. Hirth, "Kinetics of the Displacement Reaction between Iron and Cu_2O," *Metall. Trans. ,* **4**, 1293-1300, (1973).

19. C. Wagner, "The Concept of the Virtual Maximum Rate of a Single Step of a Series Reaction," *Z. Phys. Chem.,* **64**, 49-54, (1969).

20. W.B. Johnson, T.D. Claar, and G.H. Schiroky, "Preparation and Processing of Platelet Reinforced Ceramics by the Directed Reaction of Zirconium with Boron Carbide," *Ceram. Eng. Sci. Proc.,* **9**, [7-8], 588-98, (1989).

21. W.B. Johnson, A.S. Nagelberg, and E. Breval, "Kinetics of Formation of a Platelet-Reinforced Ceramic Composite Prepared by the Directed Reaction of Zirconium with Boron Car bide," *J. Am. Ceram. Soc. ,* **74**, [9], 2093-101, (1991).

22. T.D. Claar, W.B. Johnson, C.A. Anderson, and G.H. Schiroky, "Microstructure and Properties of Platelet Reinforced Ceramics Formed by the Directed Reaction of Zirconium with Boron Carbide," *Ceram. Eng. Sci. Proc.*, **10**, [7-8], 599-609, (1989).

23. K.J. Brondyke, "Effect of Molten Aluminum on Alumina-Silica Refractories," *J. Am. Ceram. Soc.* , **36**, [3], 171-4, (1953).

24. J.G. Lindsay, W.T. Bakker, and W.Dewing, "Chemical Resistance of Refractories to Al and Al-Mg Alloys," *J. Am. Ceram. Soc.*, **47**, [2], 90-4, (1964).

25. R. E. Loehman, K. G. Ewsuk, A. P. Tomsia, J. Ortega and W. Farenholtz, "Near-Net Shape Fabrication of Metal Ceramics by Reactive Metal Infiltration", Presented at the 1993 American Ceramic Society Annual Meeting, Cincinnati, OH.

26. H. George, United States Patent Number **2,702,750**; Patented February 22, 1955.

27. A.E. Standage and M.S. Gani, "Reaction Between Vitreous Silica and Molten Aluminum," *J. Am. Ceram. Soc.*, **50**, [2], 101-5, (1967).

28. W. H. Gitzen, *Alumina as a Ceramic Material*, American Ceramic Society, Inc., 1970, pp. 17.

29. K. Prabriputaloong and M.R. Piggott, "Thin-Film Studies of the Reduction of SiO_2 by Al," *J. Am. Ceram. Soc.*, **56**, [4], 177-80, (1973).

30. K. Prabriputaloong and M.R. Piggott, "Reduction of SiO_2 by Molten Al," *J. Am. Ceram. Soc.*, **56**, [4], 184-5, (1973).

31. W.B. Thacker, *The Kinetics of the Metallothermic Reduction of Amorphous Silica in the Presence of Liquid Aluminum-Silicon Alloys in the Temperature Range 1023K to 1323K*, Master's Thesis, The Ohio State University, 1986.

32. N.B. Pilling and R.E. Bedworth, "The Oxidation of Metals at High Temperatures," *J. Inst. Metals*, **29**, 529-91, (1923).

33. O. Kubaschewski and B.E. Hopkins, *Oxidation of Metals and Alloys*, Butterworth and Co., 1962, pp. 64-70.

34. T.E. Leontis and F.N. Rhines, "Rates of High-Temperature Oxidation of Magnesium and Magnesium Alloys," *Trans. Amer. Inst. Min. Met. Eng.*, **166**, 265-94, (1946).

35. S.J. Gregg and W.B. Jepson, "The High-Temperature Oxidation of Magnesium in Dry and In Moist Oxygen," *J. Inst. Metals*, **87**, 187-203, (1958-59).

36. E.A. Gulbransen and W.S. Wysong, "Thin Oxide Films on Aluminum," *J. Phys. Colloid. Chem.*, **51**, 1087-103, (1947).

37. D. Cubicciotti, "The Reaction Between Uranium and Oxygen," *J. Am. Ceram. Soc.*, **74**, 1079-81, (1952).

38. J.V. Cathcart, J.J. Campbell, and G.P. Smith, "The Microtopography of Oxide Films on Niobium," *J. Electrochem. Soc.*, **105**, [8], 442-6, (1958).

39. O. Kubaschewski and E. Hopkins, "Oxidation of Niobium, Tantalum, Molybdenum and Tungsten," *J. Less-Common Metals*, **2**, 172-80, (1960).

40. R. Prescott and M.J. Graham, "The Oxidation of Iron-Aluminum Alloys," *Oxidation of Metals*, **38**, [1-2], (1992).

41. *Unpublished Work*, J. Seeger, The Ohio State University, 1994.

42. P. Kofstad, *High Temperature Corrosion*, Elsevier Applied Science Publishers Ltd., London, 1988, pp.244-5.

APPENDIX A

UNITED STATES PATENT NUMBER 5,214,011

US005214011A

United States Patent [19]

Breslin

[11] Patent Number: 5,214,011

[45] Date of Patent: May 25, 1993

[54] **PROCESS FOR PREPARING CERAMIC-METAL COMPOSITE BODIES**

[75] Inventor: Michael C. Breslin, Columbus, Ohio

[73] Assignee: BFD, Incorporated, Columbus, Ohio

[21] Appl. No.: 752,824

[22] Filed: Aug. 30, 1991

[51] Int. Cl.^{5} C04B 35/10; C04B 35/46; C04B 35/50; C04B 35/58

[52] U.S. Cl. 501/127; 75/235; 501/126; 501/128; 501/96; 501/105; 501/104; 501/119; 501/125; 501/133; 501/152; 501/153

[58] Field of Search 501/127, 126, 128, 153, 501/96, 105, 104, 119, 125, 133, 152; 75/235

[56] **References Cited**

U.S. PATENT DOCUMENTS

3,437,468	4/1969	Seufert	75/235
3,973,977	8/1976	Wilson	501/120
4,673,435	7/1987	Yamaguchi et al.	75/235
4,847,220	7/1989	Lesher et al.	501/927
4,874,569	10/1989	Kuszyk et al.	501/127
4,885,131	12/1989	Newkirk	501/127
4,886,766	12/1989	Dwivedi	501/128
4,891,345	1/1990	Nadkanni et al.	501/155
4,923,832	5/1990	Newkirk et al.	501/127
4,935,055	6/1990	Aghajanian et al.	501/127
4,940,679	7/1990	Claar et al.	501/127
4,956,319	9/1990	Dwivedi et al.	501/127
4,956,338	9/1990	Rapp et al.	501/127
4,957,779	9/1990	Irick et al.	501/127
4,960,736	10/1990	Luxcz et al.	501/127

OTHER PUBLICATIONS

Nagelberg, Solid State Ionics, 32/33 pp. 783–788 (1989).
Aghajanian et al., J. Am. Ceram. Soc. 73(9) pp. 2610–2614 (1990).

Creber et al., (preprint) Annual Conference on Composites and Adv. Ceram. Mat. Jan. 1988.

Newkirk et al., (preprint) Annual Conference on Composites and Adv. Ceram. Mat. Jan. 1987.

Prabriputaloong et al., J. Am. Ceram. Soc. Apr. (1973) pp. 184–185.

Urquhart, Advanced Materials and Processes Jul. 1991 pp. 25–29.

Schiroky et al., Am. Soc. of Mech. Eng. vol. GT316, Jun. 4–8, 1989 pp. 1–5.

Newkirk, et al., J. Mater. Res. 1(1) Jan./Feb. (1986) pp. 81–89.

Brondyke, J. Am. Ceram. Soc., 36(5) pp. 171–174 (1953).

Standage, J. Am. Ceram. Soc. vol. 50 No. 2 pp. 101–105 (1967).

Primary Examiner—Mark L. Bell
Assistant Examiner—C. M. Bonner
Attorney, Agent, or Firm—Dennis H. Rainear

[57] **ABSTRACT**

A process is presented for the fabrication of a metal/ceramic composite by a non-vapor phase oxidation of a molten metal by contacting said molten metal at an elevated temperature with a sacrificial ceramic preform. The shape of the preform is retained but the ceramic preform is reduced, oxidizing the molten metal. A preferred sacrificial ceramic preform is silica, but can also be, for example, mullite, titania or zirconia, and the preferred molten metal is aluminum or an aluminum alloy. Thus, for example, is produced from immersing a silica preform into molten aluminum alloy, an Al/Al$_2$O$_3$ composite metal/ceramic article which does not contain silica or silicon and which is extremely tough.

16 Claims, No Drawings

1

PROCESS FOR PREPARING CERAMIC-METAL COMPOSITE BODIES

TECHNICAL FIELD

The invention is directed to a non-vapor phase process for forming a ceramic-metal composite article by the reaction of a metal or metal alloy and a sacrificial ceramic preform. The molten metal or alloy is oxidized directly by the ceramic preform, wherein the preform serves as the oxidizer and also as the pattern or geometric form of the final composite article, as the cation of the sacrificial ceramic preform is replaced by a metal ion and the preform shape is retained in the form of a metal-ceramic composite.

BACKGROUND ART

Processes which convert molten aluminum to alumina/aluminum composite through vapor-phase oxidation have been developed by several individuals and companies, including for example, the Lanxide Corporation. The Lanxide DIMOX (directed metal oxidation) processes for preparing ceramic-metal composites requires vapor-phase transport for producing composite product. The Lanxide process (Newkirk, et al., J. Mater. Res. 1(1), January/February 1986, page 81–89) involves oxidation of a bulk molten metal, usually in an inert graphite or alumina crucible, by a gas to produce a solid ceramic-containing body via a directed growth process. The reaction product forms initially on the exposed surface of a pool of the molten metal and then grows outward, fed by transport of additional metal through channels in the ceramic product of the oxidation reaction between the parent metal and the gas phase oxidant. Direct oxidation reaction between silica-containing preform and molten aluminum alloy is not taught.

Brondyke has observed the chemical interaction between molten aluminum and silica. (Brondyke, J. Am. Cerm. Soc., 36 [5] 171–74 (1953)).

Standage et al., in J. Am. Cerm. Soc., vol. 50, no. 2, page 101–105, 1967, teach the reaction between vitreous silica and molten aluminum.

Prabriputaloong et al., J. Am. Ceram. Soc., April 1973, page 184–85, discusses the reduction of SiO_2 by molten aluminum.

It is known that infiltration of ceramic materials (e.g. Al_2O_3) with molten metal can result in metal/ceramic composites.

Prior art processes for the fabrication of alumina/aluminum matrix composites suffer from the limitation in three dimensional growth which tends to restrict the shape of the resulting composite articles. In addition, prior art processes require gas phase reaction. Finally, metal-ceramic articles produced by the conventional methods exhibit undesirable porosity, anisotropy and poor toughness for many applications.

There exists a need for a non-vapor phase process for the production of metal-ceramic articles with increased densification, improved ability to tailor the microhardness and toughness, and which process will produce articles of a predetermined arbitrary shape.

BRIEF DISCLOSURE OF INVENTION

The present invention relates to a process for preparing a metal/ceramic composite material. By the present invention, any sacrificial ceramic preform which is less thermodynamically stable than is the oxide, nitride,

2

carbide, or sulfide of the chosen molten metal or molten metal alloy can be used to oxidize the molten metal or molten alloy to thereby produce a metal/ceramic, or metal/metal oxide composite. The invention includes, for example, a process for forming a metal/ceramic composite, said process comprising the non-vapor phase oxidation of a molten metal or alloy by contacting the molten metal or alloy, at an elevated temperature, to a sacrificial ceramic preform body, whereby the sacrificial ceramic preform body is at least partially reduced, oxidizing the metal to form a metal oxide, metal nitride, metal carbide, or metal sulfide ceramic component, and whereby the sacrificial ceramic preform body experiences reactive progression by the molten metal, and whereby a metal/ceramic composite is produced.

More specifically, it has been surprisingly discovered that one embodiment of the inventive process produces a composite comprising aluminum and alumina without requiring the conventional steps of vapor phase oxidation, powder pressing or physical phase distribution.

In one embodiment, the process of the present invention involves the reaction of a silica (SiO_2) or silica-containing sacrificial preform, which can be either polycrystalline or amorphous, with a molten aluminum alloy or molten aluminum. The silica-containing preform serves as the oxidizer, such as a source of oxygen, in the oxidation of the molten aluminum metal to the ceramic aluminum oxide, with concomitant reduction of silica to silicon dissolved in the molten aluminum. This non-vapor phase process and the composite materials produced thereby are significant advancements over the art. Metal/ceramic composite bodies of near net shape geometry are produced, wherein the geometry of the final body is dictated by the initial geometry of the sacrificial ceramic preform. In addition, the articles produced by the method of the present invention are extremely tough, and have good fracture and impact resistance.

DETAILED DESCRIPTION OF INVENTION

In the process of the present invention, a sacrificial ceramic body or preform, such as silica, mullite, titania, titanium carbide, magnesia, zirconia, zirconium carbide, zirconium nitride, silicon carbide, or silicon nitride, or a combination thereof, is placed in contact with a molten metal such as aluminum, iron, nickel, cobalt, an aluminum alloy, magnesium, titanium, tungsten, tantalum, yttrium, or niobium at a temperature greater than the melting point of the metal, but less than the melting point or softening point of the sacrificial ceramic preform. The preform and the molten metal are maintained in contact at the elevated temperature for a time sufficient to allow the preform to at least partially transform, and preferrably fully transform, into a ceramic metal oxide body containing a metallic phase. The resulting ceramic-metal composite article contains two phases, the first a ceramic based on the metal or metal alloy, and the second a metal, one or both of which phases may be continuous. The ceramic produced may be an oxide, nitride, carbide or sulfide depending on the nature of the starting preform body. By "metal" herein is meant pure metal or metals, metal alloys, intermetallic compounds, and mixtures thereof.

The sacrificial ceramic preform can contain whiskers, particulates, or fibers of one or more of the materials selected from the group consisting of silica, titania, zirconia, alumina, silicon nitride, and silicon carbide.

3

Thus, for example, a silica glass preform containing SiC, alumina, or silicon nitride fibers, particulates, or whiskers can be used in the present invention. The fibers or whiskers may or may not be totally replaced by the metal/metal oxide depending on the reaction temperature and the nature of the fibers, particulates, or whiskers. Alternatively, the fibers, particulates, or whiskers can be retained in the resulting ceramic-metal composite article by utilizing a lower reaction temperature.

In describing herein the "non-vapor phase oxidation of a molten metal by the sacrificial ceramic preform", oxidation is not to be unduly construed as being limited to the transference of one or more oxygen atoms, but shall also include the electron donor/acceptor reaction and electron sharing reactions between the sacrificial ceramic preform and the molten metal or metal alloy.

By "sacrificial ceramic preform" herein is meant the chemical sacrifice (i.e., chemical reduction) while retaining the macroscopic physical or geometric form, i.e., the chemical elements of the preform are sacrificed as the preform is reduced to thereby oxidize the molten metal to a metal oxide. The reduced preform components diffuse outwardly as a solute from the preform shape. The sacrificial ceramic preform can include, for example, an article or material comprising silica, mullite, titania (TiO_2), titanium carbide (TiC), zirconia (ZrO_2), zirconium carbide (ZrC), zirconium nitride (ZrN), silicon nitride (Si_3N_4), silicon carbide (SiC), magnesium oxide (MgO), titanium carbide (TiC), analogous sulfides, or mixtures thereof. Thus oxides, nitrides, sulfides, and carbides are all operative in the present invention.

Metals operative herein as the molten metal can include aluminum, iron, nickel, cobalt, magnesium, titanium, tantalum, tungsten, yttrium, niobium, mixtures thereof and alloys comprising one or more of the aforementioned metals.

It is not critical to the present invention that the sacrificial ceramic preform be an oxide, such as silica, since it can also be any material able to react with the molten metal to form a ceramic. Thus the ceramic formed can be an oxide, nitride, carbide, or sulfide of the molten metal. It is also not critical that the sacrificial ceramic preform be fully replaced by the metal and ceramic, since for some applications it may be desirable to retain an amount of porosity or silica or other ceramic such as silicon carbide or silicon nitride in the final composite. The amount of remaining ceramic from the preform can be controlled according to the present invention by controlling the reaction time and temperature. A reduction in the reaction time can produce articles with residual sacrificial ceramic preform in addition to the metal and metal oxide phases. However, metal-ceramic composites prepared by the present invention exhibit increased hardness, often decreased porosity, and improved toughness as the sacrificial ceramic preform is replaced with metal and metal oxide.

A volume reduction in the resulting ceramic component relative to the volume of the starting preform is achieved in the present invention. As the silica sacrificial ceramic preform is replaced by metal oxide, such as alumina, there is a significant volume contraction of the ceramic of approximately 25 volume per cent. The volume reduction is due to the Al_2O_3 or other metal oxide or ceramic products having smaller volume per mole of oxygen than SiO_2, or TiO_2, or ZrO_2 of the sacrificial ceramic preform. Therefore, the transformation product must have a smaller volume per mole of

4

oxygen than the sacrificial ceramic preform compound. For the replacement of titania in a sacrificial preform by aluminum, the volume change is about 9%. When the ceramic oxide such as SiO_2, is brought into contact with the molten metal, such as aluminum, the reaction starts immediately and the outer ceramic oxide layer is transformed into metal oxide, rejecting silicon, or titanium, or zirconium into the metal melt. It is known that there is a very high solubility for silicon in molten aluminum. Because there is a large decrease in solid volume upon transformation, large tensile stresses develop in the layer of metal oxide formed. Eventually the layer cracks, likely producing cracks in the ceramic oxide preform to which it is bonded. This permits the molten metal to reach deeper into the preform structure. Also, this cracking roughens the melt/ceramic oxide interface. This produces some channels in the reactive progression surface which allows molten Al or other molten metal to flow further inwardly. It is believed that the rough cracked surface requires that the metal oxide growth direction varies locally. This destroys any strong crystallographic texture in the resulting ceramic article. The reaction is maintained and sustained by the continuous flow of molten metal through channels created by cracking of the transformation product. This complicated three dimensional contraction and cracking leads to interconnected blocks of metal oxide with interconnected metal present. Reduced preform material such as elemental Si, Ti, or Zr travels or diffuses from the area of higher concentration within the preform out to the area of lower concentration in the molten metal. It is believed, but the inventor does not wish to be limited to the theory, that as the sacrificial ceramic preform is reduced, the molten metal is oxidized to metal oxide and the molten metal flows through channels in the reaction product permitting the reaction to continue. This leaves reduced metal, such as silicon, titanium, or zirconium in solution which diffuses out into the bulk molten metal surrounding the preform. Analysis of ceramic-metal composites prepared by the present invention indicated, for example, the dramatic reduction of the silicon content in composites prepared from a silica-containing preform.

By this process, metal/ceramic composites have been successfully grown at temperatures between about 1000 and about 1250 degrees Centigrade and growth rates of 8 cm/day have been observed. It has been discovered that the growth rate is related to the process temperature and an increase in temperature will produce an increase in growth rate. The dimensions of the transformed composite are the same as the initial preform to within experimental resolution (i.e., <1% change). The molar volume reduction is replaced or accounted for by the infusion of the molten metal so that the initial shape and size of the preform is maintained.

Conventionally, one would not normally heat the Al metal alloy to more than 300 degrees over its melting point and it is surprising that this results in the reactive progression according to the present invention as a solid state transformation.

In the present invention, the reaction utilized is represented by the following:

$$A_wB_x + M \rightarrow B_yM_z + A$$

where A_wB_x is the sacrificial ceramic preform, and M can be Al, Fe, Ni, Co, Mg, Ti, Ta, W, Y, or Nb. B can be oxygen, nitrogen, sulfur, or carbon. The subscripts

5,214,011

w, x, y, and z need not be equal and can be independently selected depending on the molecular stoichiometry of the ceramic preform composition. A_wB_x can be selected from a wide range of compounds including: silicon dioxide, titanium dioxide, magnesium oxide, silicon nitride, silicon carbide, titanium carbide, zirconium dioxide, zirconium carbide, zirconium nitride, and mixture thereof such as mullite. Carbides, oxides, sulfides, and nitrides of reactive metals are all expected to be operative in the present invention. It is recognized that the resulting reduced metal, A, can react with the molten metal, M, to form another compound.

Thus, the present invention relates to a process for forming a metal/ceramic composite comprising the non-vapor phase oxidation of a molten metal by exposure of the molten metal at an elevated temperature to a sacrificial ceramic preform body, whereby the sacrificial ceramic preform body acts as an oxidizer of the metal and also as a pattern for the shape of the metal/ceramic composite.

Thus, self supporting ceramic composite bodies are produced by reactive progression of a parent metal as a solid state transformation into a sacrificial ceramic preform. The reactive progression typically results in a composite comprising an oxidation product (ceramic or metal oxide), and a residual metal.

The invention relates to a non-vapor phase method for producing composite ceramic articles by reactive progression of metal into a sacrificial ceramic preform, said preform preferably but not necessarily comprising silica. Unlike the prior art, dross materials and fillers are not required in the process of the present invention.

In a preferred embodiment of the present invention, the sacrificial ceramic preform can be silica, quartz, sand, wollastonite, mullite, silicate glass, fluorosilicate glass, fluoroborosilicate glass, aluminosilicate glass, calcium silicate glass, calcium aluminum silicate glass, and calcium aluminum fluorosilicate glass, and the like and mixtures thereof. Any silica source is operative herein if Al is able to displace Si and thereby form Al_2O_3. Higher melting or softening point silicates are preferred, thus quartz or polycrystalline silica and mullite are the most preferred silicas. Lower softening point silicas are less likely to maintain the desired shape.

The sacrificial ceramic preform can also be an oxide, carbide, or nitride or mixture thereof.

The silica-containing preform can be readily prepared in the shape and size of the desired ultimate ceramic article and thereby serve as a geometric form or pattern for the final article.

It is also preferred herein that the metal or metal alloy be molten to serve as a bath to receive the ceramic oxide-containing preform. The preferred metals are aluminum and titanium. The alloy can have a content comprising titanium, aluminum, sources of aluminum, and other metals such as zirconium, hafnium, silicon, magnetized or non-magnetized iron, nickel, cobalt, and magnesium. In one example, the content of the alloy is aluminum, silicon (7.0 weight %) and magnesium (0.3 weight %). Another alloy useful in the present invention is aluminum alloy Alcoa 356, available from Alcoa of Pittsburgh, Pa.

The sacrificial ceramic preform and the molten metal are preferrably contacted such that there is direct and maximum surface contact between the preform and the molten metal. Because the oxidation reaction can be conducted within the preform or crucible and completely under the surface level of the molten metal, it is

clear that a gas phase oxidant or an oxidizing atmosphere is not required in the present invention. This is quite different from the prior art and the Lanxide DIMOX process.

In one embodiment of the process of the present invention, a SiO_2-containing preform decomposes or at least partially decomposes at the elevated temperature of the molten alloy to the extent necessary for the preform to serve as an oxidizer for the oxidation of the liquid metal in the molten aluminum bath to aluminum oxide. The other reaction product is silicon in solution. The silica-containing preform also serves the purpose of dictating the geometry of the final composite body as the aluminum from the molten alloy and aluminum oxide penetrate and replace the silica-containing preform, displacing the silicon atoms. The reaction product typically contains both interconnected alumina and interconnected aluminum. In this manner was prepared a ceramic composite coil-shaped article by immersing a quartz coil or helix in a molten aluminum alloy. The resulting coil-shaped ceramic article had approximately 70 volume per cent alumina and about 30 volume per cent aluminum metal, wherein the alumina was a continuous phase and the Al metal was also continuous. It is believed that at higher process temperatures the percentage of aluminum metal present in the resultant article is less than in comparable articles produced at lower process temperatures. Increased continuity of the alumina phase and reduced continuity of the aluminum phase is achievable at higher process temperatures.

In another embodiment of the present invention, a molten aluminum alloy is poured into a sacrificial ceramic crucible or receptacle which serves as a preform rather than immersing the preform in a molten alloy bath. As discussed above, the ceramic oxide (e.g. SiO_2) of the preform serves to both donate oxygen sufficient to oxidize or at least partially oxidize an amount of the aluminum metal in the molten alloy to aluminum oxide, and also as a mold, model, or pattern for the resulting article. The molten alloy then conforms to the shape of the ceramic oxide crucible or receptacle, penetrates the crucible or receptacle, and the aluminum replaces the non-oxygen atoms in the preform with aluminum atoms and aluminum oxide molecules, to produce the final ceramic-metal composite article. The final article no longer contains the original ceramic oxide (such as silica) but is an aluminum/alumina composite.

In yet another embodiment of the present invention, a silica-containing preform crucible or receptacle is both filled with and immersed in the molten aluminum alloy to thereby increase the rate of migration of aluminum metal into the preform and facilitate the reduction of silica to silicon which is readily dissolved in the surrounding molten aluminum.

According to the present invention, it is believed that the amount of metal in the final product can be increased if the preform porosity is increased.

The articles produced by the process of the present invention can have a continuous phase of aluminum oxide and a discontinuous phase of aluminum metal.

The articles produced by the process of the present invention can also have a continuous phase of aluminum metal from the reduction of the silica followed by replacement of the silica with alumina, wherein the aluminum phase is discontinuous.

By the present invention, it is also possible to have both the metal and the aluminum oxide exist in continu-

5,214,011

7

ous phases which are each infinite or extended matrices or clusters extending throughout the resulting article.

The composite product of the present invention was tested for continuity of the metal phase by means of conductivity measurement. In near cube-shaped (and others) samples, an electric current was found to flow across neighboring and opposite faces, confirming continuity of the metal phase. To test the continuity of the ceramic phase, the samples were placed in concentrated hydrochloric acid to dissolve out the metal phase. In all cases, the metal was removed and the structure retained its original cubic shape, albeit with high porosity. This confirmed the continuity of the ceramic phase, since a lack of continuity of the ceramic phase would cause the acid-etched samples to collapse.

A separate test for continuity of the ceramic phase of the articles produced by the present invention is to heat the article to a temperature well above the melting point of the metal. Thus, for example, when the molten metal used was pure Al, which has a melting point of approximately 660 degrees Centigrade, the composite article would be heated to about 1000 degrees Centigrade. The ability of the articles produced by the present invention to retain the geometry as well as the physical strength at this high temperature illustrates continuous metal oxide phase has been formed to a significant extent.

The articles produced by the process of the present invention comprise a ceramic/metal composite. The inventive composites have relatively high hardness (Rockwell A), electrical conductivity which may be tailored, and are quite resistant to fracture. The specific property values can be varied as desired by modification of the processing parameters, including but not limited to, temperature, aluminum alloy melt composition, porosity of the preform, composition of the preform, phase distribution in the preform, and reaction time.

In one example of the present invention, Si and Mg were added at one weight per cent levels to an aluminum alloy (Alcoa 356) which already contained 7.0% Si and 0.3% Mg. The addition was done during an induction melt prior to the process reaction. The modified Alcoa 356 alloy was then solidified, cooled and cut into smaller pieces. These Al sections were put into silica crucibles, type F-29 obtained from Ferro Corporation, of Crooksville, Ohio and heated in air to a temperature between 1200 and 1500 K. The temperature was maintained for a period of time which was varied from about several hours up to two days. The furnace was then turned off and the contents allowed to slowly cool in air. The resulting crucibles were no longer silica, but were an aluminum/alumina ceramic composite. Samples were also prepared without an induction melt and with essentially pure aluminum without the addition of extra Si or Mg. The composite articles thus produced also exhibited excellent strengths and continuity of phases.

In another example of the present invention, a geometry-specific quartz preform was submerged into the molten Alcoa 356 aluminum alloy yielding a composite body having the same shape as the preform. In this manner quartz rods of 10 millimeters diameter have been fully transformed to aluminum/alumina composites in less than 3 hours at 1473 K.

The metal/ceramic composites of the present invention have a bulk density ranging from approximately 3.3 to 3.5 grams per cubic centimeter based on mass-water displacement method. Rockwell A hardness values of

8

the products of the present invention can range from, but are not limited to, for example, about 60 to about 75.

Modulus of rupture tests (3-point MOR) on the ceramic-metal articles of the present invention yielded values ranging from at least 22 kpsi to greater than 45 kpsi. However, these values are not limitations in the present invention and can be varied by the modifications described herein. The samples for the MOR test were cut by the Orton Foundation, Westerville, Ohio to produce test specimens which did exhibit some undesirable surface cracks. It is believed that the presence of these cracks has substantially reduced the MOR values. It is anticipated that samples produced with fewer and smaller surface cracks will exhibit substantially higher MOR strengths.

X-ray diffraction analysis of the composites of the present invention confirmed that the components were aluminum and alpha-alumina (corundum). Grain diameters in the present invention can be less than 1 micron and up to greater than about 70 microns, but tend to be irregular in shape. The ability of the instant process to produce smaller grain diameters is another advantage of the present invention over the Lanxide DIMOX process, which generally produces grains of sizes greater than 10 microns. This is an important feature of the present invention because, in general, smaller grain sizes produce higher fracture toughness in ceramic materials.

Also, the composite articles of the present invention have low coefficients of thermal expansion, ranging from about 9.6×10^{-6} per degree Centigrade to about 12.25×10^{-6} per degree Centigrade, and good thermal conductivity ranging from about 34 to about 60.25 Watts/(meter)(degrees Centigrade). These features make the articles of the present invention desirable for use in the manufacture of substrates for integrated circuit chips and devices, high temperature combustion engines, and applications needing heat dissipation, wear resistance and low density.

In addition, the bulk density of articles produced by the Lanxide DIMOX process is generally 2.9 to 3.5 grams per cubic centimeter, while the bulk density of articles prepared by the present invention is generally in the range of from 3.3 to 3.5 grams per cubic centimeter.

Another distinctive feature of the present invention relative to the Lanxide DIMOX process is the use herein of a sacrificial geometric preform and also the ability to obtain near-net shape of the final article.

Yet another advantage of the present invention is the high product growth rate of approximately 8 centimeters per day compared to 2.5 to 3.8 centimeters per day in the Lanxide DIMOX process.

Still another advantage of the present invention is the ability to run the reaction in an oxygen free environment such as an argon blanket, or Ar/H mix, or under a full or partial vacuum. Thus the present invention avoids undesirable side oxidation reactions which can occur in the Lanxide DIMOX process and other prior art processes. Because the Lanxide DIMOX process is based on gas-phase oxidation of molten metal, the reaction front remains planar, even on the microscopic scale. Therefore, in the prior art, the Lanxide oxide grows as colonies about 0.5 millimeters in diameter. In addition, the Lanxide DIMOX process grows product with planes perpendicular to the growth direction, that is, the colony growth direction is the c axis of the hexagonal alpha-alumina, and the intercellular region has a very different structure than the regions within the cells. In the present invention, however, the composite

9

product growth is more random and homogeneous. This randomness in growth is important because it produces more isotropic and homogeneous properties in the products than obtainable in the prior art. Thus, the present composite structure viewed along the growth direction is indistinguishable from that viewed along the longitudinal direction.

Furthermore, unlike the products of the Lanxide DIMOX process, the composite articles of the present invention have no strong crystallographic texture.

Finally, the Lanxide DIMOX process relies on the presence of trace elements in the aluminum, a requirement not present in the instant invention.

The materials prepared by the present invention will be useful in high temperature components, electronic packaging materials, ceramic filters, conducting ceramics, and magnetic ceramics. It is also expected that the materials of the present invention will be useful in automotive engine and brake components, metal working dies, wear resistant and mining components, armor, cutting tools, grinding and abrading tools, cutlery and flatware, composite components including metal matrix composites and dual scale composites. Additionally, useful articles can be prepared by the present invention in the form of airframes, prosthetic devices and components, surface coatings and impellar and pump components.

Other advantages and utilities of the present invention will become apparent to those skilled in the art. While certain preferred embodiments of the present invention have been disclosed in detail, it is to be understood that various modifications may be adopted without departing from the spirit of the invention or scope of the following claims.

That which is claimed is:

1. A process for forming an aluminum/ceramic composite comprising the non-vapor phase oxidation of molten aluminum achieved by contacting the molten aluminum to a sacrificial ceramic body, wherein the molten aluminum is at a temperature at least 300 degrees above the melting point of aluminum but below the softening point of the ceramic body, wherein the sacrificial ceramic body is a material selected from the group consisting of silica, quartz, sand, wollastonite, mullite, silicate glass, fluorosilicate glass, fluoroborosilicate glass, aluminosilicate glass, calcium silicate glass, calcium aluminum silicate glass, calcium aluminum fluorosilicate glass, titanium dioxide, titanium carbide, zirconium dioxide, magnesium oxide, silicon nitride, silicon carbide, zirconium carbide, zirconium nitride, metal sulfides, and mixtures thereof, whereby the sacrificial ceramic body at least partially oxidizes the aluminum to form an aluminum oxide ceramic component, and wherein molten aluminum flows into the aluminum oxide ceramic component, and wherein the sacrificial ceramic body is at least partially reduced, whereby an aluminum/ceramic composite is produced possessing a near net shape relative to the shape of the sacrificial ceramic body.

2. The process of claim 1 wherein the molten aluminum metal is an alloy comprising one or more of the metals selected from the group consisting of iron, cobalt, magnesium, titanium, tantalum, tungsten, yttrium, niobium, zirconium, and hafnium.

3. The process of claim 1 wherein the composition of the sacrificial ceramic body is amorphous.

4. The process of claim 1 wherein the composition of the sacrificial ceramic body is crystalline.

5. The process of claim 1 wherein the composite produced comprises aluminum/alumina.

10

6. The process of claim 1 wherein the composite produced has a continuous aluminum phase.

7. The process of claim 1 wherein the composite produced has a continuous ceramic phase.

8. The process of claim 1 wherein the composite produced has a continuous aluminum phase and a continuous ceramic phase.

9. The process of claim 2 wherein the alloy further comprises silicon.

10. The process of claim 1 wherein the sacrificial ceramic body comprises a material which is polycrystalline silica.

11. The process of claim 1 wherein the sacrificial ceramic body comprises a material which is amorphous silica.

12. The process of claim 1 wherein the composite produced is substantially free of the cation of the material of the sacrificial ceramic body.

13. A process for forming a metal/ceramic composite comprising the non-vapor phase oxidation of a molten metal selected from the group consisting of iron, nickel, cobalt, magnesium, titanium, tantalum, tungsten, yttrium, hafnium, niobium and zirconium, achieved by contacting the molten metal to a sacrificial ceramic body, wherein the molten metal is at a temperature significantly above the melting point of the metal but below the softening point of the ceramic body, wherein the sacrificial ceramic body is a material selected from the group consisting of silica, wollastonite, mullite, fluorosilicate glass, fluoroborosilicate glass, aluminosilicate glass, calcium silicate glass, calcium aluminum silicate glass, calcium aluminum fluorosilicate glass, titanium dioxide, titanium carbide, zirconium dioxide, magnesium oxide, silicon nitride, silicon carbide, zirconium carbide, zirconium nitride, metal sulfides, and mixtures thereof, whereby the sacrificial ceramic body at least partially oxidizes the metal to form a metal oxide ceramic component, and wherein molten metal flows into the metal oxide ceramic component, and wherein the sacrificial ceramic body is at least partially reduced, whereby a metal/ceramic composite is produced possessing a near net shape relative to the shape of the sacrificial ceramic body.

14. The process of claim 13 wherein the molten metal is an alloy comprising two or more of the metals selected from the group consisting of aluminum, iron, nickel, cobalt, magnesium, titanium, tantalum, tungsten, yttrium, niobium, zirconium, and hafnium.

15. The process of claim 13 wherein the metal in the metal/composite produced comprises an intermetallic compound.

16. A ceramic composite article produced by a method comprising the non-vapor phase oxidation of a molten metal selected from the group consisting of iron, nickel, cobalt, magnesium, titanium, tantalum, tungsten, yttrium, niobium, zirconium, and hafnium, by contacting the molten metal to a sacrificial ceramic body, wherein the molten metal is at a temperature significantly above the melting point of the metal but below the softening point of the ceramic body, wherein the sacrificial ceramic body is a material selected from the group consisting of silicon dioxide, titanium dioxide, titanium carbide, zirconium dioxide, mullite, magnesium oxide, silicon nitride, silicon carbide, zirconium carbide, zirconium nitride, metal sulfides, and mixtures thereof, whereby the sacrificial ceramic body at least partially oxidizes the metal to form a metal oxide ceramic component, and whereby the metal oxide ceramic component contains the molten metal, and whereby a ceramic composite article is produced possessing a near net shape relative to the shape of the sacrificial ceramic body.

* * * * *

APPENDIX B

PROPERTIES OF C^4 MATERIALS

Table 1.   Typical properties of C^4 material produced from glass precursors reacted with molten Al at 1150°C

Property	Value	Comparison/Comment
Density	3.5-3.7 g/cm^3	steel density 7.8 g/cm^3
Young's Modulus	200-240 GPa	steel modulus 207 GPa
Avg. MOR in 3pt bend	370 MPa	similar to better structural ceramics
Fracture Toughness (K_{IC})	10 MPa m$^{1/2}$	similar to cast irons
Coefficient of Thermal Expansion (α)	10X10^{-6} K^{-1}	slightly below steel
Thermal conductivity	81 W/K• m	twice 1040 steel
Growth rates	1-5 mm/hour	doubles for two side transformation
Phase proportions (approximate)	65%Al$_2$O$_3$, 35%Al	tailorable

APPENDIX C

KINETIC MEASUREMENT DATA

The following tables feature the data on which this thesis is based. All measurements are in metric units (mm, °C, etc.). Data annotated with an "A" designation was collected by Dr. A.L. Marasco using 16mm diameter rods. The data annotated with a "B" was collected by the author using 10mm diameter rods.

Table 2. Kinetic measurement data (1400°C to 1000°C)

Time (min)	1400°C/A	1300°C/A	1200°C/A	1150°C/B	1100°C/A	1100°C/B	1050°C/B	1000°C/A	1000°C/B
					Transformation Thickness (mm)				
0	0	0	0	0	0	0	0	0	0
5	1.635								
10	3.3	2.2							
15	4.369								
20	5.477	3.895	1.957						
25									
30		5.14			0.75			0.4	
35									
40		6.462	3.965						
45									
50									
55									
60			5.114	3	1.777	2	0.7	0.825	1.19
70									
80			6.241						
90					2.229				
100			7.245						
110									
120				5	2.705	4	1.5	1.5	1.93
150					3.208				
180					3.333			3.5	
210					4.048				
240				5	4.62	5	2.78	4.208	2.88
300									
360				5		5	5	6.021	3.95
480				5		5	5		4.48
720									
1080									
1440									

Table 3. Kinetic measurement data (1400°C to 1000°C)

Time (min)	950°C/B	900°C/A	900°C/B	850°C/B	800°C/A	800°C/B	750°C/B	700°C/B
				Transformation Thickness (mm)				
0	0	0	0	0	0	0	0	0
5								
10								
15								
20								
25								
30		0.645			2.111			
35								
40								
45								
50								
55								
60	1.3	0.867	0.4	1.95	2.504	3.28	0.8	
70								
80								
90								
100								
110								
120		1.008		2.4	2.86	3.95	1.7	0.4
150			0.6					
180								
210								
240	1.3	1.178	0.6	2.7	4.363		2.45	1.23
300						5		
360	1.78		1.05	4.45	4.644	5	2.68	2.13
480	2.13	1.455	1.3	4.65	4.821	5	2.6	3.35
720		1.74						
1080		2.088						
1440		2.444						